Ion Transport and Rheological Behavior in Polymeric Systems

Thesis by
Alexandros Tsamopoulos

In Partial Fulfillment of the Requirements for the
Degree of
Doctor of Philosophy in Chemical Engineering

CALIFORNIA INSTITUTE OF TECHNOLOGY
Pasadena, California

2026
Defended March 20, 2026

Alexandros Tsamopoulos
ORCID: 0009-0003-5924-5512

ACKNOWLEDGEMENTS

First and foremost, I would like to express my deepest gratitude to my advisor, Prof. Zhen-Gang Wang, for his mentorship, patience, and guidance throughout my PhD. Zhen-Gang pushed me to grow as a researcher, helped me persevere through the many stages of this journey, and challenged me to think critically and defend my work with confidence.

I am also deeply grateful to my thesis committee, Prof. Julie Kornfield, Prof. John Brady, and Prof. Sujit Datta. I had the privilege of learning from each of them through committee meetings, individual discussions, and their classes. I would also like to thank Prof. Karol Makuch for the fruitful collaboration and discussions we had during the last year of my PhD.

I am grateful to have met, interacted with, and learned from many members of the Wang group. In particular, I would like to mention Sriteja Mantha, Dorian Brunch, Vignesh Bhethanabotla, Chris Balzer, and Yasemin Basdogan. Outside the group, I would also like to thank Mike Vicic and Javier Garcia for brightening many of my days.

I must also mention a few individuals that have strongly influenced my academic journey. First, I would like to thank my undergraduate advisor, Prof. Vlasis Mavrantzas, to whom I am deeply indebted. I also owe a great deal (in many different ways) to Profs. Yannis Dimakopoulos, Konstantinos Asimakopoulos, and Dimitrios Fraggedakis.

Lastly, I want to express my gratitude to my friends in Greece and the US, and especially to those who made the journey from Greece to the US. To Elvira – you made this journey so much different. To my family and my siblings, thank you for everything.

ABSTRACT

Ion-containing polymers are an important class of soft materials, owing to their applications in electrochemical energy storage, fuel cells, and membrane separations, as well as their rich ion transport and mechanical behavior. Their properties are governed by the interplay of polymer connectivity, ion correlations, segmental dynamics, and viscoelastic response across multiple length and time scales. This thesis examines these couplings using molecular simulations of polymer electrolytes, polymerized ionic liquids, and model polymeric fluids. We first investigate ion transport in salt-doped polymer electrolytes and show how temperature and salt concentration jointly control ionic conductivity through their effect on polymer mobility. We then examine polymerized ionic liquids, focusing on how ion correlations and chain length influence polymer relaxation, Onsager transport coefficients, and ion conductivity. Next, we return to the polymer electrolyte system to study the role of salt in controlling their linear and nonlinear rheological response. Finally, we develop a hydrodynamic framework for the diffusion of anisotropic probes in complex fluids, demonstrating that probe motion is governed by the length-scale-dependent viscous response of the surrounding medium. Overall, the range of systems considered here reflects the broader challenge of understanding ion-containing and polymeric materials.

PUBLISHED CONTENT AND CONTRIBUTIONS

[1] Tsamopoulos, A. J.; Wang, Z.-G. *ACS Macro Letters* **(2024)**, 322–327, DOI: 10.1021/acsmacrolett.3c00757.

[2] Stewart, C. J.*; Tsamopoulos, A. J.*; Ye, B. B.; Wang, Z.-G. *The Journal of Chemical Physics* **2025**, *163*, DOI: 10.1063/5.0297386 * Denotes equal contribution.

[3] Tsamopoulos, A. J.; Makuch, K.; Wang, Z.-G. Microrheological Dumbbell Probes in Complex Fluids, *in preparation*, (2026).

[4] Tsamopoulos, A. J.; Wang, Z.-G. Salt effect on the Linear and Nonlinear Viscoelastic Response of Polymer Electrolytes, *in preparation*, 2026.

In each of the above, A.J.T. participated in the conception of the project, conducted calculations, analyzed data, and participated in the writing of the manuscript.

TABLE OF CONTENTS

LIST OF ILLUSTRATIONS

Number *Page*

Chapter 1

INTRODUCTION

This introductory chapter gives an overview of ion-containing polymers, their application in Li-ion batteries, and their limitations. The subsequent chapters will delve into the ion transport behavior and rheology of charged polymeric systems, while the last chapter presents a hydrodynamic framework for anisotropic probe diffusion in complex fluids.

1.1 Lithium-Ion Batteries

Lithium-ion batteries are the current standard for rechargeable energy storage, used in portable electronics, stationary grid-energy storage, and electric vehicles [1, 2]. Their widespread use has been enabled by reductions in costs and improvements in energy density. Over the past 30 years, battery costs have fallen by $\sim 99\%$, while their energy density has increased approximately fivefold [3]. In 2024, electric vehicle sales exceeded 17 million [4]. However, wider deployment at scale still requires further improvements in energy storage technology [5, 6].

Modern batteries typically use flammable organic liquid electrolytes (e.g., mixtures of alkyl carbonates and lithium salts), which raise safety concerns and complicate the use of higher-energy electrode chemistries [7, 8]. For example, lithium–metal anodes offer higher specific capacity than the typical graphite anode but, in liquid electrolytes, can more easily form lithium dendrites, which cause short circuits, and trigger thermal runaway [9]. Therefore, a central scientific objective is developing alternate electrolyte materials that can support high–energy electrodes while reducing the risk of catastrophic failures [10].

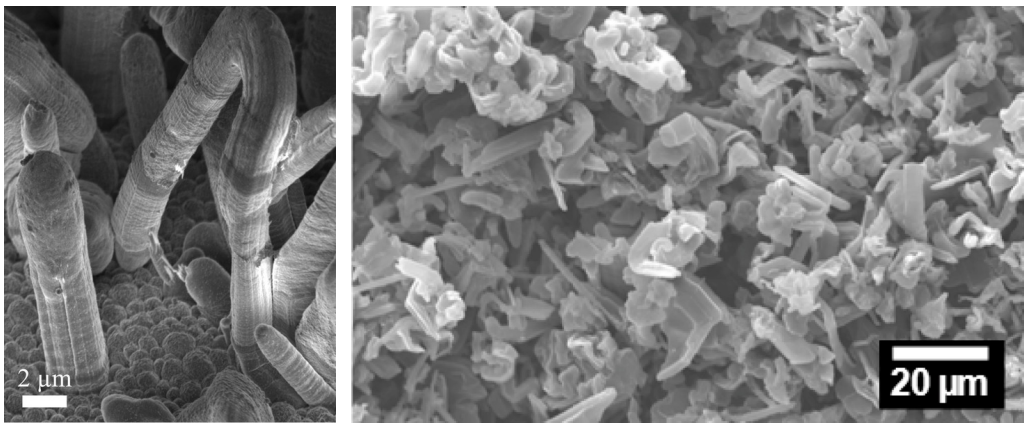

(a) (b)

Figure 1.1: Complex local morphology of Li growth at the micrometer scale. (a) scanning electron microscopy (SEM) image of electrodeposited lithium in carbonate electrolyte, showing kinked and loop-like deposits attached to the substrate. Reproduced from Becherer *et al.* [11]. (b) SEM image of electrodeposited lithium on a Cu substrate from 1 M $LiPF_6$ in propylene carbonate, showing a rough dendritic morphology characteristic of unstable Li growth. Reproduced from Ding *et al.* [12].

1.2 Ion-Containing Polymers

One avenue to reduce the risk of thermal runaway is the replacement of organic liquid electrolytes with polymer electrolytes (PEs). This class of materials was first

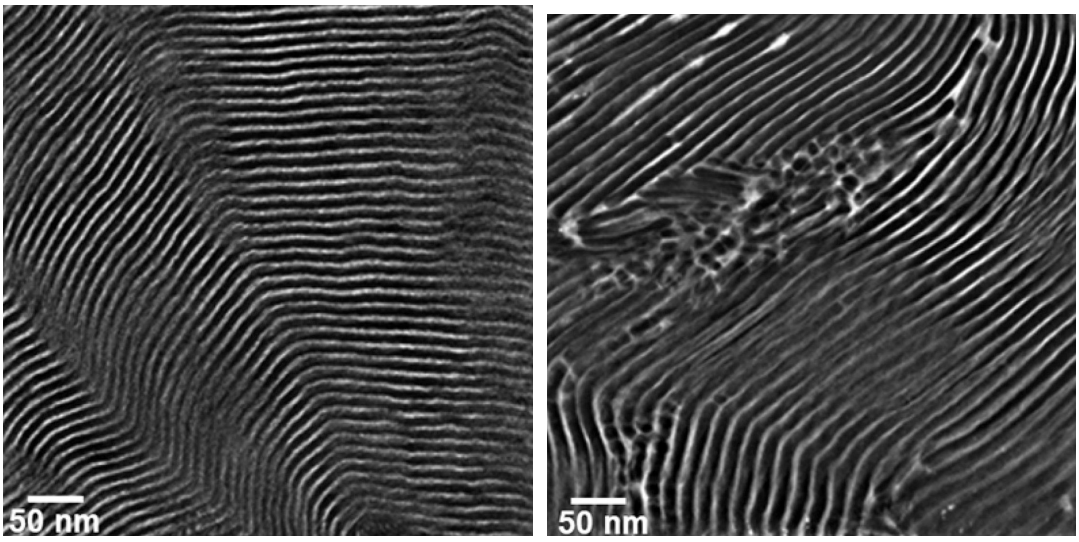

(a) (b)

Figure 1.2: (a) Dark-field transmission electron microscopy image of PEO-PS block-copolymer, showing well-defined lamellar microdomains separated by grain boundaries. (b) Representative image from the same system with added LiTFSI salt, indicating perforated lamellar morphology. The bright regions correspond to PEO-rich domains (ionic nanochannels) and the dark region to the PS-rich domains (mechanically rigid). Reproduced from Chintapalli *et al.* [17].

developed in 1973 by Fenton *et al.* [13], who discovered that alkali salt could be dissolved in poly(ethylene oxide), while Armand *et al.* [14] demonstrated that such mixtures can conduct ions and be used as electrolytes in batteries. In general, PEs consist of a lithium salt in a neutral polymer matrix. They are less volatile than organic electrolytes and can suppress lithium dendrite growth [10, 15]. However, most PEs exhibit low ionic conductivity at room temperature (often $\sigma \sim 10^{-4}$ S cm^{-1} or below), and low cation transference number ($t^+ \sim 0.3$), which have hindered their commercialization [16].

Significant efforts have been made to improve the performance of PEs, which introduced the need to investigate the ion transport in such systems. A common strategy is to combine components that provide both mechanical strength and high ion conductivity. Gel electrolytes, formed by adding plasticizers (such as small-molecule solvents or ionic liquids) to PEs, generally exhibit higher conductivity. However, these small-molecule solvents can reduce mechanical strength, and thus increase the formation of Li dendrite, while also increasing flammability [18, 19]. Another approach is by using polymer blends or block copolymers that can microphase separate, creating mechanically rigid domains and ionic nanochannels. While these

materials are able to further slow down dendrite growth, they are also linked to an increase in the glass transition temperature (T_g) of PEO, resulting to a decrease in conductivity. Lastly, polymerized ionic liquids (PILs) are a distinct class of materials in which either the cationic or anionic component of a conventional ionic liquid is incorporated into the polymer repeat unit. These materials can exhibit ion transference numbers close to unity and favorable mechanical properties owing to their high glass-transition temperatures. However, their ionic conductivity is typically lower than that of PEs by 2-3 orders of magnitude [20].

A longstanding conclusion is that, in amorphous polymer electrolytes, ion transport depends strongly on polymer segmental mobility and thus correlates with the glass transition temperature T_g [21, 22]. This coupling creates a fundamental design tradeoff: increasing conductivity typically motivates softer, more mobile polymer hosts, whereas dendrite suppression requires higher mechanical resistance [7]. These competing constraints motivate a closer examination of the microscopic mechanisms governing ion transport in polymer electrolytes and how they evolve with polymer architecture, temperature, and salt-doping.

1.3 Outline

In this thesis, we employ molecular simulations to gain a mechanistic understanding of ion transport and rheology in polymeric systems. In Chapter 2, we dive into the ion transport behavior of polymer electrolytes, and provide a model to predict how temperature and salt–doping affect the conductivity. In Chapter 3, we construct a coarse–grained model of polymerized ionic liquids, to understand the interplay between electrostatic correlation and ion conductivity. In Chapter 4, we investigate the linear and non-linear viscoelastic response of Polymer Electrolytes. In Chapter 5, we explore the diffusion of anisotropic probes in complex fluids through the lens of wave-vector-dependent viscosity.

References

[1] Goodenough, J. B.; Kim, Y. *Chemistry of Materials* **2010**, *22*, 587–603, DOI: 10.1021/cm901452z.

[2] Goodenough, J. B.; Park, K.-S. *Journal of the American Chemical Society* **2013**, *135*, 1167–1176, DOI: 10.1021/ja3091438.

[3] International Energy Agency Executive summary – Global EV Outlook 2025 – Analysis, https://www.iea.org/reports/global-ev-outlook-2025/executive-summary, 2025.

[4] Solomon, M. The Rise of Batteries in Six Charts and Not Too Many Numbers, https://rmi.org/the-rise-of-batteries-in-six-charts-and-not-too-many-numbers/, 2024.

[5] Tarascon, J.-M.; Armand, M. *Nature* **2001**, *414*, 359–367, DOI: 10.1038/35104644.

[6] Armand, M.; Tarascon, J.-M. *Nature* **2008**, *451*, 652–657, DOI: 10.1038/451652a.

[7] Miller, T. F. I.; Wang, Z.-G.; Coates, G. W.; Balsara, N. P. *Accounts of Chemical Research* **2017**, *50*, 590–593, DOI: 10.1021/acs.accounts.6b00568.

[8] Xu, K. *Chemical Reviews* **2004**, *104*, 4303–4418, DOI: 10.1021/cr030203g.

[9] Peled, E.; Menkin, S. *Journal of The Electrochemical Society* **2017**, *164*, A1703, DOI: 10.1149/2.1441707jes.

[10] Khurana, R.; Schaefer, J. L.; Archer, L. A.; Coates, G. W. *Journal of the American Chemical Society* **2014**, *136*, 7395–7402, DOI: 10.1021/ja502133j.

[11] Becherer, J.; Kramer, D.; Mönig, R. *Journal of Materials Chemistry A* **2022**, *10*, 5530–5539, DOI: 10.1039/D1TA10920K.

[12] Ding, F.; Xu, W.; Graff, G. L.; Zhang, J.; Sushko, M. L.; Chen, X.; Shao, Y.; Engelhard, M. H.; Nie, Z.; Xiao, J.; Liu, X.; Sushko, P. V.; Liu, J.; Zhang, J.-G. *Journal of the American Chemical Society* **2013**, *135*, 4450–4456, DOI: 10.1021/ja312241y.

[13] Fenton, D. E.; Parker, J. M.; Wright, P. V. *Polymer* **1973**, *14*, 589, DOI: 10.1016/0032-3861(73)90146-8.

[14] Armand, M. B. *Annual Review of Materials Research* **1986**, *16*, 245–261, DOI: 10.1146/annurev.ms.16.080186.001333.

[15] Hallinan, D. T.; Balsara, N. P. *Annual Review of Materials Research* **2013**, *43*, 503–525, DOI: 10.1146/annurev-matsci-071312-121705.

[16] Xue, Z.; He, D.; Xie, X. *Journal of Materials Chemistry A* **2015**, *3*, 19218–19253, DOI: 10.1039/C5TA03471J.

[17] Chintapalli, M.; Le, T. N. P.; Venkatesan, N. R.; Mackay, N. G.; Rojas, A. A.; Thelen, J. L.; Chen, X. C.; Devaux, D.; Balsara, N. P. *Macromolecules* **2016**, *49*, 1770–1780, DOI: 10.1021/acs.macromol.5b02620.

[18] Song, J.; Wang, Y.; Wan, C. *Journal of Power Sources* **1999**, *77*, 183–197, DOI: 10.1016/s0378-7753(98)00193-1.

[19] Son, C. Y.; Wang, Z.-G. *The Journal of Chemical Physics* **2020**, *153*, 100903, DOI: 10.1063/5.0016163.

[20] Ganesan, V. *Molecular Systems Design & Engineering* **2019**, *4*, 280–293, DOI: 10.1039/c8me00114f.

[21] Mongcopa, K. I. S.; Gribble, D. A.; Loo, W. S.; Tyagi, M.; Mullin, S. A.; Balsara, N. P. *Macromolecules* **2020**, *53*, 2406–2411, DOI: 10.1021/acs.macromol.0c00091.

[22] Wheatle, B. K.; Lynd, N. A.; Ganesan, V. *ACS Macro Letters* **2018**, *7*, 1149–1154, DOI: 10.1021/acsmacrolett.8b00594.

Chapter 2

ION CONDUCTIVITY IN SALT-DOPED POLYMERS: COMBINED EFFECTS OF TEMPERATURE AND SALT CONCENTRATION

We construct a coarse–grained molecular dynamics model based on poly(ethylene oxide) and lithium bis-(trifluoromethane)sulfonimide salt to examine the combined effects of temperature and salt concentration on the transport properties. Salt doping notably slows down the dynamics of polymer chains and reduces ion diffusivity, resulting in a glass transition temperature increase proportional to the salt concentration. The polymer diffusion is shown to be well represented by a modified Vogel–Fulcher–Tamman (M-VFT) equation that accounts for both the temperature and salt concentration dependence. Furthermore, we find that at any temperature, the concentration dependence of the conductivity is well described by the product of its infinite dilution value and a correction factor accounting for the reduced segmental mobility with increasing salt concentration. These results highlight the important role of polymer segmental mobility in the salt concentration dependence of ion conductivity for temperatures near and above the glass transition.

This chapter includes content from our previously published article:

Tsamopoulos, A. J.; Wang, Z.-G. *ACS Macro Letters* **(2024)**, 322–327, DOI: 10.1021/acsmacrolett.3c00757

2.1 Introduction

Electrolytes in energy storage devices, such as Li-ion batteries, typically consist of organic solvents and binary salts. Existing commercial energy storage devices use organic electrolytes, which come with safety and performance concerns [1], such as thermal runaway and electrolyte decomposition. Solvent-free polymer electrolytes (PEs), e.g., salt-doped poly(ethylene)oxide (PEO), offer promising alternatives with low flammability, good mechanical stability, and suppression of the formation of Li dendrite growth [2]. However, PEs suffer from low ion conductivity ($\sigma \sim 10^{-4}$ S cm^{-1}) and low cation transference number ($t_+ \sim 0.3$) [3]. To overcome these performance bottlenecks, a comprehensive understanding of the ion transport mechanisms in these materials is necessary.

Seminal steps in this direction were taken by Borodin and Smith [4], who conducted molecular dynamics (MD) simulations with polarizable force fields. They proposed three ion transport mechanisms, namely: (1) polymer–ion co-diffusion, (2) ion motion along the polymer chain (intra-chain), and (3) inter-segmental ion hopping. Their study indicated that the dynamics of both cations and anions are coupled to the polymer segmental relaxation. Further studies by Maitra and Heuer [5, 6] provided analytical expressions for the lithium ion diffusivity D_{Li^+} in terms of the polymer chain length based on the three characteristic timescales of the proposed ion transport mechanisms. Additional MD studies by Molinari et al. [7] suggested that polymer segmental relaxation is mainly responsible for the Li^+ diffusion, and that interchain hops are rare; however, this conclusion was based on simulations at much higher temperatures than the glass transition temperature of the system. While these studies focused on the mechanisms that determine Li^+ diffusion, they did not explore the effect of salt concentration on the polymer mobility and on the glass transition temperature, factors that are crucial in determining ion transport.

Balsara and co-workers [8, 9] conducted quasi-elastic neutron scattering experiments to understand how salt concentration influences the ion conductivity of PEO doped with lithium bis(trifluoromethane) sulfonimide salt (PEO/LiTFSI). They found that the conductivity reaches a maximum with respect to salt concentration, as a result of the competing effects of increased charge carriers and the slowdown of polymer segmental dynamics. This result was corroborated by the computer simulation study of Webb et al. [10] for PEO doped with LiPF_6, where addition of the lithium salt was shown to result in a global slowdown of chain dynamics.

An analogous trend to the concentration dependence of the ion conductivity was

reported in terms of the polymer host polarity. Ganesan and coworkers [11, 12] performed molecular dynamics simulations to examine how the polar nature of the polymer chain influences ion transport properties. It was found that by increasing the dielectric permittivity of the polymer medium, the ion conductivity increases due to the weakened ion interactions. At higher dielectric constant, however, the enhanced polymer–polymer dipolar interactions impede the segmental relaxation dynamics, leading to a decrease of the ionic conductivity. They suggested that there is an intermediate dipole strength for which the ion conductivity is optimal.

In this work, we report results from coarse-grained molecular dynamics simulations aimed at exploring the combined effect of salt concentration and temperature on the ion transport in systems such as PEO doped with LiTFSI. We find that the polymer segmental dynamics are primarily responsible for the non-monotonic behavior of conductivity with salt concentration and propose a modified Vogel–Fulcher–Tammann (M-VFT) equation to describe the temperature and salt concentration dependence of the polymer segmental mobility, that remains valid near the glass transition temperature.

We follow the simulation framework developed by Hall and co-workers [13–15] to model lithium-salt doped polymers (such as the PEO/LiTFSI system) in which the polymer dynamics is described by the Kremer–Grest model [16, 17] and the strong ion–polymer interaction is captured by a $1/r^4$ solvation potential. In order to capture glass transition and the effects of temperature on the segmental dynamics, we include an attractive interaction between non-bonded monomer beads [18, 19]. More details on the simulation methods and the mapping from coarse-grained to real units are provided in the Appendix.

2.2 Results and Discussion

As the chain dynamics are intimately related to the proximity to glass transition [18] and lithium-salt doping is known to affect the chain dynamics [8, 10], we first examine the dependence of glass transition temperature, T_g, on salt concentration. A common method for determining T_g is by measuring the temperature dependence of the simulation volume under isobaric conditions [20, 21]. At the glass transition, there is a characteristic change in the slope of the volume when plotted as a function of the temperature (see Appendix). As shown in Figure 2.1, T_g increases with salt concentration and follows a straight line for the concentration range we studied. Both the order of magnitude of the T_g shift and the nearly linear dependence on

salt concentration are consistent with the experimental findings (see Appendix) [22]. Considering the simplicity of the coarse-grained model used in our work, the agreement is reasonable and reassuring. This behavior can be attributed to the increased ion–polymer complexation leading to restricted motion of the polymer backbone [10], and to the decreased partial molar volume of the polymer (see Appendix). Further, it has been reported in previous studies [23] that the ion–polymer interactions lead to dynamic cross–linking of the polymer chains, effectively increasing the apparent molecular weight, and thus increasing T_g [24].

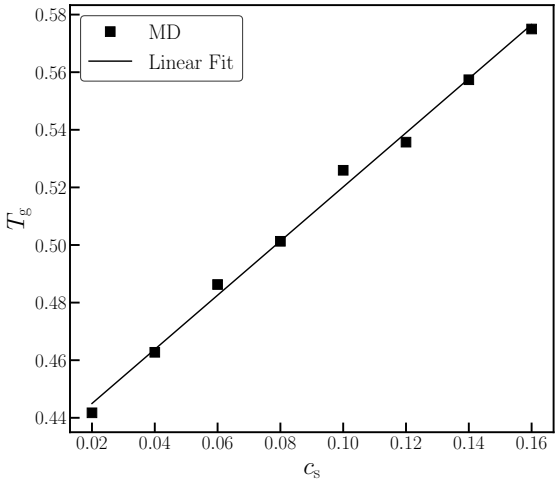

Figure 2.1: Glass transition temperature, T_g, as a function of salt concentration, c_s.

The most direct transport properties of the salt-doped polymer system are the self-diffusivities of the ions and center-of-mass self-diffusivity of the polymer, determined from:

$$D_\alpha = \lim_{t\to\infty} \frac{\langle \Delta \boldsymbol{R}_\alpha(t)^2 \rangle}{6t} \tag{2.1}$$

where $\langle \Delta \boldsymbol{R}_\alpha(t)^2 \rangle$ is the mean–square displacement (MSD) of species α (α = +, −, and p) during time t. For the polymer, $\boldsymbol{R}_p(t)$ refers to the center-of-mass position of the chain. The salt concentration dependence of the diffusion of all species at $T = 1.0$ is shown in the Appendix. The diffusivity of all species decrease as c_s increases due to the strong ion–polymer coupling [4].

Since the sum of the anion and cation diffusivities is proportional to the Nernst–Einstein conductivity, we examine its dependence on the salt concentration. Notably,

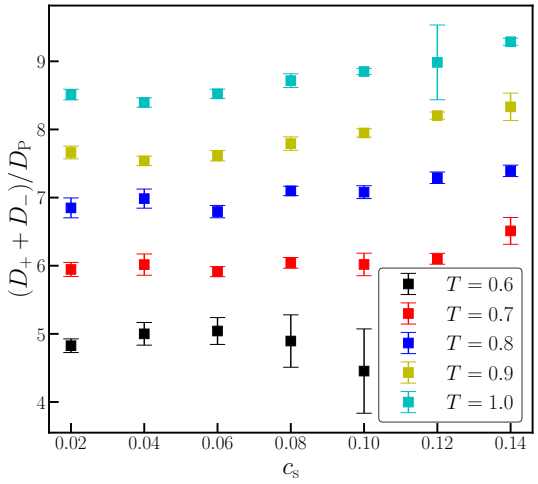

Figure 2.2: Ratio of the total ion diffusion over the polymer diffusion, $(D_+ + D_-)/D_P$, as a function of salt concentration, c_s.

while all the diffusivities decrease with increasing salt concentration, Figure 2.2 shows that the ratio $(D_+ + D_-)/D_p$ is relatively constant for each temperature. This result indicates that the ion diffusivities and polymer diffusivity have different temperature effects but similar salt concentration effects.

For unentangled polymer melts, the polymer diffusivity is inversely proportional to the monomeric friction coefficient ζ. Previous studies have employed the Rouse model to examine the dynamics of polymer chains under lithium salt doping, nanoparticle doping, and concurrent salt and nanoparticle doping [10, 25, 26]. As shown in Appendix, the chain dynamics are well described by the Rouse modes for all the modes well above the glass transition. Near the glass transition, the high-p modes exhibit notable deviation from the expected Rouse dynamics, but the low-p modes still follow the Rouse behavior. We thus take the lowest Rouse mode corresponding to the center-of-mass diffusion to define the friction coefficient via $D_P = kT/N\zeta$. Mongcopa et al. [8] have suggested that the friction coefficient follows an exponential dependence on salt concentration. Our results confirm this to be the case at high temperatures. However, at lower temperatures closer to T_g, there is strong deviation from the exponential dependence; the friction instead becomes super-exponential (see Appendix).

Since the diffusion of a pure polymer melt close to T_g is well described by a Vogel–Fulcher–Tamman (VFT) temperature dependence, we propose a modified VFT (M-VFT) formula by taking into account the observed linear shift in the glass

transition temperature with salt concentration and possible increase in the activation energy [27, 28]:

$$D_{\mathrm{P}} = B \exp\left[-\frac{E^{(0)} + E^{(1)} c_{\mathrm{s}}}{T - (T_0^{(0)} + a^{(1)} c_{\mathrm{s}})}\right] \tag{2.2}$$

where B is a prefactor, $E^{(0)}$ is the activation energy in the pure polymer melt, and $T_0^{(0)}$ is the Vogel temperature of the pure polymer melt [27], typically taken to be 50K below the glass transition temperature T_{g}. $E^{(1)}$ and $a^{(1)}$ are coefficients for capturing the leading-order dependence on salt concentration in the activation energy and glass transition temperature, respectively.

In Figure 2.3, we show D_{P} in an Arrhenius plot for the 8 salt concentrations (including 0 salt) studied in our work. The symbols are the simulation data. D_{P} is seen to decrease with increasing salt concentration and decreasing temperature. The solid lines are the results of fitting. We find that with a single set of fitting parameters, $B = 0.01273$, $E^{(0)} = 1.295$, $E^{(1)} = 4.201$, $T_0^{(0)} = 0.245$, $a^{(1)} = 1.249$, eq. (2.2) is able to describe all the simulation data well.

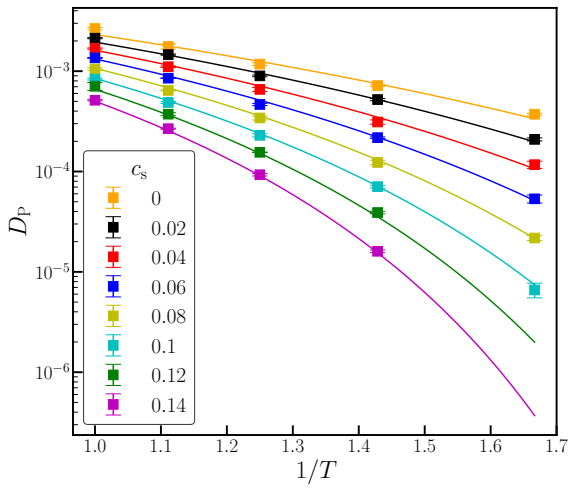

Figure 2.3: Polymer center of mass diffusivity, D_{P}, as a function of 1/T, for various salt concentrations.

The ion conductivity is a complex function of ion–ion correlations and segmental dynamics. Typically in an electrolyte solution, increasing salt concentration increases ion-ion correlations–in the form of ion pairing and ion clustering–and the

friction coefficient or solution viscosity. Both factors contribute to a decrease in the ion mobility [29, 30].

However, for the PEO/LiTFSI system, the experimental work by Mongcopa et al. [8] showed that the reduction of the conductivity is primarily due to the slowing down of the polymer segmental dynamics, implying that ion–ion correlation plays a relatively minor role in governing the conductivity [31]. The physical reason for the weak ion–ion correlation in the LiTFSI–PEO system is likely due to the strong Li–PEO interaction which results in the seclusion of the Li^+ ions from forming ion pairs and clusters with the bulky $TFSI^-$ ions [32]. In our coarse-grained model, the weakness of the ion–ion correlation can be gleaned from the radial distribution function of the polymer beads and anions from the cation (see Appendix). To quantify the effects of the ion–ion correlation on the ion conductivity, we compare its value computed using the exact (Einstein) equation

$$\sigma = \lim_{t\to\infty} \frac{e^2}{6tVk_\mathrm{B}T} \sum_{\mathrm{i,j}}^{n} \left\langle \left(z_\mathrm{i}\Delta\boldsymbol{R}_\mathrm{i}(t)\right) \cdot \left(z_\mathrm{j}\Delta\boldsymbol{R}_\mathrm{j}(t)\right) \right\rangle \tag{2.3}$$

with the approximate expression from using the ion diffusivities (the Nernst–Einstein equation)

$$\sigma^{\mathrm{NE}} = \frac{e^2}{Vk_\mathrm{B}T}(N_+z_+^2D_+ + N_-z_-^2D_-) \tag{2.4}$$

In these expressions, e is the elementary charge, V is the simulation volume, k_B is the Boltzmann constant, T is the temperature, z_i is the ion valency, and $\Delta\boldsymbol{R}_\mathrm{i}(t)$ is the displacement of particle i during time t. N_+ and N_- are respectively the number of cations and anions, and D_+ and D_- are the corresponding diffusivity. We note that while the choice of reference frame can influence the cation transference number [33, 34], the ion conductivity, which is the focus of this work, is independent of this choice [35, 36].

In Figure 2.4, we show the ion conductivity computed using eq. (2.3) together with the Nernst–Einstein conductivity calculated using eq. (2.4) as a function of salt concentration at the high temperature $T = 1.0$. With increasing salt concentration, the conductivity initially increases, reaches a maximum, and then decreases; this non-monotonic behavior is consistent with both earlier simulations and experiments [4, 8]. Within the error bars of the simulation data, the Nernst–Einstein conductivity

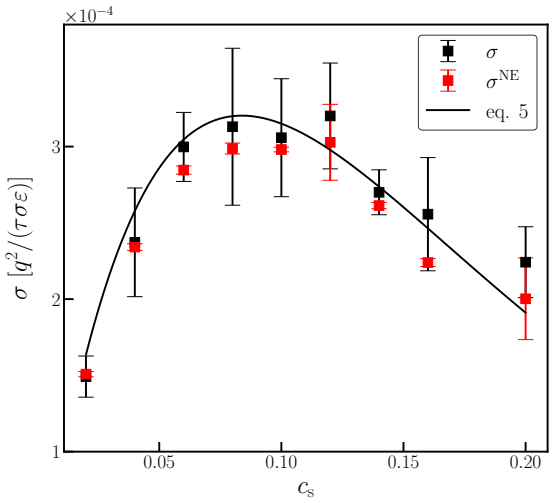

Figure 2.4: Ion conductivity, σ, as a function of salt concentration, c_s, at temperature $T = 1.0$. We include the true conductivity, σ, the Nernst–Einstein conductivity, σ^{NE}, and the conductivity based on eq. (2.5).

is very close to the true conductivity, confirming that ion–ion correlation is unimportant for this system. Both experimental and simulation studies have reported similar results [4, 11, 37, 38], with inverse Haven ratios close to unity for this type of system.

Based on the fitted exponential dependence of the friction coefficient at high temperatures, Ref. [8] proposed the following expression for the salt concentration dependence of the conductivity:

$$\sigma = \lambda c_s \exp\left(-\frac{c_s}{c_s^{max}}\right) \tag{2.5}$$

where c_s^{max} is obtained from fitting the friction coefficient. Our data at $T = 1.0$ shown in Figure 2.4 can be reasonably described by this expression. Later work by the same group [39] found that at lower temperatures, eq. (2.5) could still fit the experimental data; however, the coefficients λ and c_s^{max} were treated as purely fitting parameters *for each temperature* and no connection was made with the segmental friction.

Since the conductivity is well approximated by the Nernst–Einstein conductivity, and since the ratio of the sum of the cation and anion diffusivities to the polymer diffusivity remains essentially independent of the salt concentration for a given temperature, we hypothesize that using the M-VFT equation (eq. (2.2)) for the

polymer diffusivity would allow a unified description of the conductivity for any temperature and salt concentration. Thus, we propose:

$$\sigma = \lambda(T) c_s \frac{D_P}{D_P(0)} \tag{2.6}$$

where D_P is given by eq. (2.2) and $D_P(0) = D_P(c_s = 0)$. $\lambda(T)$ corresponds to the specific conductivity at infinite dilution at temperature T, which can be directly calculated from performing simulations at very low salt concentrations, or treated as a fitting parameter. In the Appendix, we show data for $\lambda(T)$ obtained using both methods, with good agreement. For our numerical fitting using eq. (2.6), we adopt the value obtained from fitting.

In Figure 2.5a, we present the simulation data (symbols) for the ion conductivity as a function of salt concentration for various temperatures; in the same figure, we show the results of fitting using eq. (2.6) (lines). As expected, the ion conductivity decreases as the temperature is decreased, while the characteristic non-monotonic dependence is found for all temperatures. The maximum in the conductivity shifts to lower concentrations as the temperature decreases, in agreement with experiments [39]. All these trends are captured by eq. (2.6), which yields nearly quantitative agreement with the simulation data.

As a global measure of the quality of fitting the data using eq. (2.6), in Figure 2.5b we plot the ratio of the specific conductivity σ/c_s to its infinite dilution value $\lambda(T)$ vs. the ratio of the polymer diffusivity $D_P/D_P(0)$ on a log–log scale. All the data fall on the same curve, with an R-squared value of 0.989. This result is strong indication that the salt concentration dependence in the ion conductivity is governed by the segmental dynamics of the polymer for all the temperatures and salt concentrations examined in our work.

In the literature, the temperature dependence of the ion conductivity in amorphous polymeric materials is widely fitted to the VFT equation [40–42]:

$$\sigma = A \exp\left(-\frac{E_a}{T - T_0}\right) \tag{2.7}$$

where A and E_a are both fitting parameters, and the Vogel temperature T_0 is typically taken to be 50 K below T_g, or treated as a fitting parameter. In the Appendix, we show the simulation data for the conductivity and the VFT fitting as a function of $1/T$ for different salt concentrations. While VFT provides a good fit to simulation data,

we emphasize that the VFT parameters have to be fitted *for each salt concentration*, and their resulting dependence on the salt concentration exhibits behaviors that are difficult to justify on physical grounds, as shown and discussed in Appendix. We believe the unusual behaviors of these fitting parameters with salt concentration, also reported in experimental studies [28], raise doubt about the physical basis in the VFT for describing the conductivity data in salt-doped polymers.

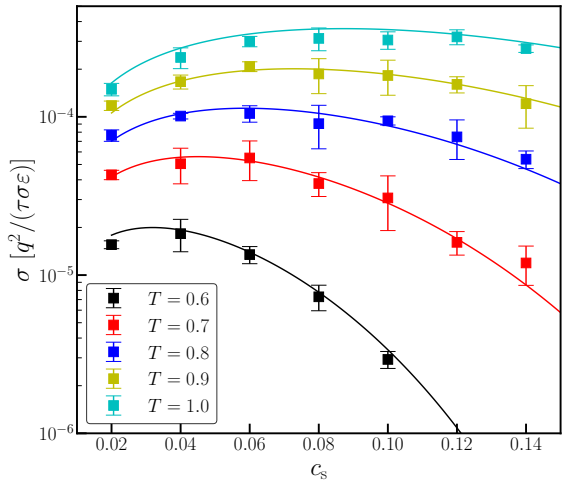

(a)

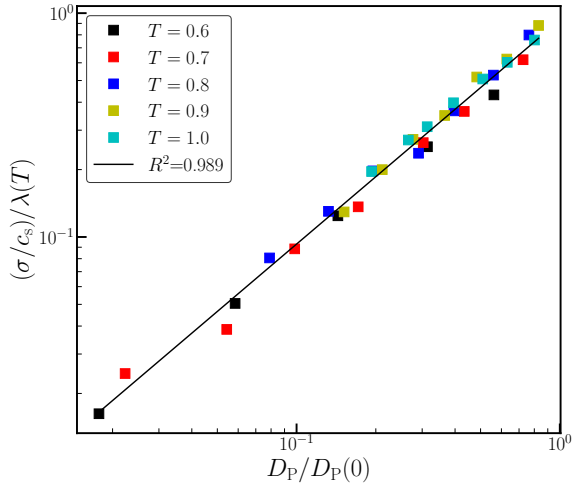

(b)

Figure 2.5: (a) Ion conductivity, σ, as a function of salt concentration, c_s, for various temperatures, (b) Ratio of the specific conductivities correlates well with the ratio of polymer center-of-mass diffusivity.

2.3 Conclusions

In summary, by examining the salt concentration effects on the glass transition of the polymer, we propose a modified VFT equation for the polymer segmental mobility. Using the M-VFT equation, we provide a simple formula, eq. (2.6), that accurately captures the conductivity data for all the temperatures and salt concentrations studied in our simulation, and affords a straightforward physical interpretation. The complex concentration and temperature dependence in eq. (2.6) cannot be captured by either eq. (2.5) or eq. (2.7) without using parameters that must be fitted for each temperature or concentration and that lack consistent physical interpretation. Interestingly, while lowering the temperature and increasing the salt concentration both slow down the segmental dynamics, we note that eq. (2.6) does not follow a simple salt–temperature superposition as found in other systems such as ionomers [43]. A possible reason for this difference may be that the salt concentration in the salt-doped polymer systems has a different role from the temperature, in that it alters the activation energy in the VFT equation, in addition to changing T_g. Our study highlights the nontrivial synergistic effects of salt concentration and temperature on the segmental dynamics of polymers and ion conductivity, and the role of the glass transition temperature, in salt-doped polymer systems.

2.4 Appendix

Simulation Details

Our simulations include 400 polymer chains, each with 30 neutral monomer beads and are conducted using Lennard–Jones (LJ) units. We choose the LJ parameter ϵ to correspond to $k_B T$ at $T = 400$K. Thus, the reduced temperature $T = 1.0$ corresponds to $T = 400$K. This correspondence yields a glass transition temperature that falls within the known values of the glass transition temperature for PEO [22]. Following previous studies [14], the salt concentration mapping from LJ units to real units is $2c_s^{LJ} = c_s^{real} \equiv c_s$, where c_s is defined as the ratio $[Li^+]/[EO]$. To compare with experiments, we report the salt concentration in real units. The length scale σ is taken as 0.7nm. All particles have the same mass $m = 1.0$.

All particles interact via the Lennard–Jones potential:

$$U_{LJ}(r_{ij}) = \begin{cases} 4\epsilon_{ij}\left[\left(\frac{\sigma_{ij}}{r_{ij}}\right)^{12} - \left(\frac{\sigma_{ij}}{r_{ij}}\right)^{6} - \left(\frac{\sigma_{ij}}{r_c}\right)^{12} + \left(\frac{\sigma_{ij}}{r_c}\right)^{6}\right], & r_{ij} \le r_c \\ 0, & r_{ij} > r_c \end{cases} \tag{2.8}$$

where r_{ij} is the distance between two particles. We choose the same LJ interaction energy between all pairs $\epsilon_{ij} = \epsilon$ and set σ_{ij} to be the mean particle size $\sigma_{ij} =$

$(\sigma_i + \sigma_j)/2$. To approximate the size difference between the Li^+ cation, $TFSI^-$ anion, and EO monomers in the PEO/LiTFSI system, we choose the polymer bead size to be 1.0σ, the cation diameter $\sigma_+ = 0.4\sigma$, and the anion diameter $\sigma_- = 1.6\sigma$. For the ion–ion, ion–monomer and bonded monomer–monomer interactions, the cutoff distance is $r_c = 2^{1/6}\sigma_{ij}$, corresponding to the repulsive Weeks–Chandler–Andsersen potential [44]. For non-bonded monomer–monomer interactions we choose $r_c = 2.0\sigma$, so that the interaction includes the attractive portion of the potential, which is essential to reproduce the glass transition phenomenon [18].

The chain connectivity is modeled using the finitely extensible nonlinear elastic potential (FENE) [16, 17] between consecutive beads along the chain backbone:

$$U_{FENE}(r_{ij}) = -\frac{1}{2}KR_0 \ln\left(1 - \frac{r_{ij}^2}{R_0^2}\right) \tag{2.9}$$

We choose the standard values $K = 30\epsilon/\sigma^2$ for the spring constant, and $R_0 = 1.5\sigma$ for the cutoff radius.

The strong ion–ether oxygen interaction in the lithium salt-doped PEO systems is captured by a solvation potential proposed by Hall and coworkers [15, 45]:

$$U_{SOLV}(r_{ij}) = \begin{cases} -S_{ij}\left[\left(\frac{\sigma_{ij}}{r_{ij}}\right)^4 - \left(\frac{\sigma_{ij}}{r_c}\right)^4\right], & r_{ij} \le r_c \\ 0, & r_{ij} > r_c \end{cases} \tag{2.10}$$

Following these authors, we choose $S_{ij} = 4.33$ and $r_c = 5.0\sigma$.

Ion–ion interactions are described by the Coulomb potential

$$U_{COUL}(r_{ij}) = \frac{q_i q_j}{4\pi\varepsilon_0\varepsilon_r r_{ij}} \tag{2.11}$$

where q_i is the charge of ion i, ε_0 is the vacuum permittivity, and ε_r is the dielectric constant of the polymer host medium. For the temperature range studied we choose constant $\varepsilon_r = 7.5$, corresponding to the dielectric constant of PEO [14].

All simulations were performed on the LAMMPS platform [46]. We used the velocity-Verlet algorithm with a time step of 0.005τ; where τ is the LJ time defined by $\sigma\sqrt{m/\epsilon}$. The Coulomb interactions were evaluated using a particle–particle particle–mesh Ewald solver [47]. To control the temperature and pressure of the system we use the Nosé–Hoover barostat and thermostat [48], with a damping

constant of 1.0τ. The pressure is set to $p = 0.0\varepsilon\sigma^{-3}$. [19] For all our simulations, we prepared fully equilibrated systems at $T = 1.0$ for the range of salt concentrations studied. To examine the temperature dependence and glass transition, we took these equilibrated configurations for the different salt concentrations at $T = 1.0$ and applied a constant cooling rate [49] $\Delta T/\Delta t = -0.5 \times 10^{-7}/\tau$ to the desired temperatures. Data were collected by further equilibration at each of the desired temperature values. The results were obtained by block averaging with at least four statistically uncorrelated blocks, where the polymer and ions reached the diffusive regime in each block.

Determination of the Glass Transition

In Figure 2.6a, we show the system volume, V, as a function of temperature, T, for various salt concentrations. Each set of data exhibit two distinct slopes. By linearly fitting the volume data at low and high temperatures, we determine T_{g} from the crossing of the two straight lines.

To map the T_{g} of our simulation to that for the PEO/LiTFSI system, we invoke the requirement that our T_{g} in the absence of salt match the T_{g} of the neat polymer in experiments. Since T_{g} depends on the degree of polymerization, we use the Fox–Flory equation to determine the T_{g} corresponding to the chain length in our study, taking data from experiments at different chain lengths [50]. We find that $T_{\mathrm{g}} = 0.426$ in reduced units for our chain length without salt corresponds to $T_{\mathrm{g}} = 192.3K$. Thus, in our study, a reduced temperature of $T = 1.0$ can alternatively be mapped to $T \simeq 450K$. In Figure 2.6b, we show T_{g} in real units along with experimental data [22]. Recent simulation study has shown similar trend in the T_{g} dependence on salt concentration [51]. Since our model parameters are not tuned to quantitatively reproduce properties of the PEO/LiTFSI system, and since the experiment used a different chain length, we do not expect quantitative agreement.

The increase in T_{g} with salt mole fraction can be attributed to the strong ion–polymer complexation, that leads to restricted motion of the polymer backbone, and to the decreased partial molar volume of the polymer as shown in Figure 2.6c. The monotonic behavior of $\overline{V}_p$ is found for all studied temperatures (below and above T_{g}).

Ion–Polymer Coordination

In Figure 2.7, we show that the self-diffusion coefficients of the cation, anion, and polymer center–of–mass decrease with increasing salt concentration, c_{s}. This

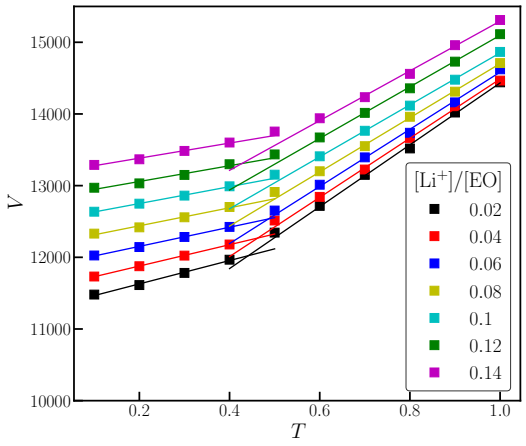

(a)

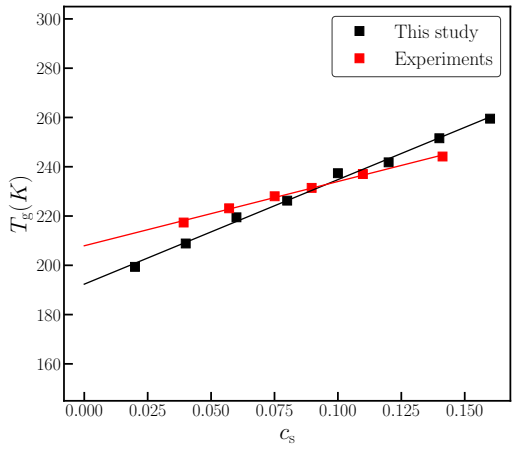

(b)

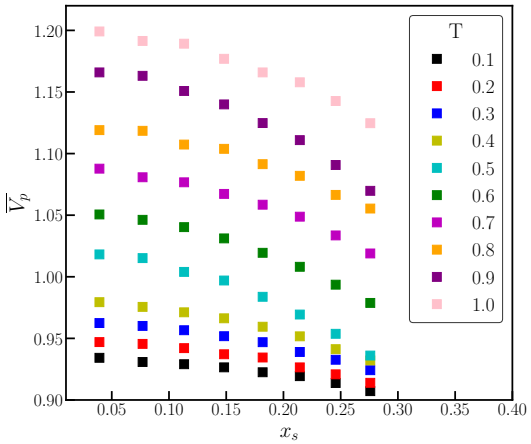

(c)

Figure 2.6: (a) System Volume, V, as a function of temperature, T, (b) Glass transition temperature T_g, as a function of salt concentration, c_s, from experiments [22] and this work, (c) Polymer partial molar volume as a function of salt mole fraction.

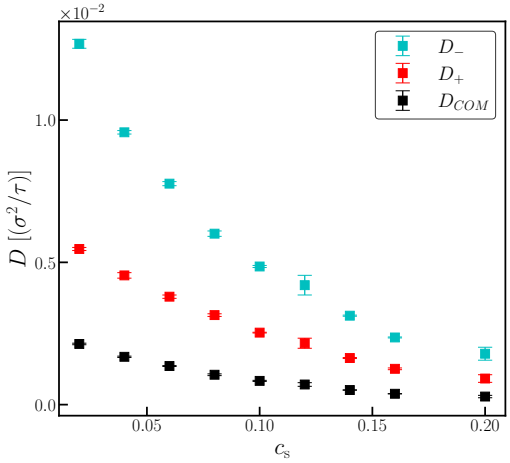

Figure 2.7: Self-diffusion coefficient, D, as a function of salt concentration, c_s, for the anion, cation, and polymer center of mass, at temperature $T = 1.0$.

reflects the slowdown of the segmental dynamics due to the strong ion–polymer coupling [4].

In Figure 2.8, we show the cation–polymer and the cation–anion radial distribution function $g(r)$, for $c_s = 0.02$ and $c_s = 0.16$. For both concentrations, the peak height of the cation-polymer $g(r)$ is much higher than the peak height of the cation-anion $g(r)$. This result supports that the strong cation–polymer interaction leads to seclusion of the cation from forming ion pairs and clusters with the bulky anion in our model system.

Rouse-Mode Analysis and Friction Coefficient

In Figure 2.9 we show the normal modes' relaxation times, τ_p, at $T = 1.0$ and $T = 0.6$, for salt concentration $c_s = 0.1$. The normal mode analysis is described in Refs. [52, 53]. We find that at $T = 1.0$, τ_p follows the expected p^{-2} Rouse scaling. However, at $T = 0.6$ there is a clear deviation from the Rouse prediction. Specifically, there is a transition at some intermediate mode from p^{-2} to $p^{-3/2}$. The relationship between the location of the crossover and the temperature or salt concentration will be explored in future work.

In Figure 2.10, we show the monomeric friction coefficient calculated from the Rouse model:

$$\zeta = \frac{k_B T}{N D_P} \tag{2.12}$$

All results are normalized by the friction coefficient of the pure polymer melt.

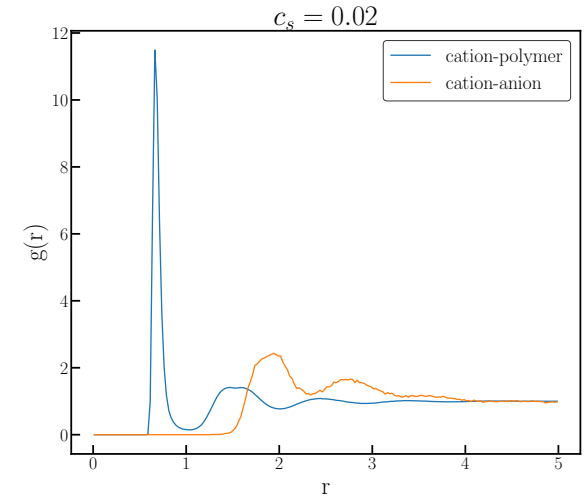

(a)

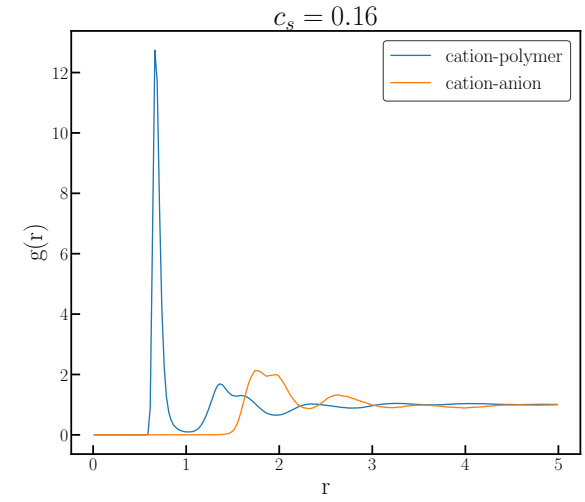

(b)

Figure 2.8: The cation–polymer and cation–anion radial distribution functions at (a) $c_s = 0.02$ and (b) $c_s = 0.16$.

With decreasing temperature, the salt concentration dependence of ζ changes from exponential to super-exponential. Due to this deviation, in the main text we have quantified the segmental dynamics using the modified-VFT equation for the polymer diffusion coefficient, instead of an exponential dependence on salt concentration for ζ.

Specific Conductivity at Infinite Dilution

In Figure 2.11, we show the specific conductivity at infinite dilution, λ, as a function of temperature. We determine λ by fitting our conductivity data to eq. 2.6, and by conducting molecular simulations at very low salt concentrations ($c_s = 0.00016$).

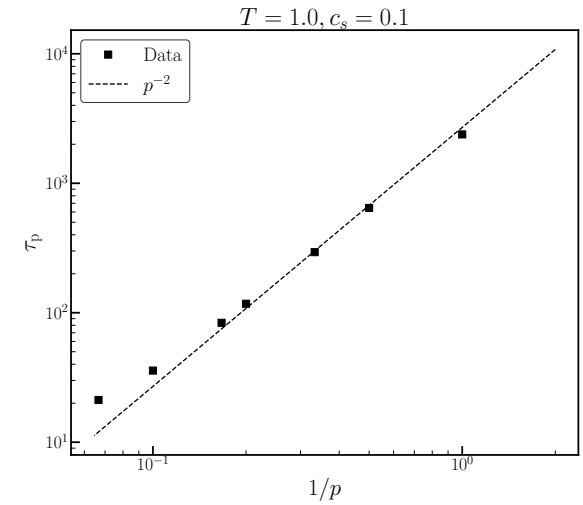

(a)

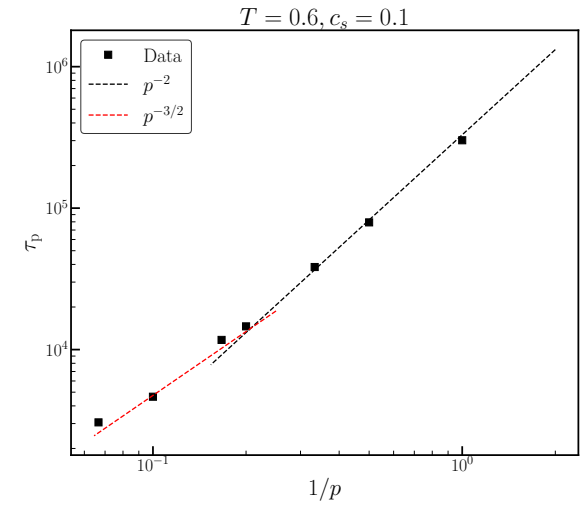

(b)

Figure 2.9: Effective relaxation times plotted as a function of 1/p for (a) $T = 1.0$ and (b) $T = 0.6$.

We find good agreement between the two methods for all the studied temperatures.

VFT Analysis

In Figure 2.12, we present the ionic conductivity as a function of $1/T$ for various salt concentrations. The symbols are the simulation data, and the lines are the results of fitting using the VFT equation:

$$\sigma = A\exp\left(-\frac{E_a}{T - T_0}\right) \tag{2.13}$$

where A is a prefactor commonly associated with the charge carrier concentration, E_a is a pseudoactivation energy related to the segmental relaxation, and T_0 is the

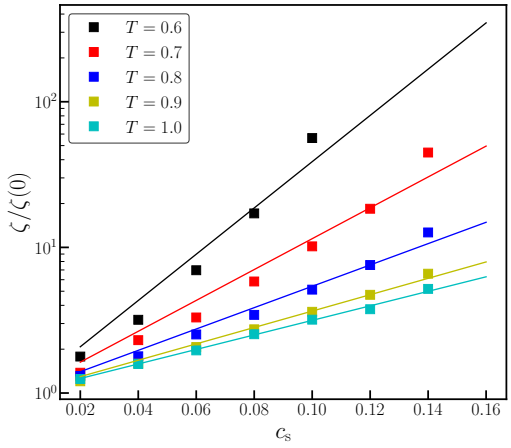

Figure 2.10: Normalized friction coefficient, $\zeta/\zeta(0)$, as a function of salt concentration, c_s, for various temperatures.

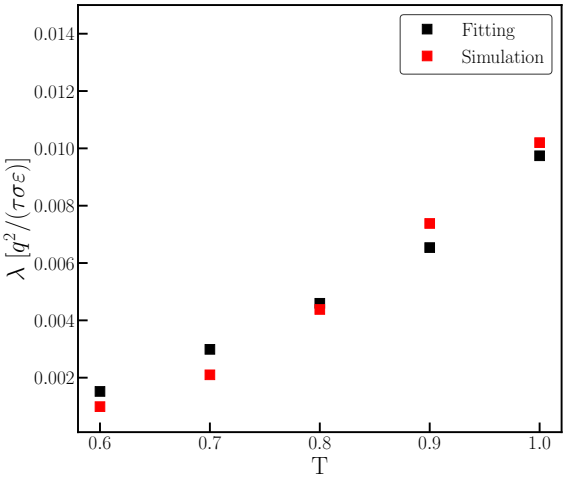

Figure 2.11: Specific Conductivity at infinite dilution as a function of temperature, calculated from fitting eq. 2.6 and conducting simulations at very low concentration.

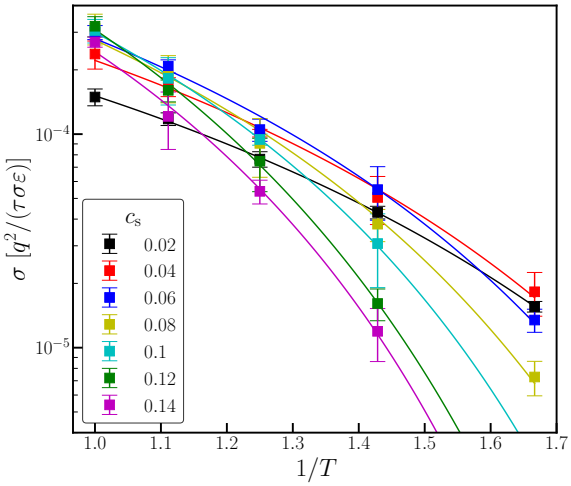

Figure 2.12: Ionic conductivity as a function of 1/T for various salt concentrations. The curves are results from fitting using scheme 1; the results are indistinguishable from those using schemes 2 and 3.

equilibrium glass transition temperature, typically taken 50 K below T_g [40–42]. We fit our simulation data using 3 different schemes: (1) We consider $T_0 = T_g - 0.125$, where T_g is the glass transition temperature shown in Fig. 1 of the main text and 0.125 corresponds to 50 K in reduced units; (2) we consider T_0 to be predetermined from fitting the polymer diffusivity in eq. 2.6 of the main text; (3) T_0 is taken as a free fitting parameter. In all methods, A and E_a are considered fitting parameters.

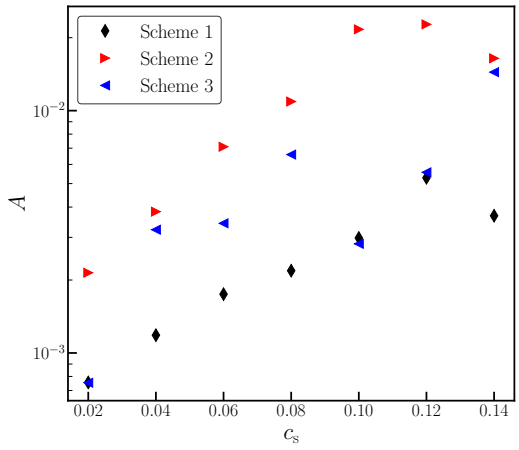

(a)

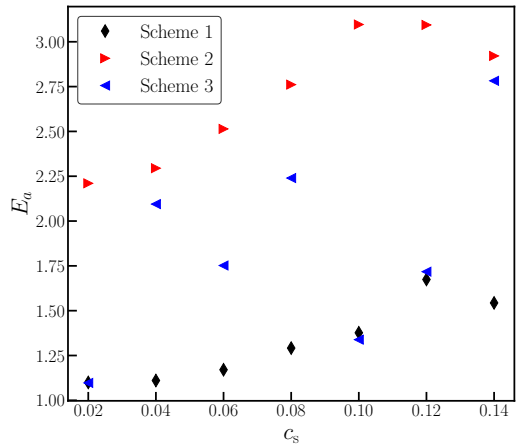

(b)

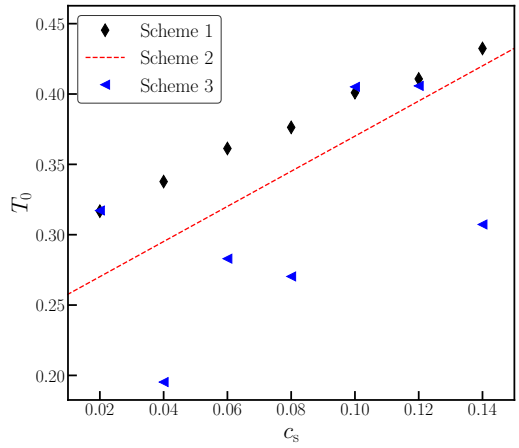

(c)

Figure 2.13: VFT parameters, (a) A (b) E_a and (c) T_0 calculated as a function of salt concentration, c_s, using the three different fitting methods.

In Figure 2.13, we show the parameters A, E_a, and T_0 as function of salt concentration, c_s. We observe that for fitting schemes 1 and 2, both A and E_a exhibit a non-linear and non-monotonic dependence on c_s. The non-monotonic behavior in both A and E_a are difficult to justify on physical grounds, given that our model does not have strong ion–ion correlations. Fitting scheme 3 yields a rather irregular dependence of T_0 on c_s, as shown in Figure 2.13c. The fitted values of T_0 fail to have any meaningful connection to the glass transition temperature, and likewise we find unphysical fluctuations in A and E_a. The fact that three different fitting schemes with widely different values for the fitting parameters can yield nearly identical results to fit the conductivity data is strong evidence that the VFT fitting for the conductivity in salt-doped polymers lacks solid physical basis.

References

[1] Peled, E.; Menkin, S. *Journal of The Electrochemical Society* **2017**, *164*, A1703, DOI: 10.1149/2.1441707jes.

[2] Goodenough, J. B.; Kim, Y. *Chemistry of Materials* **2010**, *22*, 587–603, DOI: 10.1021/cm901452z.

[3] Hallinan, D. T.; Balsara, N. P. *Annual Review of Materials Research* **2013**, *43*, 503–525, DOI: 10.1146/annurev-matsci-071312-121705.

[4] Borodin, O.; Smith, G. D. *Macromolecules* **2006**, *39*, 1620–1629, DOI: 10.1021/ma052277v.

[5] Maitra, A.; Heuer, A. *Physical Review Letters* **2007**, *98*, 227802, DOI: 10.1103/PhysRevLett.98.227802.

[6] Maitra, A.; Heuer, A. *Macromolecular Chemistry and Physics* **2007**, *208*, 2215–2221, DOI: 10.1002/macp.200700265.

[7] Molinari, N.; Mailoa, J. P.; Kozinsky, B. *Chemistry of Materials* **2018**, *30*, 6298–6306, DOI: 10.1021/acs.chemmater.8b01955.

[8] Mongcopa, K. I. S.; Tyagi, M.; Mailoa, J. P.; Samsonidze, G.; Kozinsky, B.; Mullin, S. A.; Gribble, D. A.; Watanabe, H.; Balsara, N. P. *ACS Macro Letters* **2018**, *7*, 504–508, DOI: 10.1021/acsmacrolett.8b00159.

[9] Mongcopa, K. I. S.; Gribble, D. A.; Loo, W. S.; Tyagi, M.; Mullin, S. A.; Balsara, N. P. *Macromolecules* **2020**, *53*, 2406–2411, DOI: 10.1021/acs.macromol.0c00091.

[10] Webb, M. A.; Yamamoto, U.; Savoie, B. M.; Wang, Z.-G.; Miller, T. F. *ACS Macro Letters* **2018**, *7*, 734–738, DOI: 10.1021/acsmacrolett.8b00237.

[11] Wheatle, B. K.; Lynd, N. A.; Ganesan, V. *ACS Macro Letters* **2018**, *7*, 1149–1154, DOI: 10.1021/acsmacrolett.8b00594.

[12] Wheatle, B. K.; Lynd, N. A.; Ganesan, V. *Macromolecules* **2020**, *53*, 875–884, DOI: 10.1021/acs.macromol.9b02510.

[13] Shen, K.-H.; Hall, L. M. *Macromolecules* **2020**, *53*, 10086–10096, DOI: 10.1021/acs.macromol.0c02161.

[14] Shen, K.-H.; Hall, L. M. *Macromolecules* **2020**, *53*, 3655–3668, DOI: 10.1021/acs.macromol.0c00216.

[15] Shen, K.-H.; Fan, M.; Hall, L. M. *Macromolecules* **2021**, *54*, 2031–2052, DOI: 10.1021/acs.macromol.0c02557.

[16] Grest, G. S.; Lacasse, M.-D.; Kremer, K.; Gupta, A. M. *The Journal of Chemical Physics* **1996**, *105*, 10583–10594, DOI: 10.1063/1.472978.

[17] Kremer, K.; Grest, G. S. *The Journal of Chemical Physics* **1990**, *92*, 5057–5086, DOI: 10.1063/1.458541.

[18] Morita, H.; Tanaka, K.; Kajiyama, T.; Nishi, T.; Doi, M. *Macromolecules* **2006**, *39*, 6233–6237, DOI: 10.1021/ma052632h.

[19] Hsu, H.-P.; Kremer, K. *The Journal of Chemical Physics* **2019**, *150*, 091101, DOI: 10.1063/1.5089417.

[20] Buchholz, J.; Paul, W.; Varnik, F.; Binder, K. *The Journal of Chemical Physics* **2002**, *117*, 7364–7372, DOI: 10.1063/1.1508366.

[21] Grest, G. S. *The Journal of Chemical Physics* **2016**, *145*, 141101, DOI: 10.1063/1.4964617.

[22] Lascaud, S.; Perrier, M.; Vallee, A.; Besner, S.; Prud'homme, J.; Armand, M. *Macromolecules* **1994**, *27*, 7469–7477, DOI: 10.1021/ma00103a034.

[23] Nest, J.-F. L.; Gandini, A.; Cheradame, H. *British Polymer Journal* **1988**, *20*, 253–268, DOI: 10.1002/pi.4980200317.

[24] Fox, T. G.; Flory, P. J. *Journal of Applied Physics* **1950**, *21*, 581–591, DOI: 10.1063/1.1699711.

[25] Mogurampelly, S.; Sethuraman, V.; Pryamitsyn, V.; Ganesan, V. *The Journal of Chemical Physics* **2016**, *144*, 154905, DOI: 10.1063/1.4946047.

[26] Lin, E. Y.; Frischknecht, A. L.; Riggleman, R. A. *Macromolecules* **2021**, *54*, 5335–5343, DOI: 10.1021/acs.macromol.1c00206.

[27] Diederichsen, K. M.; Buss, H. G.; McCloskey, B. D. *Macromolecules* **2017**, *50*, 3831–3840, DOI: 10.1021/acs.macromol.7b00423.

[28] Chintapalli, M.; Le, T. N. P.; Venkatesan, N. R.; Mackay, N. G.; Rojas, A. A.; Thelen, J. L.; Chen, X. C.; Devaux, D.; Balsara, N. P. *Macromolecules* **2016**, *49*, 1770–1780, DOI: 10.1021/acs.macromol.5b02620.

[29] Zhang, Y.; Maginn, E. J. *The Journal of Physical Chemistry Letters* **2015**, *6*, 700–705, DOI: 10.1021/acs.jpclett.5b00003.

[30] McDaniel, J. G.; Son, C. Y. *The Journal of Physical Chemistry B* **2018**, *122*, 7154–7169, DOI: 10.1021/acs.jpcb.8b04886.

[31] Son, C. Y.; Wang, Z.-G. *The Journal of Chemical Physics* **2020**, *153*, 100903, DOI: 10.1063/5.0016163.

[32] Mao, G.; Saboungi, M.-L.; Price, D. L.; Armand, M. B.; Howells, W. S. *Physical Review Letters* **2000**, *84*, 5536–5539, DOI: 10.1103/PhysRevLett.84.5536.

[33] Gouverneur, M.; Schmidt, F.; Schönhoff, M. *Physical Chemistry Chemical Physics* **2018**, *20*, 7470–7478, DOI: 10.1039/C7CP08580J.

[34] Shao, Y.; Gudla, H.; Brandell, D.; Zhang, C. *Journal of the American Chemical Society* **2022**, *144*, 7583–7587, DOI: 10.1021/jacs.2c02389.

[35] Kilchert, F.; Lorenz, M.; Schammer, M.; Nürnberg, P.; Schönhoff, M.; Latz, A.; Horstmann, B. *Physical Chemistry Chemical Physics* **2023**, *25*, 25965–25978, DOI: 10.1039/D2CP04423D.

[36] Fang, C.; Mistry, A.; Srinivasan, V.; Balsara, N. P.; Wang, R. *JACS Au* **2023**, *3*, 306–315, DOI: 10.1021/jacsau.2c00590.

[37] Bocharova, V.; Sokolov, A. P. *Macromolecules* **2020**, *53*, 4141–4157, DOI: 10.1021/acs.macromol.9b02742.

[38] Timachova, K.; Chintapalli, M.; Olson, K. R.; Mecham, S. J.; DeSimone, J. M.; Balsara, N. P. *Soft Matter* **2017**, *13*, 5389–5396, DOI: 10.1039/C7SM00794A.

[39] Hoffman, Z. J.; Shah, D. B.; Balsara, N. P. *Solid State Ionics* **2021**, *370*, 115751, DOI: 10.1016/j.ssi.2021.115751.

[40] Thomas, E. M.; Nguyen, P. H.; Jones, S. D.; Chabinyc, M. L.; Segalman, R. A. *Annual Review of Materials Research* **2021**, *51*, 1–20, DOI: 10.1146/annurev-matsci-080619-110405.

[41] Albinsson, I.; Mellander, B.-E.; Stevens, J. R. *The Journal of Chemical Physics* **1992**, *96*, 681–690, DOI: 10.1063/1.462453.

[42] Ratner, M. A.; Nitzan, A. *Faraday Discussions of the Chemical Society* **1989**, *88*, 19–42, DOI: 10.1039/DC9898800019.

[43] Zhang, S.; Dou, S.; Colby, R. H.; Runt, J. *Journal of Non-Crystalline Solids* **2005**, *351*, 2825–2830, DOI: 10.1016/j.jnoncrysol.2005.03.075.

[44] Weeks, J. D.; Chandler, D.; Andersen, H. C. *The Journal of Chemical Physics* **1971**, *54*, 5237–5247, DOI: 10.1063/1.1674820.

[45] Brown, J. R.; Seo, Y.; Hall, L. M. *Physical Review Letters* **2018**, *120*, 127801, DOI: 10.1103/PhysRevLett.120.127801.

[46] Plimpton, S. *Journal of Computational Physics* **1995**, *117*, 1–19, DOI: 10.1006/jcph.1995.1039.

[47] Brown, W. M.; Kohlmeyer, A.; Plimpton, S. J.; Tharrington, A. N. *Computer Physics Communications* **2012**, *183*, 449–459, DOI: 10.1016/j.cpc.2011.10.012.

[48] Martyna, G. J.; Tuckerman, M. E.; Tobias, D. J.; Klein, M. L. *Molecular Physics* **1996**, *87*, 1117–1157, DOI: 10.1080/00268979600100761.

[49] Li, W.; Olvera de la Cruz, M. *Soft Matter* **2021**, *17*, 8420–8433, DOI: 10.1039/D1SM01098K.

[50] Niedzwiedz, K.; Wischnewski, A.; Pyckhout-Hintzen, W.; Allgaier, J.; Richter, D.; Faraone, A. *Macromolecules* **2008**, *41*, 4866–4872, DOI: 10.1021/ma800446n.

[51] Fang, C.; Yu, X.; Chakraborty, S.; Balsara, N. P.; Wang, R. *ACS Macro Letters* **2023**, *12*, 612–618, DOI: 10.1021/acsmacrolett.3c00041.

[52] Hsu, H.-P.; Kremer, K. *The European Physical Journal Special Topics* **2017**, *226*, 693–703, DOI: 10.1140/epjst/e2016-60322-5.

[53] Kalathi, J. T.; Kumar, S. K.; Rubinstein, M.; Grest, G. S. *Soft Matter* **2015**, *11*, 4123–4132, DOI: 10.1039/C5SM00754B.

Chapter 3

CHAIN DYNAMICS AND CONDUCTIVITY OF POLYMERIZED IONIC LIQUIDS: EFFECTS OF ELECTROSTATIC CORRELATION AND CHAIN LENGTH

Polymerized ionic liquids (PILs) exhibit complex ion transport dynamics that are central to advancing energy storage design. In this work, we employ coarse-grained molecular dynamics simulations with smeared electrostatics and mass to isolate the role of electrostatic correlations and chain length on ion transport in solvent-free PILs. This model enables access to long chain lengths and entangled regimes, and is constructed such that it eliminates glassy slowdown. We find that introducing electrostatics slightly stiffens the polymer chains, slows their relaxation, and reduces diffusivity. Nevertheless, the charged system retains ideal chain statistics and exhibits the same Rouse-to-reptation crossover observed in the analogous uncharged system. Moreover, although polyanion diffusivity decreases sharply with chain length, the ion conductivity remains nearly constant. Analysis of the Onsager transport coefficients reveals that this behavior arises from a competition between the slowdown of polymer diffusion and enhanced interchain correlations. This competition and the resulting conductivity behavior persist even in the absence of electrostatic interactions, highlighting the role of melt incompressibility rather than charge-mediated effects. These findings reveal an intrinsic decoupling between charge transport and chain relaxation that does not rely on glass transition, suggesting that mechanical properties can in principle be tuned via the chain length without compromising conductivity.

This chapter includes content from our previously published article:

[1] Stewart, C. J.*; Tsamopoulos, A. J.*; Ye, B. B.; Wang, Z.-G. *The Journal of Chemical Physics* **2025**, *163*, DOI: 10.1063/5.0297386 * Denotes equal contribution.

3.1 Introduction

Polymerized ionic liquids (PILs) have gained increasing research interest as charge-dense materials with applications in energy storage [1, 2], separation membranes [3, 4], and sensors [5]. Composed of ionically charged monomer units and their counterions, PILs offer chemical stability, low flammability, and enhanced mechanical robustness [6, 7]. However, their ion conductivity is intrinsically limited, typically falling well below that of their monomeric analogs [8]. Even in favorable cases, such as poly(imidazolium) systems with TFSI counterions, the conductivity remains modest, reaching only 4×10^{-4} S cm^{-1} at 60°C [7], which is comparable to that of PEO-based polymer electrolytes [9] but far below the threshold required for high-performance devices [10]. Recent synthetic advances have enabled systematic structural tuning of PILs [11], but challenges remain in achieving conductivities comparable to those of ionic liquids. One key limitation is their elevated glass transition temperature (T_g), which often exceeds 100°C and is well above the typical operating range of Li-ion batteries [12–15]. Below this temperature, PILs enter a glassy state where ion transport is severely hindered [16–18]. T_g increases with chain length [19–21], making it difficult to disentangle the intrinsic effects of chain length from those arising due to glass formation [22]. Furthermore, changes in temperatures in experimental studies necessarily alter the strength of electrostatic interactions, further complicating the decoupling [12]. Fan et al. [23] systematically studied the effect of chain length on ion transport in PILs over a wide range of molecular weights. They found that while conductivity decreases sharply upon polymerization, its dependence on chain length beyond $N \sim 10$ is minimal, even as T_g, viscosity, and fragility increase, suggesting that ion transport becomes increasingly decoupled from segmental relaxation. Zhang et al. [24] reported a similar decrease in conductivity in molecular dynamics (MD) simulations comparing an ionic liquid and an oligomeric PIL, consistent with the widely observed trend that polymerization suppresses conductivity. However, this trend is not universal.

Frenzel et al. [25] reported a PAAPS-based PIL in which conductivity increases with molecular weight, a surprising result they attribute to a glass-transition-assisted hopping mechanism and enhanced intrachain correlations. This enhancement persists even when the structural relaxation times remain constant, suggesting that intrachain dynamics can compensate for the reduced segmental mobility. Similarly, Griffin et al. [26] observed that a trisaminocyclopropenium-based PIL outperforms its monomeric analogue at ambient temperature, while MD simulations using the Kremer–Grest model have predicted an initial increase in conductivity at short chain

lengths, followed by a plateau [27]. However, the chain length in the MD study was limited to $N \leq 25$, and it was challenging to draw conclusions about the dependence on chain length due to the high uncertainty in the data. These findings highlight the need for a mechanistic framework that isolates chain connectivity and ion–ion correlation from glassy dynamics.

In this work, we conduct coarse-grained molecular dynamics simulations using the Gaussian core model with smeared electrostatics (GCMe) [28–31] to investigate the effect of chain length and electrostatic correlations on ion transport in PILs. Unlike atomistic simulations, which inherently capture glassy behavior and require significant computational resources to probe marginally entangled regimes [32, 33], GCMe permits large time steps and soft particle overlap, enabling simulations of long polymer chains and entangled regimes at high densities. Combined with the GPU acceleration available in OpenMM [31, 34], GCMe accesses longer time scales and larger system sizes than would be feasible with atomistic models. Given the experimental difficulty of isolating the impact of chain length, glass transition, and temperature-dependent electrostatics on ion transport, our approach provides a way to suppress glassy dynamics and thereby disentangle their influence on polymer segmental motion and ion transport.

By comparing PILs with their uncharged counterparts, we quantify the effect of electrostatic correlations and chain length on polymer dynamics and ion transport. We find that introducing electrostatics stiffens the polymer chain, slows relaxation, and reduces diffusivity. Nevertheless, the qualitative dynamics remain unchanged: both charged and uncharged systems follow ideal chain statistics and exhibit a clear crossover from Rouse to reptation dynamics with increasing chain length. Despite a sharp decrease in the polymer diffusivity with increasing chain length, ion conductivity remains largely unchanged due to enhanced interchain correlations that compensate for the reduced polymer mobility. This behavior points to a decoupling between charge transport and chain relaxation that is driven not by glassy dynamics but by collective effects intrinsic to dense polymer systems due to incompressibility. Together, these results provide a new perspective for interpreting conductivity behavior in dense ionic systems in both unentangled and entangled regimes.

3.2 Theory

Onsager Transport Coefficients

The Onsager transport framework provides a set of linear relations that link thermodynamic driving forces to the resulting fluxes, fully characterizing transport phenomena in electrolytes [1, 35]. This framework is especially useful for systems where the ideal Nernst–Einstein relation breaks down due to significant ion–ion correlations.

In this formalism, the flux $\mathbf{J}_i$ of species i is related to the gradient in the electrochemical potential $\bar{\mu}_j$ of species j by

$$\mathbf{J}_i = -\sum_j L_{ij} \nabla \bar{\mu}_j, \tag{3.1}$$

where L_{ij} are the Onsager transport coefficients. The Onsager reciprocal relations require $L_{ij} = L_{ji}$. Furthermore, mass conservation imposes the additional constraint $\sum_i M_i L_{ij} = 0$, where M_i is the molecular weight of species i. This ensures that the total mass flux vanishes in a closed system with purely diffusive transport.

For concreteness, we consider a PIL comprising polyanions with their monomeric counterions. Assuming the polyanion monomers and cations have equal mass, mass conservation enforces $L_{--} + L_{+-} = 0$, reducing the system to a single degree of freedom: $L_{--} = L_{++} = -L_{+-}$. This relationship intrinsically couples the magnitudes of the Onsager coefficients, so that a change in one directly necessitates an equal compensatory change in the others. The magnitude and sign of a coefficient convey the extent of correlated or anticorrelated motion. More positive values indicate stronger correlation, while more negative values indicate stronger anticorrelation.

The Onsager transport coefficient between species i and j can be calculated from the particle positions using the Einstein relation

$$\begin{aligned} L_{ij} = \frac{1}{6 k_\mathrm{B} T V} \lim_{t\to\infty} \frac{d}{dt} \Bigg\langle \sum_\alpha \sum_\beta \big[\mathbf{r}_{i,\alpha}(t) - \mathbf{r}_{i,\alpha}(0)\big] \\ \cdot \big[\mathbf{r}_{j,\beta}(t) - \mathbf{r}_{j,\beta}(0)\big] \Bigg\rangle, \end{aligned} \tag{3.2}$$

where α and β index all particles belonging to species i and j, respectively, k_B is the Boltzmann constant, T is the system temperature, and V is the system volume.

The diagonal coefficients ($i = j$) can be further partitioned into two components: $L_{ii} = L_{ii}^{\mathrm{self}} + L_{ii}^{\mathrm{dist}}$. The "self" terms L_{ii}^{self} ($\alpha = \beta$) capture the Nernst–Einstein

contributions to transport:

$$L_{ii}^{\text{self}} = \frac{1}{6k_{\text{B}}TV} \lim_{t\to\infty} \frac{d}{dt} \left\langle \sum_{\alpha} \left[\mathbf{r}_{i,\alpha}(t) - \mathbf{r}_{i,\alpha}(0)\right]^2 \right\rangle, \tag{3.3}$$

while the "distinct" terms L_{ii}^{dist} ($\alpha \neq \beta$) account for nonidealities arising from interparticle correlations:

$$\begin{aligned} L_{ii}^{\text{dist}} = \frac{1}{6\,k_{\text{B}}TV} \lim_{t\to\infty} \frac{d}{dt} \Bigg\langle \sum_{\alpha} \sum_{\beta\neq\alpha} \left[\mathbf{r}_{i,\alpha}(t) - \mathbf{r}_{i,\alpha}(0)\right] \\ \cdot \left[\mathbf{r}_{i,\beta}(t) - \mathbf{r}_{i,\beta}(0)\right] \Bigg\rangle, \end{aligned} \tag{3.4}$$

The self terms can be directly related to self-diffusion coefficients D_i through

$$L_{ii}^{\text{self}} = \frac{D_i n_i}{k_{\text{B}}T}. \tag{3.5}$$

where n_i is the number of particles belonging to species i, while the L_{--}^{dist} and L_{++}^{dist} terms account for interchain and cation interactions, respectively, not captured by the mean squared displacement.

The polyanion terms can be more naturally expressed in terms of the individual chain center of mass

$$\mathbf{R}_{\text{c}} = \frac{1}{N} \sum_{\gamma}^{N} \mathbf{r}_{\gamma}, \tag{3.6}$$

where γ indexes particles within a given chain and N is the chain length. The cross-terms are reexpressed as

$$\begin{aligned} L_{+-} = \frac{N}{6k_{\text{B}}TV} \lim_{t\to\infty} \frac{d}{dt} \Bigg\langle \sum_{\alpha} \sum_{b} \left[\mathbf{r}_{+,\alpha}(t) - \mathbf{r}_{+,\alpha}(0)\right] \\ \cdot \left[\mathbf{R}_{\text{c},b}(t) - \mathbf{R}_{\text{c},b}(0)\right] \Bigg\rangle, \end{aligned} \tag{3.7}$$

while the polyanion-only terms become

$$\begin{aligned} L_{--} = \frac{N^2}{6k_{\text{B}}TV} \lim_{t\to\infty} \frac{d}{dt} \Bigg\langle \sum_{a} \sum_{b} \left[\mathbf{R}_{\text{c},a}(t) - \mathbf{R}_{\text{c},a}(0)\right] \\ \cdot \left[\mathbf{R}_{\text{c},b}(t) - \mathbf{R}_{\text{c},b}(0)\right] \Bigg\rangle, \end{aligned} \tag{3.8}$$

$$L_{--}^{\text{self}} = \frac{N^2}{6k_{\text{B}}TV} \lim_{t\to\infty} \frac{d}{dt} \left\langle \sum_a \left[\mathbf{R}_{\text{c},a}(t) - \mathbf{R}_{\text{c},a}(0)\right]^2 \right\rangle, \tag{3.9}$$

$$\begin{aligned} L_{--}^{\text{dist}} = \frac{N^2}{6k_{\text{B}}TV} \lim_{t\to\infty} \frac{d}{dt} \Bigg\langle \sum_a \sum_{b\neq a} \left[\mathbf{R}_{\text{c},a}(t) - \mathbf{R}_{\text{c},a}(0)\right] \\ \cdot \left[\mathbf{R}_{\text{c},b}(t) - \mathbf{R}_{\text{c},b}(0)\right] \Bigg\rangle, \end{aligned} \tag{3.10}$$

where a and b are chain indices.

Eq. 3.9 is now related to the polyanion diffusivity through

$$L_{--}^{\text{self}} = \frac{D_- n_- N^2}{k_{\text{B}}TV}. \tag{3.11}$$

Since the system density $\rho = (n_+ + n_- N)/V$ is fixed, it follows that the polyanion self term scales as

$$L_{--}^{\text{self}} = D_- N \frac{\rho}{2k_{\text{B}}T}. \tag{3.12}$$

Ion Conductivity from Equilibrium MD

The ion conductivity σ can be expressed in terms of the Onsager transport coefficients:

$$\sigma = F^2 \sum_i \sum_j L_{ij} z_i z_j, \tag{3.13}$$

where F is the Faraday constant and $z_i = \pm 1$ is the ionic valency of species i [35]. For a binary PIL system, Eq. 3.13 expands to

$$\sigma = F^2(L_{++} + L_{--} - 2L_{+-}). \tag{3.14}$$

For a binary mixture, the derived relationships $L_{++} = L_{--} = -L_{+-}$ allow us to express the total ion conductivity in terms of any single Onsager coefficient. Specifically, the total conductivity is proportional to four times the magnitude of any of these equivalent coefficients.

For comparison, the Nernst–Einstein conductivity σ^{NE} for an ideal solution is

$$\sigma^{\text{NE}} = \frac{e^2}{k_{\text{B}}TV}(n_+ D_+ + n_- D_- N^2). \tag{3.15}$$

and can also be written in terms of the Onsager transport coefficients [1]:

$$\sigma^{\text{NE}} = F^2(L_{++}^{\text{self}} + L_{--}^{\text{self}}). \tag{3.16}$$

For an ideal polymer electrolyte solution in the dilute limit, σ should scale with the diffusivity of that system.

Ion Conductivity from Non-Equilibrium MD

To further validate the equilibrium MD results, we perform non-equilibrium molecular dynamics (NEMD) simulations by applying an external electric field within the linear response regime [36]. In these simulations, we extract the average drift velocity by isolating the field-induced directed motion from the underlying random diffusion. This is achieved by analyzing the MSD and subtracting the diffusive contribution, which is estimated from the MSD in the direction orthogonal to the applied field. The resulting drift velocity yields the average electrophoretic mobility, which we combine with the cation and polyanion number densities to calculate the total ion conductivity (see Appendix for details).

Unlike equilibrium MD, E-field NEMD directly measures ion conductivity by monitoring the system's response to an applied electric field, providing a clear connection between microscopic dynamics and macroscopic transport. By driving ion motion with an external force, NEMD simulations offer a stronger signal and reduced statistical noise, enabling more reliable conductivity estimates with shorter simulation times. Thus, the results obtained from NEMD serve to confirm and complement the conductivity calculated from equilibrium MD [37].

3.3 Methodology

Molecular dynamics simulations are performed in the NVT ensemble using OpenMM [34], with a DPD thermostat [38], thereby capturing hydrodynamic interactions.

Each system contains at least 48,000 identically sized charged monomer particles, with the longest chain systems containing up to 118,000 particles. The polyanion chain length N is varied from 1 to 400, while the cations remain monomeric.

The pairwise interparticle interactions are described by the soft coarse-grained GCMe potentials, with a fundamental length scale d, and energy scale $k_\mathrm{B}T$ [31]. The excluded volume interaction between two particles is given by:

$$u_{\mathrm{excl}}(r) = A\left(\frac{3}{2\pi\sigma_s^2}\right)^{3/2}\exp\left(-\frac{3}{2\sigma_s^2}r^2\right), \tag{3.17}$$

where r is the separation distance, $A \approx 25.2d^3k_\mathrm{B}T$ is the excluded volume repulsion parameter, and $\sigma_\mathrm{s} \approx 0.257d$ is the mass smearing radius.

The smeared electrostatic interaction between two particles is expressed as:

$$u_{\mathrm{elec}}(r) = \left(\frac{z_i z_j e^2}{4\pi\varepsilon_0\varepsilon_r r}\right)\mathrm{erf}\left(\sqrt{\frac{\pi}{2}}\frac{r}{a}\right), \tag{3.18}$$

where $a = d/2$ is the electrostatic mass smearing radius, z is the valency, and ε_0 is the vacuum permittivity.

The electrostatic strength in the system is characterized by the Bjerrum length

$$l_{\mathrm{B}} = \frac{e^2}{4\pi\varepsilon_0\varepsilon_{\mathrm{r}}k_{\mathrm{B}}T}. \tag{3.19}$$

We choose a relative permittivity of $\epsilon_{\mathrm{r}} = 12$, consistent with typical values for ionic liquids [39, 40]. With this choice of ϵ_{r}, $\lambda_B \approx 4.34d$ for our charged systems, indicating substantial electrostatic interactions.

From this, the corresponding Debye screening length

$$\lambda_D = \frac{1}{\sqrt{8\pi l_{\mathrm{B}}\rho}} \tag{3.20}$$

is approximately $0.087d$. For comparison, we also simulate an uncharged system under identical conditions by removing all charges, equivalent to setting the Bjerrum length to zero.

To capture chain connectivity, a harmonic bond potential is used:

$$u_{harm}(r) = \frac{1}{2}k(r-b)^2, \tag{3.21}$$

where $k = 100k_{\mathrm{B}}T/d^2$ is the spring constant and $b = 0.8d$ is the equilibrium bond length.

The systems are solvent-free and contain an equal number of polyanion and cation beads, with the same mass m, at a total number density of $\rho = 2.5d^{-3}$. In this study, the cation and polymer beads were assigned the same size, in order to minimize the number of free parameters and focus on the effect of chain length and electrostatics [1]. The simulations are initialized by first determining the cubic box dimensions and volume to accommodate the system, constrained by the system density and total number of particles. All system dimensions are set equal, and periodic boundary conditions are used in all directions. For example, a 48,000-particle system is simulated within a cubic domain of equidimensional length of approximately $26.95d$. Simulation cells were initialized by randomly placing cation beads and the starting positions of polyanion chains. Each polyanion was then constructed bead-by-bead via a random-walk procedure, with adjacent monomers constrained to one bond length apart. A local energy minimization is first performed to remove unfavorable interactions. The dynamics are then simulated over a time scale sufficient for the

trajectories to reach the diffusive regime, using an integration time step of $t = 0.04\,\tau$, where $\tau = d(m/\epsilon)^{1/2}$ is the fundamental simulation time unit, with the energy ϵ set to be $k_{\mathrm{B}}T$. To map to real units, we choose the length scale as $d \approx 1.07$ nm, the particle mass as $m \approx 72.1$ g/mol (approximately four times that of water) and the temperature to be approximately 300 K.

3.4 Results and Discussion

Chain Dynamics

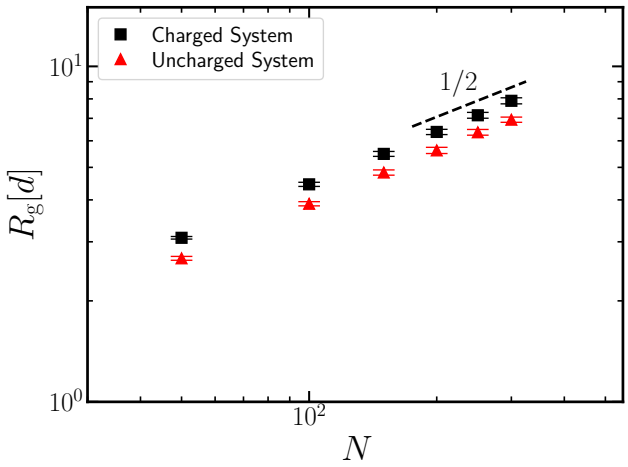

Figure 3.1: Radius of gyration, R_{g}, for polyanion and neutral polymers as a function of chain length, N.

We begin by investigating the effect of charge on polymer structure and dynamics. With the polymer volume fraction held constant at 50%, we expect both excluded volume and hydrodynamic interactions to be significantly screened. For an analogous neutral system under these conditions, we anticipate Rouse dynamics for short to moderate chains and reptation for longer chains. It is therefore important to assess how the introduction of charge modifies this expected behavior. Accordingly, we first examine the chain length dependence of structural and dynamical properties and evaluate the extent to which the Rouse and reptation model apply to these charged systems.

To analyze the ion correlation effect on polymer structure, we first explore the chain length dependence of the radius of gyration in charged and uncharged systems. The radius of gyration, R_{g}, is given by [19]:

$$R_{\mathrm{g}} = \sqrt{\frac{1}{N}\sum_{i=1}^{N}\left\langle(\mathbf{r}_i - \mathbf{R}_{\mathrm{c}})^2\right\rangle}. \tag{3.22}$$

As shown in Fig. 3.1, both the charged and uncharged systems follow $R_g \sim N^{1/2}$ scaling, characteristic of ideal chain dynamics. Charged chains are slightly larger, reflecting effects of residual electrostatic repulsions, even in the high-density regime where the nominal Debye length λ_D is smaller than the particle radius. In spite of the slightly larger R_g for the charged systems, the scaling behavior remains unchanged.

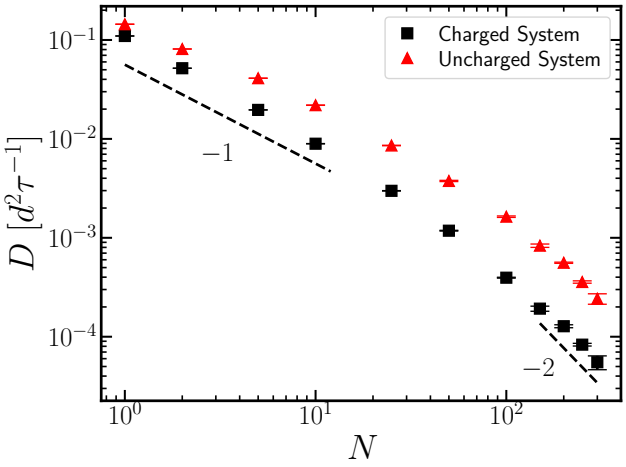

(a)

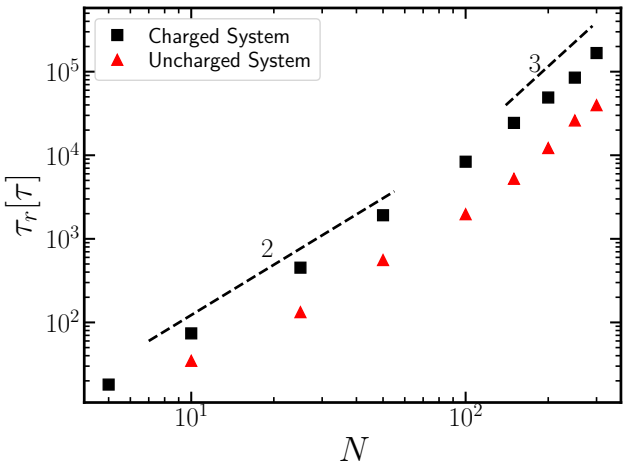

(b)

Figure 3.2: (a) Polymer center-of-mass diffusion, D, as a function of chain length, N. (b) End-to-end vector relaxation time, τ_r, as a function of chain length, N.

Next, we quantify the effect of chain length and electrostatic correlations on the polymer dynamics, and compare our results with the Rouse and reptation models for neutral systems. The diffusion coefficients for both individual ionic species and the polyionic chains are determined from their respective mean squared displacements (MSD):

$$D = \frac{1}{6} \lim_{t\to\infty} \frac{d}{dt} \left\langle \frac{1}{n} \sum_{a}^{n} \left[\mathbf{R}_{\mathrm{c},a}(t) - \mathbf{R}_{\mathrm{c},a}(0) \right]^2 \right\rangle. \tag{3.23}$$

Figure 3.2a shows that both charged and uncharged systems follow $D \sim N^{-1}$ scaling in the unentangled regime and transition to $D \sim N^{-2}$ in the entangled regime. We note that for the unentangled charged case, the scaling is slightly weaker ($D \sim N^{-0.9}$), consistent with the behavior of L_{--} in Fig. 3.5. Thus, apart from this modest shift and lower overall diffusivity, the qualitative scaling remains essentially the same as in the uncharged systems.

In addition to the polymer diffusion, we examine how the relaxation time varies with chain length, which is obtained by integrating the end-to-end vector autocorrelation function (see Appendix):

$$C_{\mathrm{ee}}(t) = \frac{\langle \mathbf{R}_{\mathrm{ee}}(t) \cdot \mathbf{R}_{\mathrm{ee}}(0) \rangle}{\langle \mathbf{R}_{\mathrm{ee}}^2 \rangle}. \tag{3.24}$$

As shown in Fig. 3.2b, both the charged and uncharged systems transition from a Rouse regime to an entangled regime, with $\tau_r \sim N^2$ and $\tau_r \sim N^3$ respectively. The slower relaxation in the charged system is attributed to the additional interparticle friction imposed by electrostatic interactions. Using the relation $\tau_r \sim R_{\mathrm{g}}^2/D$ to combine the scalings of diffusivity and radius of gyration yields $\tau_r \sim N^2$ in the unentangled regime and $\tau_r \sim N^3$ in the entangled regime. This expected agreement shows that both charged and uncharged chains follow ideal scaling behavior, with electrostatics affecting only the absolute magnitudes of the dynamical properties.

While these results indicate that electrostatic interactions do not qualitatively alter the polymer dynamics, we corroborate this conclusion by performing a Rouse mode analysis of the internal chain segments. More details on the Rouse mode calculation are provided in the Appendix. In Fig. 3.3a we present the scaled amplitudes $\langle X_p^2 \rangle \sin^2(p\pi/(2N))$ of the Rouse modes, plotted as a function of N/p. With increasing N/p, the scaled amplitudes become asymptotically independent of p, consistent with the Rouse prediction $\langle X_p^2 \rangle \sin^2(p\pi/(2N)) = b^2/4$. Deviations at small length scales are expected from previous studies [25, 41]. For the charged system, we also observe a larger effective Kuhn length, in agreement with the increase in R_{g} in Fig. 3.1. Lastly, in Fig. 3.3b, we plot the Rouse-modes relaxation times τ_p as a function of N/p, for a wide range of chain lengths. We find that the data for all chain lengths fall on a master curve with a $\tau_p \sim (N/p)^2$ scaling. Overall, the

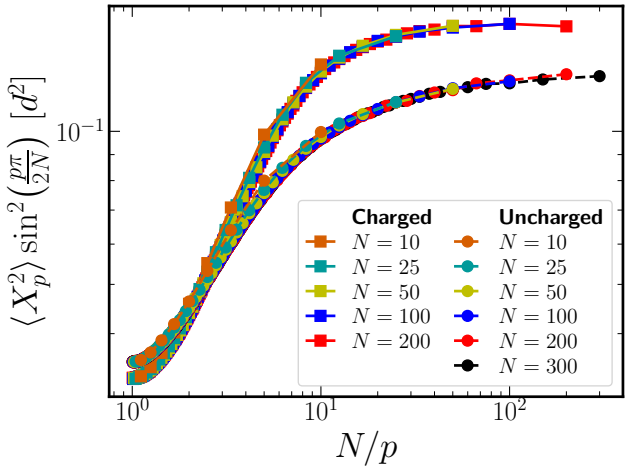

(a)

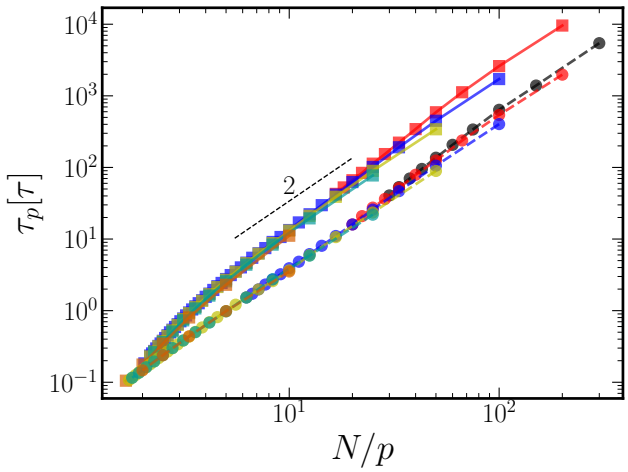

(b)

Figure 3.3: (a) Scaled amplitudes of the Rouse modes for both charged and uncharged systems across various chain lengths. (b) Effective relaxation time, τ_p, of the p-th mode for charged and uncharged systems across different chain lengths.

polymer dynamics are broadly consistent with Rouse behavior at unentangled chain lengths [42], though subtle deviations emerge, particularly at high mode numbers.

Thus, the charged system exhibits Gaussian chain scaling with clear Rouse and reptation regimes. Electrostatic correlations introduce only secondary quantitative shifts in chain dimensions and dynamics, leaving the qualitative scaling behavior unchanged from the uncharged analogue.

Onsager Transport Coefficient

To understand the chain length dependent dynamics, we deconstruct the Onsager transport coefficients, L_{ij}, into components for single-ion diffusion and collec-

tive ion correlations. While polyanion diffusion slows predictably with increasing chain length, the collective ion correlations are governed by a competition between correlated motion arising from increasing chain length and repulsive interchain electrostatics.

Compared to dilute or semi-dilute polyelectrolyte solutions, solvent-free PILs exhibit significantly stronger steric hindrance and highly screened, short-range electrostatic interactions. These more localized electrostatic interactions, coupled with the system's incompressibility, produce a complex set of transport behaviors that deviate from more dilute or idealized frameworks.

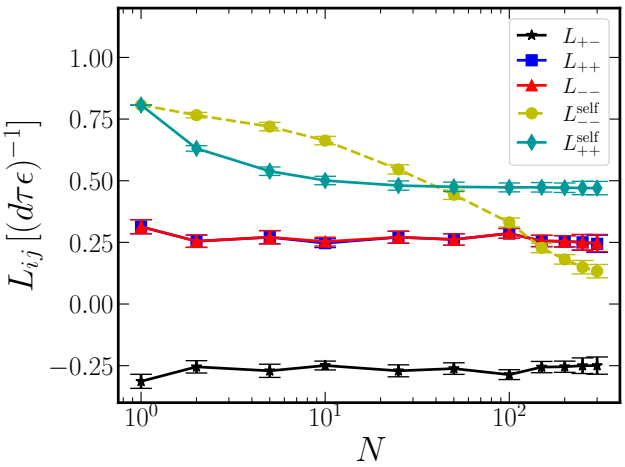

Figure 3.4: Onsager transport coefficients, L_{ij}, for the charged polyanion system as a function of chain length N. Note that L_{++} and L_{--} directly overlap, a result of the equal mass for polyanion monomers and cations, which enforces $L_{--} = L_{++} = -L_{+-}$.

Beginning with Fig. 3.4 and the L_{++}^{self} term, we observe an initial decrease with chain length, followed by a plateau around $N \sim 25$, indicating that counterion motion becomes effectively independent of chain length beyond this point. Accounting for the N dependence in Eq. 3.12 and the short chain diffusivity scaling relationship of $\sim N^{-1}$, it becomes clear that we should expect almost no change to L_{--}^{self} in the short chain regime ($N < 10$). This is consistent with our earlier observation of slight deviation from Rouse dynamics for the charged unentangled regime. From Eq. 3.12 and our previous diffusivity analysis, as the chains enter the entanglement regime where the diffusivity scales as $\sim N^{-2}$, we should expect L_{--}^{self} to begin to scale as $\sim N^{-1}$, and indeed the relationship in the fully entangled regime is $\sim N^{-1.05}$.

For the non-self terms, when we exclude the monomer instance, we find a marked plateau in all three Onsager coefficients. Evaluating just the polyanion term L_{--} in

the very short chain regime ($N < 25$), the self component L_{--}^{self} exceeds the total L_{--}. This necessarily implies that the distinct contribution is negative, which is evident in Fig. 3.5a and driven by anticorrelated interchain interactions. Figure 3.5a further illustrates that as chain length increases and polyanions become increasingly entangled, the distinct contribution L_{--}^{dist} transitions towards positive values, indicating increasingly correlated interchain motion.

The ultimate effect of this competition between these interactions is that L_{--} is nearly constant once $N > 10$, decreasing only once the chains become fully entangled. For direct comparison, we also include the analogous uncharged system—corresponding to the limit of $\lambda_B \to 0$ —in Fig. 3.5, where the Onsager coefficients exhibit the same overall trend.

Notably, in Fig. 3.5 the difference in magnitude between the charged (top panel) and uncharged (bottom panel) systems indicates that the electrostatics dampen polymer correlated motion. However, the near identical magnitudes of the distinct terms imply that interchain anticorrelation is not a result of electrostatics but rather incompressibility. Additionally, the uncharged system shows a more clearly defined transition into the entangled regime around $N = 100$, transitioning from $\sim N^0$ to $\sim N^{-1}$. This is the expected relationship for both the charged and uncharged polymers where Eq. 3.12 would necessitate a D_N dependence for L_{--}^{self}

As shown in Fig. 3.4, $L_{++} < L_{++}^{\text{self}}$ for all chain lengths; from Eq. 3.4, this requires a negative distinct term, indicating anticorrelated counterion–counterion motion. Since L_{++} is nearly constant and the L_{++}^{self} decreases and then plateaus with N, the degree of anticorrelated motion decreases with N. We note that in the barycentric frame of a solvent-free binary ionic system, momentum conservation dictates a negative cross distinct term L_{+-}^{dist} [43]. However, the same-charge distinct terms are not individually constrained to negative values. As seen in Fig. 3.5a, L_{--}^{dist} transitions from negative to positive at larger chain lengths, while L_{++}^{dist} remains negative.

Conductivity

Ion conductivity is crucial for optimizing next-generation energy conversion and storage devices. Excluding the monomeric case, the conductivity behavior in Fig. 6 aligns closely with previous molecular dynamics studies in the short-chain regime [1]. Specifically, conductivity appears independent of chain length in the unentangled regime from both equilibrium and non-equilibrium MD. In the fully entangled regime, we see a slight decline, mirroring the drop in diffusive motion from the L_{--}^{self}

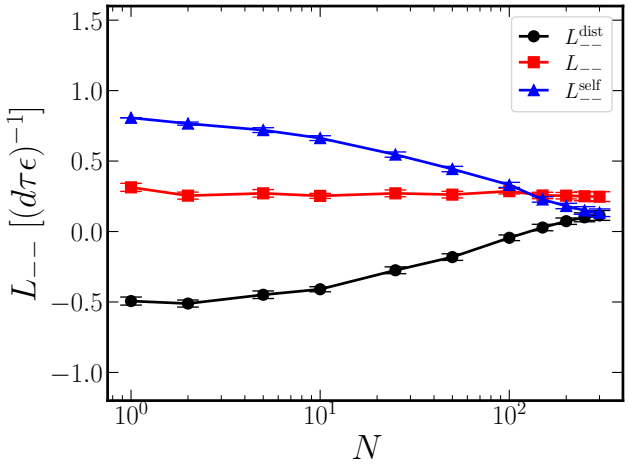

(a)

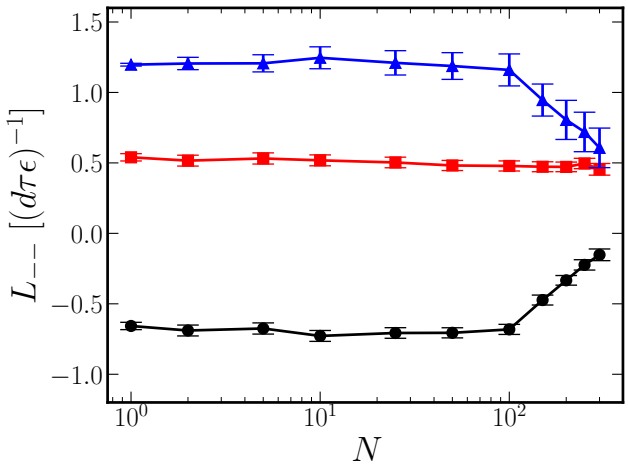

(b)

Figure 3.5: Rouse to reptation dynamics of L_{--} for (a) charged and (b) uncharged systems, plotted against chain length, N. For two-component systems L_{--} is sufficient to calculate the ion conductivity.

Onsager coefficient — despite the increase in interchain correlations (Fig. 3.5).

These results are non-obvious when viewed through the traditional Nernst–Einstein framework for an ideal solution. From Eq. 3.16 and Fig. 3.4, we would expect the Nernst–Einstein conductivity to decrease in concert with the self-diffusion terms. In the limit of long chain length, where L_{--}^{self} approaches 0, the Nernst–Einstein conductivity reduces to $\sigma^{\mathrm{NE}} = F^2 L_{++}^{\mathrm{self}}$ and asymptotically approaches ~ 0.51, consistent with the behavior of the L_{++}^{self} term shown in Fig. 3.4. Initially, this decline in conductivity is primarily driven by the cation diffusivity D_+ in the short-chain and Rouse regimes. As the polymer enters the transition and reptation regimes, where D_+ becomes chain length independent, the N-dependent polyanion diffusivity D_-

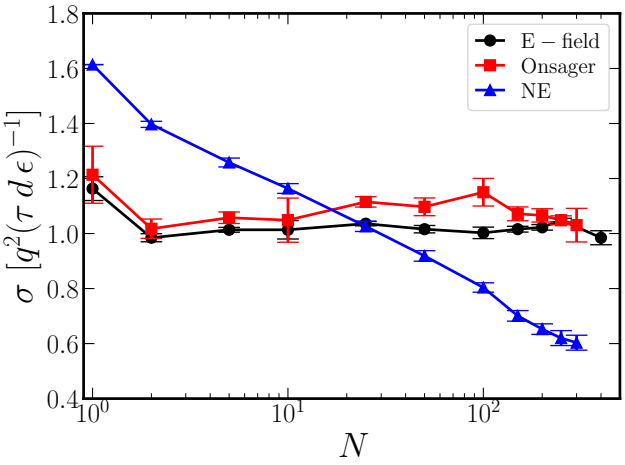

Figure 3.6: Ion conductivity, σ, as a function of chain length N, from both the equilibrium and the non-equilibrium simulations compared to the Nernst–Einstein conductivity prediction.

becomes the dominant factor driving the further reduction in the Nernst–Einstein conductivity.

It is important to note that while the Nernst–Einstein conductivity typically serves as an upper limit and decreases with chain length, the true conductivity remains relatively constant and can even exceed this value, as shown in Fig. 3.6. This occurs because the short-range Debye screening suppresses the usual correlated motion between counterions that would otherwise decrease conductivity, while chain entanglement produces beneficial polyanion correlation.

3.5 Conclusions

In summary, we conducted coarse-grained molecular dynamics simulations with smeared mass and charge distributions to investigate the effect of chain length and electrostatic correlations on the ion transport properties of PILs in the solvent-free limit. By comparing charged and uncharged systems under identical conditions, we isolated the effects of electrostatic correlations and chain connectivity, avoiding confounding contributions from glass transition or temperature-dependent electrostatics that often complicate interpretation of experimental results.

We find that introducing charge to the polymer units does not change the qualitative behavior of the structural and dynamical properties. The radius of gyration follows ideal chain scaling, $R_g \sim N^{1/2}$, while diffusivities and relaxation times follow Rouse and reptation scaling across unentangled and entangled regimes. Charge primarily induces quantitative changes: polymer chains become stiffer, relaxation slows, and

the diffusivity decreases.

Despite the sharp reduction in polyanion diffusivity (or L_{--}^{self}) with increasing N, the total ion conductivity remains remarkably constant, aside from an initial drop from IL to PIL. We attribute this invariance to an increase in the interchain correlations that compensate for the slowed chain mobility. The persistence of this effect even in uncharged systems indicates that incompressibility, rather than electrostatic interactions, dominates correlated motion, revealing an intrinsic decoupling of charge transport from chain relaxation that does not rely on kinetic trapping or vitrification.

Several directions for future study emerge from this work. First, our model neglects solvent and assumes uniform charge distribution; introducing solvent or counterion asymmetry would allow exploration of experimentally relevant systems. Including solvent adds an extra degree of freedom to the system and modifies the coupling between L_{ij}, likely reducing interchain correlations and weakening the compensation effect. Second, our results imply that increasing chain length increases the viscosity of the system without significantly affecting ion conductivity, enabling independent tuning of mechanical and transport properties—a feature uncommon in conventional ionic liquids. Finally, linking microscopic polymer center-of-mass diffusion and interchain transport to macroscopic observables such as transference number and ion conductivity can guide the design of PILs or their solutions with optimized charge transport.

In conclusion, our results highlight the dominant role of incompressibility in modulating polymer dynamics and ion transport, with electrostatic correlations playing only a surprisingly secondary role. By disentangling these effects from glass transition, we establish a mechanistic basis for interpreting conductivity behavior and identify key physical parameters that govern performance in solvent-free ionic materials.

3.6 Appendix

Mean Squared Displacement

The mean squared displacement (MSD) was computed for a range of polymer chain lengths by averaging the trajectories of particles within each species (cation and polyanion). The analysis was conducted on a per-monomer basis, considering every monomer and counterion in the system. In contrast as disccussed later in this document, the diffusivity of the polyanion was calculated using only the central monomers. Figure 3.7 shows the resulting MSD profiles, with reference slope lines

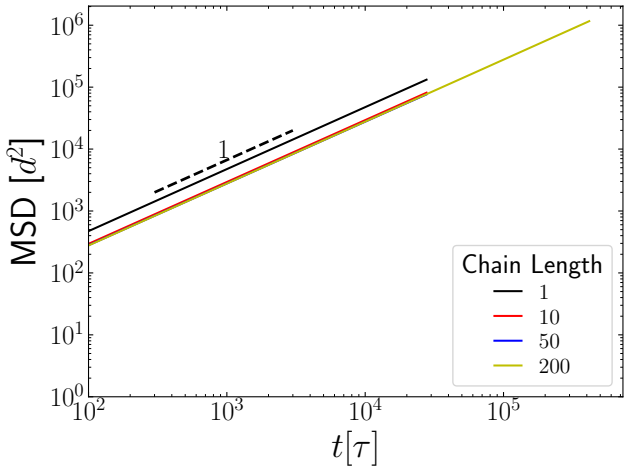

(a)

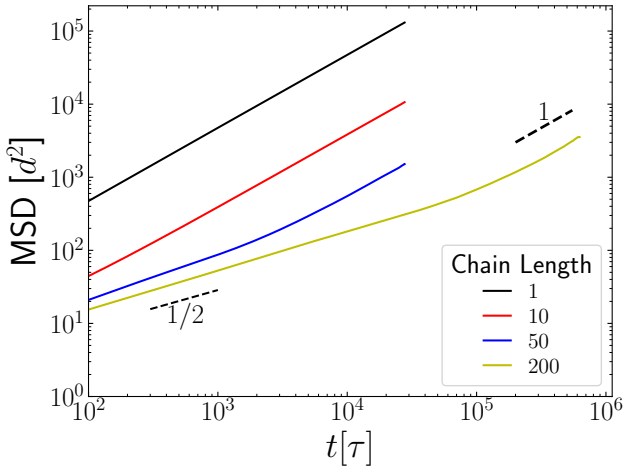

(b)

Figure 3.7: Mean squared displacement (MSD) of (a) the cation and (b) the polyanion center-of-mass, for selected polyanion chain lengths.

indicating the different diffusive regimes. Linear fits were performed on the portions of the curves that had reached the terminal diffusive regime, where the MSD scales linearly with time.

Cross Mean Squared Displacement

Onsager transport coefficients (L_{ij}) are determined from the slopes of the cross mean squared displacement (CMSD), which is defined as

$$\text{CMSD} = \left\langle \sum_{\alpha} \sum_{\beta} \left[\mathbf{r}_{i,\alpha}(t) - \mathbf{r}_{i,\alpha}(0)\right] \cdot \left[\mathbf{r}_{i,\beta}(t) - \mathbf{r}_{i,\beta}(0)\right] \right\rangle \tag{3.25}$$

The CMSD is analogous to the conventional MSD but is computed for each unique

i, j pair [27]. This approach is consistent with the integral form of the Green–Kubo relations discussed in the main text. Linear fitting is performed on the long-time regime of these CMSD profiles, where the polyanion dynamics reach the diffusive limit. Additionally, because the L_{+-} term is necessarily negative this system, the absolute value of the CMSD term is used when plotting in log–log space. Examples of CMSD time traces and their linear fits in the diffusive regime are shown in Fig. 3.8.

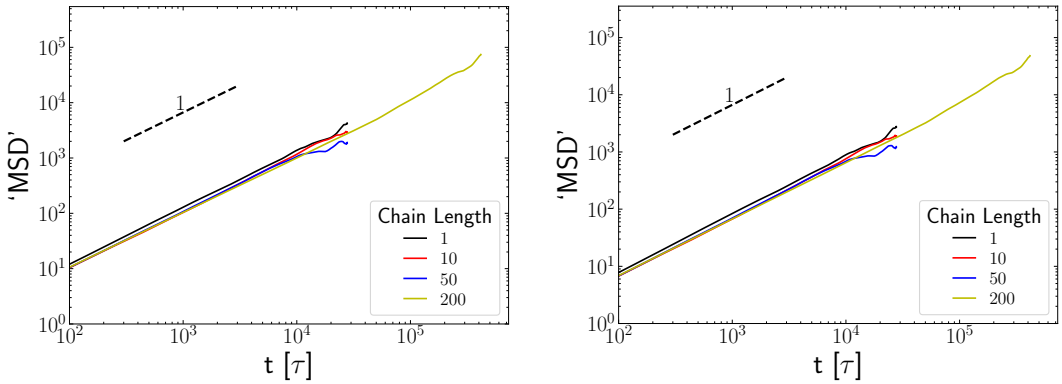

(a) L_{++} **(b)** $|L_{+-}|$

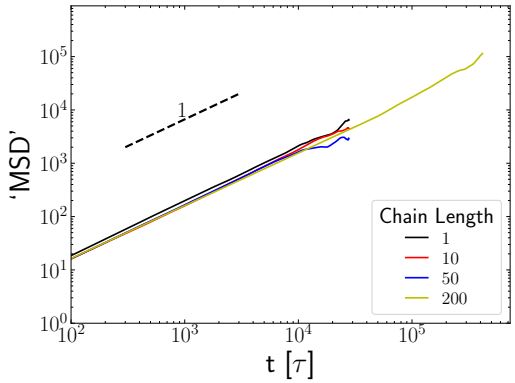

(c) L_{--}

Figure 3.8: Cross mean squared displacement used to determine L_{++}, $|L_{+-}|$, and L_{--}.

Rouse Modes

This section details the computational methodology employed to characterize the internal dynamics of polymer chains through normal mode analysis [42]. Simulation snapshots from the equilibrium molecular dynamics trajectories (as described in the main article) were taken to analyze the internal dynamics of polymer chains. For each snapshot, the instantaneous position of each particle $\mathbf{r}_n(t)$ (where n is the

particle index from 0 to $N-1$ and t is time) was transformed into normal mode amplitudes $\mathbf{X}_p(t)$ using a discrete cosine transformation:

$$\mathbf{X}_p(t) = \sum_{n=0}^{N-1} \mathbf{r}_n(t) \cos\left(\frac{\pi p(n+1/2)}{N}\right), \tag{3.26}$$

where p represents the mode index, ranging from 1 to $N-1$. This transformation was applied independently to each polymer chain within the simulation, generating a time series of mode amplitudes for every mode p of each chain.

The time autocorrelation function (ACF) for each normal mode p, denoted $\phi_p(t)$, was computed from its three-dimensional vector amplitude time series $X_p(t)$. For computational efficiency, a fast Fourier transform (FFT)-based correlation algorithm was utilized. The autocorrelations of the x-, y-, and z-components of $X_p(t)$ were evaluated separately and then summed to obtain the total ACF. Each chain's ACF was normalized by its initial value at $t = 0$. To improve statistical accuracy and reduce noise, the final ACF for a given mode p was acquired by averaging the normalized ACFs across all individual chains present in the simulation:

$$\phi_p(t) = \frac{\langle \mathbf{X}_p(t') \cdot \mathbf{X}_p(t'+t) \rangle_{t',\text{chains}}}{\langle \mathbf{X}_p(t') \cdot \mathbf{X}_p(t') \rangle_{t',\text{chains}}}. \tag{3.27}$$

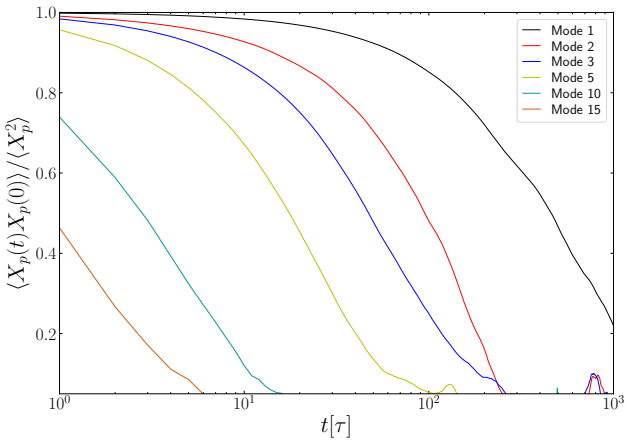

Figure 3.9: Example Rouse mode autocorrelation function for $N = 100$.

The averaged normal mode ACFs $\phi_p(t)$ were subsequently fitted to the Kohlrausch–Williams–Watts (KWW) stretched exponential function:

$$\phi_p(t) = \exp\left[-\left(\frac{t}{\tau_p^*}\right)^{\beta_p}\right]. \tag{3.28}$$

Nonlinear least-squares fitting was used to extract the characteristic relaxation times τ_p^* and the stretching exponents β_p ($0 < \beta_p \leq 1$). Initial estimates for τ_p^* were derived from the ACF's half-decay time; a default value was used if this point was not reached. The mean relaxation times τ_p, representing the areas under the KWW decay curves, were then calculated from the fitted parameters using:

$$\tau_p = \frac{\tau_p^*}{\beta_p} \Gamma\left(\frac{1}{\beta_p}\right), \tag{3.29}$$

where Γ denotes the Gamma function.

KWW fit reliability was ensured by including only ACF data points where $\phi_p(t) > 0.003$. Coarser temporal sampling (e.g., in longer chain trajectories) often precluded reliable fitting of faster-decaying, higher-order modes due to their ACFs rapidly falling below this threshold.

Relaxation Times

The polymer end-to-end vector autocorrelation functions $C_{\mathrm{ee}}(t)$ were computed from simulation trajectories as described in the main text, and then integrated numerically using Simpson's rule to get the characteristic relaxation times τ_{r} using

$$\tau_r = \int_0^\infty C_{\mathrm{ee}}(t)\, dt. \tag{3.30}$$

Fig. 3.10 shows representative $C_{\mathrm{ee}}(t)$ curves for various chain lengths on a log–linear scale.

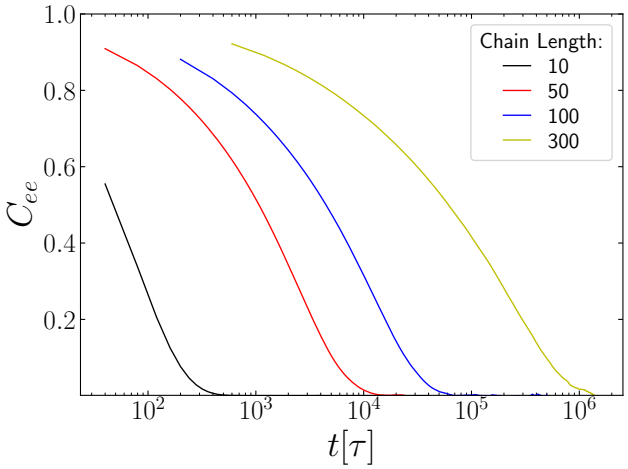

Figure 3.10: Representative end-to-end vector autocorrelation functions $C_{\mathrm{ee}}(t)$ for different polymer chain lengths.

Chain Center-of-Mass Diffusion

The diffusion coefficients reported in the main text were computed using the average positions of monomers within the middle 20% of each polymer chain to enhance statistical reliability for longer chains. To verify that this approach does accurately approximates the results obtained using the true chain centers of mass, self-diffusion coefficients from both the central-beads estimate and the full center-of-mass calculation are compared in Fig. 3.11.

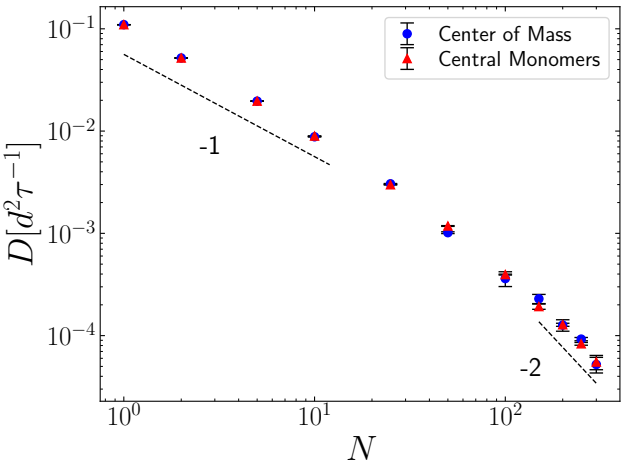

Figure 3.11: Comparison of the polyanion self-diffusion coefficients calculated from the polymer chains' centers of mass and from averaging the displacements of monomers within the middle 20% of each chain. The close agreement between the two approaches validates the use of the localized particle displacement method for characterizing system-wide diffusion.

Cation Diffusion

Fig. 3.12 shows the cation diffusivity for both charged and uncharged systems (defined in the main text). It highlights the increased interparticle friction from the more pronounced electrostatic interactions in the charged system with larger Bjerrum lengths. Notably the behavior for both systems follows the same plateau behavior at around the same chain length. This parallel trend indicates that the reduced cation mobility is a result of this increased friction, not a fundamentally different phenomenon.

Electric Field Analysis

This work follows the procedure outlined in Shen et al. [36] to determine ion conductivity from drift velocity and electrophoretic mobility. The drift velocity v_z can be extracted from the additional displacement induced by the applied electric

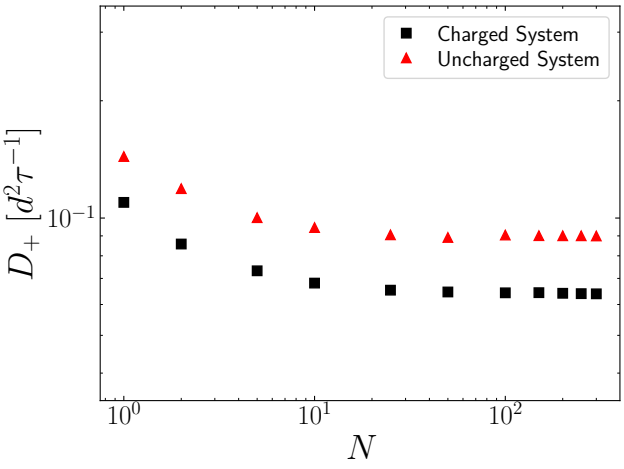

Figure 3.12: Comparison of the cation self-diffusion coefficients in the charged and uncharged systems, illustrating the increased interparticle friction in the charged system caused by the much stronger electrostatic interactions. Note, N here refers to the corresponding polyanion chain length.

field relative to an equilibrated system. Alternatively, v_z can be directly calculated from the displacement component parallel to the electric field compared to the orthogonal displacement. For an electric field applied in the z-direction, the squared average drift velocity is related to the MSD by:

$$\begin{aligned}\langle v_z\rangle^2 t^2 &= \left\langle \left(\mathbf{r}_z(t) - \mathbf{r}_z(0)\right)^2 \right\rangle_E - \left\langle \left(\mathbf{r}_z(t) - \mathbf{r}_z(0)\right)^2 \right\rangle_0 \\ &= \left\langle \left(\mathbf{r}_\parallel(t) - \mathbf{r}_\parallel(0)\right)^2 \right\rangle_E - \left\langle \left(\mathbf{r}_\perp(t) - \mathbf{r}_\perp(0)\right)^2 \right\rangle_E .\end{aligned} \tag{3.31}$$

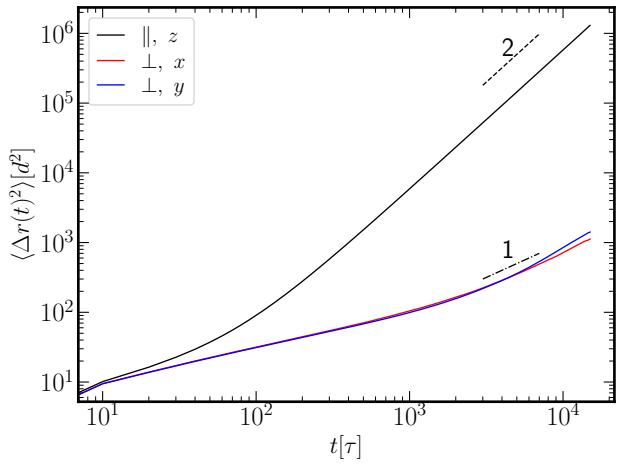

Figure 3.13: Directional MSD of the polyanion system with $N = 300$ under an electric field, illustrating the parallel and orthogonal components used to determine the drift velocity for PIL systems with longer relaxation times.

The average drift velocity $\langle v_z \rangle$ is obtained by fitting the function $a + bt^2$ to the log–log plot of the MSD after subtracting the orthogonal displacement contribution. At sufficiently long times, the parallel MSD exhibits a slope of 2 while the orthogonal MSD shows a slope of 1. Consequently, the fitted coefficient yields $\langle v_z \rangle = \sqrt{b}$. An example of this fitting procedure is shown in Fig. 3.13.

The average electrophoretic mobility μ is then calculated from the drift velocity as

$$\mu = \frac{\langle v_z \rangle}{E}. \tag{3.32}$$

In practice, μ is determined from the linear response of $\langle v_z \rangle$ across a range of applied electric fields (e.g., 0–0.2 in reduced units). The slope of the $\langle v_z \rangle$ versus E plot yields the average mobility. An example is shown in Fig. 3.14.

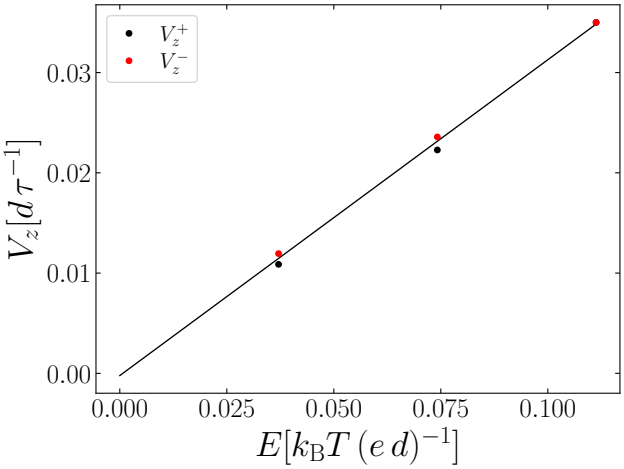

Figure 3.14: Linear drift response of the polyanion system with $N = 300$, showing the average drift velocity $\langle v_z \rangle$ as a function of applied electric field E.

Finally, the ion conductivity σ is calculated using the mobilities and number densities of the positive and negative ions:

$$\sigma = \mu_+ \rho_+ e + \mu_- \rho_- e. \tag{3.33}$$

The resulting ion conductivity values are presented in the main text.

To ensure that the application of the electric field in the z direction does not affect the uniform density distribution of the particles, we computed the linear number density of cations along the principal axes (x, y, z). A bootstrap resampling method was employed on the particle coordinates to calculate the mean density and its corresponding standard error for the two key frames. These were the end of the equilibration run before applying an electric field (t_0), and the final time step of

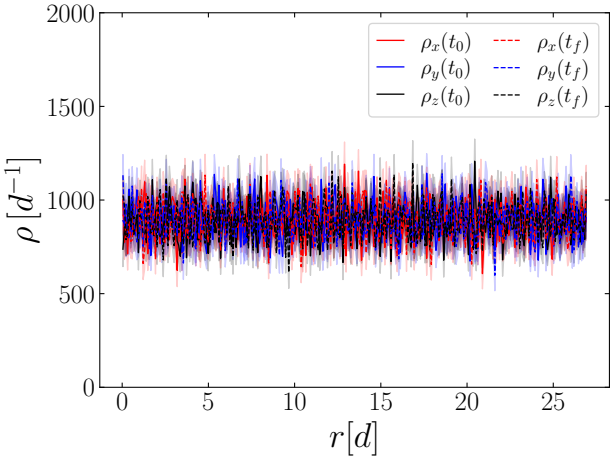

Figure 3.15: Linear number density, ρ, of cations shown along the x (red), y (blue), and z (black) axes for the equilibrated system prior to applying an electric field (t_0, solid lines) and at the final time step with the applied field (t_f, dashed lines) for chain length N=50 and electric field strength E≈ 0.075. The overlapping profiles and error bands (shaded regions) confirm the system remains spatially isotropic under the applied field.

the production simulation with the applied field (t). The resulting density profiles for each direction are statistically indistinguishable, as shown in Fig. 3.15 for the system with chain length N=50 and electric field strength E≈0.075 (in reduced units). This overlap confirms that the system is spatially isotropic and that this property is maintained even under the influence of the electric field.

References

[1] Fong, K. D.; Self, J.; McCloskey, B. D.; Persson, K. A. *Macromolecules* **2021**, *54*, 2575–2591, DOI: 10.1021/acs.macromol.0c02545.

[2] Ganesan, V. *Molecular Systems Design & Engineering* **2019**, *4*, 280–293, DOI: 10.1039/c8me00114f.

[3] Hickner, M. A. *Materials Today* **2010**, *13*, 34–41, DOI: 10.1016/s1369-7021(10)70082-1.

[4] Kusoglu, A.; Weber, A. Z. *Chemical Reviews* **2017**, *117*, 987–1104, DOI: 10.1021/acs.chemrev.6b00159.

[5] Correia, D. M.; Fernandes, L. C.; Martins, P. M.; García-Astrain, C.; Costa, C. M.; Reguera, J.; Lanceros-Méndez, S. *Advanced Functional Materials* **2020**, *30*, DOI: 10.1002/adfm.201909736.

[6] Flouda, P.; Bukharina, D.; Pierce, K. J.; Stryutsky, A. V.; Shevchenko, V. V.; Tsukruk, V. V. *ACS Applied Materials & Interfaces* **2022**, *14*, 27028–27039, DOI: 10.1021/acsami.2c04502.

[7] Özenler, S.; Kiriy, N.; Muza, U. L.; Geisler, M.; Kiriy, A.; Voit, B. *Designed Monomers and Polymers* **2025**, *28*, 35–47, DOI: 10.1080/15685551.2024.2449444.

[8] Stacy, E. W.; Gainaru, C. P.; Gobet, M.; Wojnarowska, Z.; Bocharova, V.; Greenbaum, S. G.; Sokolov, A. P. *Macromolecules* **2018**, *51*, 8637–8645, DOI: 10.1021/acs.macromol.8b01221.

[9] Tsamopoulos, A. J.; Wang, Z.-G. *ACS Macro Letters* **2024**, *13*, 322–327, DOI: 10.1021/acsmacrolett.3c00757.

[10] Yue, L.; Ma, J.; Zhang, J.; Zhao, J.; Dong, S.; Liu, Z.; Cui, G.; Chen, L. *Energy Storage Materials* **2016**, *5*, 139–164, DOI: 10.1016/j.ensm.2016.07.003.

[11] Arora, S.; Verma, N. *RSC Applied Polymers* **2024**, *2*, 317–355, DOI: 10.1039/d3lp00269a.

[12] Bocharova, V.; Wojnarowska, Z.; Cao, P.-F.; Fu, Y.; Kumar, R.; Li, B.; Novikov, V. N.; Zhao, S.; Kisliuk, A.; Saito, T.; Mays, J. W.; Sumpter, B.; Sokolov, A. P. *The Journal of Physical Chemistry B* **2017**, *121*, 11511–11519, DOI: 10.1021/acs.jpcb.7b09423.

[13] Yang, F.; Zhao, M.; Smith, D.; Cebe, P.; Lucisano, S.; Allston, T.; Smith, T. W. *Polymers* **2022**, *14*, 254, DOI: 10.3390/polym14020254.

[14] Amer, M. M.; Shouman, M. A.; Salem, M. S.; Kannan, A. M.; Hamed, A. M. *Thermal Science and Engineering Progress* **2024**, *53*, 102714, DOI: 10.1016/j.tsep.2024.102714.

[15] Lebedeva, O.; Kultin, D.; Kustov, L. *European Polymer Journal* **2024**, *203*, 112657, DOI: 10.1016/j.eurpolymj.2023.112657.

[16] Qian, W.; Texter, J.; Yan, F. *Chemical Society Reviews* **2017**, *46*, 1124–1159, DOI: 10.1039/c6cs00620e.

[17] Imbrogno, J.; Maruyama, K.; Rivers, F.; Baltzegar, J. R.; Zhang, Z.; Meyer, P. W.; Ganesan, V.; Aoshima, S.; Lynd, N. A. *ACS Macro Letters* **2021**, *10*, 1002–1007, DOI: 10.1021/acsmacrolett.1c00305.

[18] Matsumoto, K.; Yano, T.; Date, S.; Odahara, Y.; Narimura, S. *Polymer Bulletin* **2021**, *78*, 5165–5180, DOI: 10.1007/s00289-020-03364-4.

[19] Rubinstein, M.; Colby, R. H., *Polymer Physics*; Oxford University PressOxford: 2003, DOI: 10.1093/oso/9780198520597.001.0001.

[20] Reiter, M.; Anton, A. M.; Chang, J.; Kremer, F.; Unterlass, M. M.; Yuan, J. *Journal of Polymer Science* **2021**, *59*, 1518–1527, DOI: 10.1002/pol.20210200.

[21] Jeddi, J.; Niskanen, J.; Lessard, B. H.; Sangoro, J. *Faraday Discussions* **2024**, *253*, 426–440, DOI: 10.1039/d4fd00070f.

[22] Wojnarowska, Z.; Feng, H.; Fu, Y.; Cheng, S.; Carroll, B.; Kumar, R.; Novikov, V. N.; Kisliuk, A. M.; Saito, T.; Kang, N.-G.; Mays, J. W.; Sokolov, A. P.; Bocharova, V. *Macromolecules* **2017**, *50*, 6710–6721, DOI: 10.1021/acs.macromol.7b01217.

[23] Fan, F.; Wang, W.; Holt, A. P.; Feng, H.; Uhrig, D.; Lu, X.; Hong, T.; Wang, Y.; Kang, N.-G.; Mays, J.; Sokolov, A. P. *Macromolecules* **2016**, *49*, 4557–4570, DOI: 10.1021/acs.macromol.6b00714.

[24] Zhang, Z.; Wheatle, B. K.; Krajniak, J.; Keith, J. R.; Ganesan, V. *ACS Macro Letters* **2020**, *9*, 84–89, DOI: 10.1021/acsmacrolett.9b00908.

[25] Frenzel, F.; Guterman, R.; Anton, A. M.; Yuan, J.; Kremer, F. *Macromolecules* **2017**, *50*, 4022–4029, DOI: 10.1021/acs.macromol.7b00554.

[26] Griffin, P. J.; Freyer, J. L.; Han, N.; Geller, N.; Yin, X.; Gheewala, C. D.; Lambert, T. H.; Campos, L. M.; Winey, K. I. *Macromolecules* **2018**, *51*, 1681–1687, DOI: 10.1021/acs.macromol.7b02546.

[27] Fong, K. D.; Self, J.; McCloskey, B. D.; Persson, K. A. *Macromolecules* **2020**, *53*, 9503–9512, DOI: 10.1021/acs.macromol.0c02001.

[28] Lang, A.; Likos, C. N.; Watzlawek, M.; Löwen, H. *Journal of Physics: Condensed Matter* **2000**, *12*, 5087–5108, DOI: 10.1088/0953-8984/12/24/302.

[29] Leven, I.; Head-Gordon, T. *The Journal of Physical Chemistry Letters* **2019**, *10*, 6820–6826, DOI: 10.1021/acs.jpclett.9b02771.

[30] Ruppeiner, G.; Mausbach, P.; May, H.-O. *Fluid Phase Equilibria* **2021**, *542-543*, 113033, DOI: 10.1016/j.fluid.2021.113033.

[31] Ye, B. B.; Chen, S.; Wang, Z.-G. *Journal of Chemical Theory and Computation* **2024**, *20*, 6870–6880, DOI: 10.1021/acs.jctc.4c00603.

[32] Gartner, T. E.; Jayaraman, A. *Macromolecules* **2019**, *52*, 755–786, DOI: 10.1021/acs.macromol.8b01836.

[33] Joshi, S. Y.; Deshmukh, S. A. *Molecular Simulation* **2021**, *47*, 786–803, DOI: 10.1080/08927022.2020.1828583.

[34] Eastman, P.; Swails, J.; Chodera, J. D.; McGibbon, R. T.; Zhao, Y.; Beauchamp, K. A.; Wang, L.-P.; Simmonett, A. C.; Harrigan, M. P.; Stern, C. D.; Wiewiora, R. P.; Brooks, B. R.; Pande, V. S. *PLOS Computational Biology* **2017**, *13*, ed. by Gentleman, R., e1005659, DOI: 10.1371/journal.pcbi.1005659.

[35] Fong, K. D.; Bergstrom, H. K.; McCloskey, B. D.; Mandadapu, K. K. *AIChE Journal* **2020**, *66*, DOI: 10.1002/aic.17091.

[36] Shen, K.-H.; Hall, L. M. *Macromolecules* **2020**, *53*, 3655–3668, DOI: 10.1021/acs.macromol.0c00216.

[37] Shen, K.-H.; Fan, M.; Hall, L. M. *Macromolecules* **2021**, *54*, 2031–2052, DOI: 10.1021/acs.macromol.0c02557.

[38] Groot, R. D.; Warren, P. B. *The Journal of Chemical Physics* **1997**, *107*, 4423–4435, DOI: 10.1063/1.474784.

[39] Singh, T.; Kumar, A. *The Journal of Physical Chemistry B* **2008**, *112*, 12968–12972, DOI: 10.1021/jp8059618.

[40] Wang, X.; Zhang, S.; Yao, J.; Li, H. *Industrial & Engineering Chemistry Research* **2019**, *58*, 7352–7361, DOI: 10.1021/acs.iecr.9b00485.

[41] Kalathi, J. T.; Kumar, S. K.; Rubinstein, M.; Grest, G. S. *Macromolecules* **2014**, *47*, 6925–6931, DOI: 10.1021/ma500900b.

[42] Goto, S.; Kim, K.; Matubayasi, N. *The Journal of Chemical Physics* **2021**, *155*, DOI: 10.1063/5.0061281.

[43] Kashyap, H. K.; Annapureddy, H. V. R.; Raineri, F. O.; Margulis, C. J. *The Journal of Physical Chemistry B* **2011**, *115*, 13212–13221, DOI: 10.1021/jp204182c.

Chapter 4

SALT EFFECTS ON THE LINEAR AND NONLINEAR VISCOELASTIC RESPONSE OF SALT-DOPED POLYMERS

Polymer electrolytes (PEs) are promising materials for Li-ion batteries because they offer the possibility of combining high ion conductivity with mechanical robustness. Yet these properties are typically coupled in a way that makes their simultaneous enhancement challenging. The conditions that improve ion transport usually weaken the material, whereas greater mechanical rigidity tends to slow ion motion. To examine how salt affects this balance, we use coarse–grained molecular dynamics simulations and probe the linear and nonlinear viscoelastic response of PEO/LiTFSI. We find that the polymer radius of gyration depends non-monotonically on salt concentration, decreasing at low salt concentration and increasing again at higher salt concentration, consistent with a change in the Li^+ solvation environment. Under shear, however, this trend is reversed: because salt slows the chain relaxation, the same imposed shear rate leads to stronger flow-induced stretching at higher salt concentration. The steady-state shear viscosity exhibits a Newtonian plateau at low shear rates and shear thinning at higher shear rates, while the zero-shear viscosity increases near exponentially with salt concentration. Using the zero-shear viscosity together with the chain relaxation time, we find that the effective shear modulus monotonically increases over the concentration range studied here. In the linear viscoelastic regime, the stress relaxation modulus develops a shoulder and then a plateau-like regime with increasing salt concentration, indicating clear deviations from the simple Rouse model. Consistently, both the Rouse-mode analysis and the wavevector-dependent viscosity show that salt increases friction over a broad range of length scales, with the strongest effect at long wavelengths. These results show how salt concentration controls chain conformation, relaxation, and mechanical response in polymer electrolytes.

This chapter includes content from:

[1] Tsamopoulos, A. J.; Wang, Z.-G. Salt effect on the Linear and Nonlinear Viscoelastic Response of Polymer Electrolytes, *in preparation*, 2026.

4.1 Introduction

Polymer electrolytes (PEs) are ion–conducting materials in which a lithium salt is dissolved in a polar polymer host such as poly(ethylene oxide) (PEO) [1, 2]. PEs are promising alternatives to conventional liquid electrolytes for Li-ion batteries because they are nonvolatile and less flammable, can be chemically compatible with lithium-based electrodes, and can in principle serve as multifunctional separators that combine ion transport with mechanical support [3, 4]. However, their practical implementation remains limited by ionic conductivities that are generally lower than those of liquid electrolytes, low cation transference numbers, and the persistent difficulty of achieving simultaneously fast ion transport and sufficient mechanical rigidity [5, 6]. Furthermore, in PEO-based electrolytes, it is well known that lithium motion is strongly coupled to polymer segmental relaxation. As a result, the same factors that enhance conductivity often soften the material. At the same time, battery operation requires an electrolyte that remains mechanically robust enough to separate the electrodes and suppress dendrite growth [7, 8]. Therefore, it is important to understand the coupling between ion transport and mechanical response together to design electrolyte materials that can be utilized in Li-ion batteries.

The trade-off between ion transport and mechanical performance was explored in the theoretical work of Monroe and Newman [9] on the stability of lithium deposition at lithium/polymer interfaces. Using linear elasticity theory coupled with interfacial deposition kinetics, they showed that bulk stresses in the electrolyte can determine whether interfacial roughness is amplified or suppressed. For polymer electrolytes with Poisson ratio similar to that of PEO, they predicted that interfacial roughening can be mechanically suppressed when the electrolyte shear modulus exceeds about twice that of lithium. However, this stability regime lies well above the modulus of commonly studied polymer electrolytes, thereby highlighting the central challenge of combining sufficient mechanical rigidity with efficient ion transport.

More recently, Gudla *et al.* [10] examined the effect of salt concentration on the mechanical properties of PEO/LiTFSI using both nonequilibrium and equilibrium molecular dynamics simulations. They showed that salt concentration can significantly alter the viscoelastic response, and, despite the general trade-off between transport and mechanics, they identified an intermediate salt concentration at which the system exhibits both high ionic conductivity and high shear modulus, together with a relatively short elastic restoration time. However, no explanation was provided for this counterintuitive finding.

Because lithium transport in PEO-based electrolytes is strongly coupled to the local solvation environment and to polymer segmental motion, it is important to determine how added salt alters the equilibrium chain statistics of the polymer host, which in turn can affect the mechanical robustness of the material. The radius of gyration, R_g, provides a direct structural measure of this effect. Practically, R_g is not merely a geometric descriptor of the chain, but a probe of how lithium coordination reorganizes the polymer conformation. This question is particularly relevant in PEO/LiTFSI, where increasing salt concentration is known to produce nonmonotonic transport behavior, yet the microscopic relation between salt solvation, chain conformation, and thermodynamics has only recently begun to emerge [7, 8]. Loo and co-workers addressed this issue experimentally using small-angle neutron scattering on PEO/LiTFSI melts over a broad concentration range [7]. They found that the chain dimensions decrease systematically with increasing salt concentration in the low-salt regime, but reverse course and increase again above $r \approx 0.125$. The maximum reduction in chain size occurs near this crossover concentration. Their analysis further suggested that the change in R_g is correlated with Li–EO coordination, and that at higher salt concentration the system develops ionic aggregates that lead to chain expansion [7].

Fang and co-workers subsequently provided a molecular interpretation of this behavior using molecular dynamics simulations [8]. Their results reproduced the nonmonotonic concentration dependence of chain size and showed that the reversal occurs near the same critical concentration at which the activity coefficient develops a plateau. They traced both observations to a change in the Li^+ solvation structure. For $c_s < c_s^* \approx 1/6$, where $c_s = [Li^+]/[EO]$, Li^+ is coordinated almost entirely by about six ether oxygens from PEO, predominantly from a single chain, which drives the chain into a more compact local conformation. For $c_s > c_s^*$, the available EO coordination sites become saturated and $TFSI^-$ increasingly enters the Li^+ solvation shell, relaxing the compact cage and leading to chain re-expansion [8]. Taken together, these studies show that the salt dependence of R_g in PEO/LiTFSI is a direct manifestation of the underlying solvation structure. These results motivate studying R_g not as an isolated structural quantity, but as a thermodynamic and molecular indicator of how salt reorganizes the polymer host, modifies ion association, and ultimately influences transport in polymer electrolytes [7, 8]. Frenck *et al.* [11] studied lithium deposition through rigid block-copolymer electrolytes. They found that increasing salt concentration drastically reduced cell lifetime, and further showed that this trend could not be explained by salt-induced changes in morphol-

ogy or mechanical properties alone. Instead, their analysis indicated that protrusion growth correlates directly with the magnitude of the salt concentration gradient that develops under current. This result is particularly important because it shows that the relevant response of polymer electrolytes in operating cells is not fully captured by equilibrium structure or linear-response properties alone. These considerations motivate the study of polymer electrolytes under nonequilibrium conditions.

In this work, we use coarse–grained molecular dynamics simulations to examine the effect of salt concentration on the linear and nonlinear viscoelasticity of a PEO/LiTFSI-like polymer electrolyte. We show that the polymer radius of gyration depends non-monotonically on salt concentration, in agreement with previous experimental and simulation studies, and that this equilibrium salt effect is reversed under shear flow because salt also slows the chain relaxation. We further show that the zero-shear viscosity and effective modulus increase strongly with salt concentration, while the stress relaxation modulus develops clear deviations from the simple Rouse model. Analysis of the Rouse-mode relaxation times and the wavevector-dependent viscosity indicates that salt increases friction over a broad range of length scales, with the strongest effect at long wavelengths. Taken together, these results provide a molecular picture for how salt controls chain conformation, relaxation, and viscoelastic response in polymer electrolytes.

4.2 Simulation Method

Coarse-grained model and equilibrium simulations

We use the same coarse-grained model as in our previous work on salt-doped PEO/LiTFSI-like polymer electrolytes [12–14]. Each system contains 400 polymer chains, each of length $N = 30$, together with a number of cations and anions set by the salt concentration $c_s = [\mathrm{Li}^+]/[\mathrm{EO}]$. All simulations are performed in Lennard–Jones (LJ) units, and unless stated otherwise the results reported here correspond to $T = 1.0$. We take the LJ length scale to be $\sigma = 0.7$ nm, and all particles have the same mass $m = 1.0$.

Non-bonded interactions are described by the truncated and shifted LJ potential

$$U_{\mathrm{LJ}}(r_{ij}) = \begin{cases} 4\epsilon_{ij}\left[\left(\dfrac{\sigma_{ij}}{r_{ij}}\right)^{12} - \left(\dfrac{\sigma_{ij}}{r_{ij}}\right)^{6} - \left(\dfrac{\sigma_{ij}}{r_c}\right)^{12} + \left(\dfrac{\sigma_{ij}}{r_c}\right)^{6}\right], & r_{ij} \le r_c, \\ 0, & r_{ij} > r_c, \end{cases} \tag{4.1}$$

where r_{ij} is the distance between particles i and j. We use the same interaction energy for all pairs, $\epsilon_{ij} = \epsilon$, and set $\sigma_{ij} = (\sigma_i + \sigma_j)/2$. To represent the size

asymmetry of the PEO/LiTFSI system, we choose the polymer bead diameter to be σ, the cation diameter to be 0.4σ, and the anion diameter to be 1.6σ. For ion–ion, ion–monomer, and bonded monomer–monomer interactions, we use the purely repulsive Weeks–Chandler–Andersen cutoff $r_c = 2^{1/6}\sigma_{ij}$ [15]. For non-bonded monomer–monomer interactions, we choose $r_c = 2.0\sigma$ so that the attractive part of the potential is retained, which is necessary to reproduce glassy slowdown [16]

Chain connectivity is modeled by the finitely extensible nonlinear elastic (FENE) potential [17],

$$U_{\mathrm{FENE}}(r_{ij}) = -\frac{1}{2}KR_0^2 \ln\left(1 - \frac{r_{ij}^2}{R_0^2}\right), \tag{4.2}$$

with $K = 30\epsilon/\sigma^2$ and $R_0 = 1.5\sigma$. The strong Li^+–ether oxygen association is captured by the solvation potential proposed by Hall and co-workers [13, 18],

$$U_{\mathrm{solv}}(r_{ij}) = \begin{cases} -S_{ij}\left[\left(\dfrac{\sigma_{ij}}{r_{ij}}\right)^4 - \left(\dfrac{\sigma_{ij}}{r_c}\right)^4\right], & r_{ij} \le r_c, \\ 0, & r_{ij} > r_c, \end{cases} \tag{4.3}$$

for which we take $S_{ij} = 4.33$ and $r_c = 5.0\sigma$. Electrostatic interactions between ions are described by the Coulomb potential

$$U_{\mathrm{Coul}}(r_{ij}) = \frac{q_i q_j}{4\pi\epsilon_0\epsilon_r r_{ij}}, \tag{4.4}$$

with dielectric constant $\epsilon_r = 7.5$, and are evaluated using the particle–particle particle–mesh solver [19]. All simulations are performed with LAMMPS [20]. Equilibrium configurations are prepared using the velocity-Verlet algorithm with time step $\Delta t = 0.005\tau$ together with the Nosé–Hoover thermostat and barostat [**doi:10.1080/00268979600100761**]. The thermostat and barostat damping constants are both set to 1.0τ, and the pressure is fixed at $p = 0.08\sigma^{-3}$. For the present work, we focus on fully equilibrated states at $T = 1.0$ for the range of salt concentrations studied. From these equilibrium trajectories we compute the chain dimensions, end-to-end autocorrelation function, stress relaxation modulus, storage and loss moduli, Rouse-mode relaxation times, and wavevector-dependent viscosity. All reported quantities are obtained by block averaging over at least four statistically independent trajectory segments.

Nonequilibrium shear simulations

The nonlinear rheology is examined by nonequilibrium molecular dynamics simulations under homogeneous shear flow. Starting from the equilibrated configurations

described above, the NEMD simulations are performed in the NVT ensemble using the p-SLLOD equations of motion together with the Nosé–Hoover thermostat and Lees–Edwards boundary conditions [21–25]. The set of microscopic p-SLLOD equations of motion reads

$$\dot{\mathbf{q}}_{ia} = \frac{\mathbf{p}_{ia}}{m_{ia}} + \mathbf{q}_{ia} \cdot \nabla \mathbf{u} \tag{4.5}$$

$$\dot{\mathbf{p}}_{ia} = \mathbf{F}_{ia} - \mathbf{p}_{ia} \cdot \nabla \mathbf{u} - m_{ia} \mathbf{q}_{ia} \cdot \nabla \mathbf{u} \cdot \nabla \mathbf{u} - \frac{p_\zeta}{Q} \mathbf{p}_{ia} \tag{4.6}$$

$$\dot{\zeta} = \frac{p_\zeta}{Q} \tag{4.7}$$

$$\dot{p}_\zeta = \sum_i \sum_a \frac{\mathbf{p}_{ia}^2}{m_{ia}} - 3nk_\mathrm{B}T, \tag{4.8}$$

where $\mathbf{p}_{ia}$, $\mathbf{q}_{ia}$, and $\mathbf{F}_{ia}$ are the momentum, position, and force of atom a in molecule i, of mass m_{ia}. Here, n denotes the total number of atoms, T the absolute temperature and k_B the Boltzmann constant. The variables ζ and p_ζ are the coordinate- and momentum-like variables of the Nosé–Hoover thermostat, and $Q = Dnk_\mathrm{B}T\tau^2$ is the thermostat mass parameter. Flow is imposed through the velocity gradient tensor $\nabla \mathbf{u}$. For simple shear,

$$\nabla \mathbf{u} = \begin{bmatrix} 0 & 0 & 0 \\ \dot{\gamma} & 0 & 0 \\ 0 & 0 & 0 \end{bmatrix}, \tag{4.9}$$

where $\dot{\gamma}$ is the imposed strain rate. For this flow, the term $m_{ia}\mathbf{q}_{ia} \cdot \nabla \mathbf{u} \cdot \nabla \mathbf{u}$ in Eq. 4.6 vanishes. In conjunction with the Lees–Edwards boundary conditions, the p-SLLOD equations generate the correct velocity gradient under periodic boundary conditions [24, 25]. At each imposed shear rate, the system is first evolved until the stress reaches a steady state. The steady-state shear viscosity is then obtained from the off-diagonal stress tensor as

$$\eta(\dot{\gamma}) = \frac{\langle \sigma_{xy} \rangle}{\dot{\gamma}}. \tag{4.10}$$

Here, σ_{xy} is the microscopic shear stress, calculated from the virial expression as

$$\sigma_{xy} = -\frac{1}{V} \left[\sum_{j=1}^{n} \frac{p_{j,x} p_{j,y}}{m_j} + \sum_{j=1}^{n} q_{j,x} F_{j,y} \right], \tag{4.11}$$

where V is the system volume, m_j is the mass of atom j, $p_{j,x}$ and $p_{j,y}$ are the x and y components of its peculiar momentum, and $q_{j,x}$ and $F_{j,y}$ are the x component of its position and the y component of the force acting on it, respectively. The dependence of η on $\dot{\gamma}$ is used to characterize the nonlinear response and to extract the zero-shear viscosity by fitting the low-rate data to the Carreau form discussed below.

4.3 Results and Discussion

Non-linear Viscoelastic Response

We begin by examining the equilibrium chain conformation, which provides the structural baseline for the nonlinear response under shear. As shown in Fig. 4.1, the polymer radius of gyration, R_g, exhibits a clear non-monotonic dependence on salt concentration, c_s: it decreases upon initial salt addition, reaches a minimum near $c_s \approx 0.14$, and then increases again at higher salt concentration. The overall reduction from neat PEO to the minimum is about 10%. This is in good qualitative agreement with earlier experimental and simulation studies on PEO/LiTFSI, where Loo and co-workers reported that the chain dimensions decrease systematically with increasing salt concentration at low salt loading before reversing above $r \approx 0.125$. Further, Fang and co-workers reproduced the same trend using molecular dynamics simulations, with the reversal occurring near the same critical concentration [7, 8]. This non-monotonic dependence can be understood in terms of the Li^+ solvation environment: at low salt concentration, Li^+ is coordinated primarily by ether oxygens on PEO, often from a single chain, which favors locally compact conformations and contracts the polymer coil, whereas beyond the crossover concentration the available EO coordination sites become progressively saturated and $TFSI^-$ increasingly enters the Li^+ solvation shell, relaxing the compact PEO coordination cage and allowing the chain to expand again [7, 8].

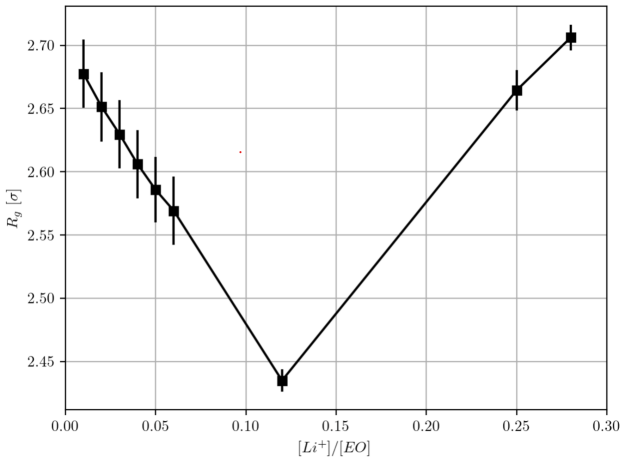

Figure 4.1: Polymer radius of gyration, R_g, as a function of salt concentration, c_s. R_g decreases upon salt addition at low c_s, reaches a minimum near $c_s \approx 0.14$, and then increases again at higher salt concentration, indicating a non-monotonic dependence of chain size on salt loading.

To examine how flow modifies the salt dependence of chain conformation, we next

plot the polymer radius of gyration, R_g, as a function of salt concentration, c_s, for a series of imposed shear rates, $\dot{\gamma}$. Here we focus on the low- to intermediate-salt regime, where under equilibrium conditions the addition of salt decreases R_g, as discussed above. Therefore, for the concentration range shown in Fig. 4.2, the zero-shear data should isolate the contracting branch of the equilibrium response. As expected, increasing the shear rate raises the overall magnitude of R_g due to flow-induced chain stretching. More importantly, the dependence on salt concentration changes qualitatively with increasing $\dot{\gamma}$. At $\dot{\gamma} = 0$, R_g decreases with c_s. At weak shear, this decrease persists but becomes progressively weaker. At sufficiently large shear rates, the trend reverses, and R_g instead increases with salt concentration. The effect of salt on chain conformation is thus reversed by the imposed shear.

This reversal can be understood as the result of two competing effects of salt addition. At equilibrium, Li^+ coordination with ether oxygens promotes locally compact conformations and reduces the chain size. Under shear, however, salt also slows the polymer relaxation. The chain then has less time to relax the deformation imposed by the flow and remains more strongly oriented and stretched. Once the flow is sufficiently strong, this dynamical effect overtakes the equilibrium compaction and leads to an increase in R_g with c_s. Thus, comparisons at fixed $\dot{\gamma}$ should be interpreted with caution. Because the polymer relaxation time depends on salt concentration, the same imposed shear rate corresponds to different Weissenberg numbers, $Wi = \dot{\gamma}\tau_R(c_s)$, at different c_s. Part of the apparent salt-induced increase of R_g in Fig. 4.2 may therefore reflect the fact that increasing salt moves the system to a larger effective flow strength, even when $\dot{\gamma}$ is held fixed. A more meaningful comparison is thus at fixed Wi, which requires an independent measure of the salt-dependent relaxation time.

We quantify the salt dependence of the polymer relaxation, by calculating the normalized autocorrelation function of the end-to-end vector,

$$C_{ee}(t) = \frac{\langle \mathbf{R}_{ee}(t) \cdot \mathbf{R}_{ee}(0) \rangle}{\langle R_{ee}^2 \rangle}, \tag{4.12}$$

where $\mathbf{R}_{ee}$ denotes the polymer end-to-end vector. As shown in Fig. 4.3a, the decay of $C_{ee}(t)$ shifts systematically to longer times as the salt concentration increases. This result confirms that salt addition leads to a monotonic slowdown of the chain relaxation. We extract the characteristic relaxation time, by fitting the autocorrelation

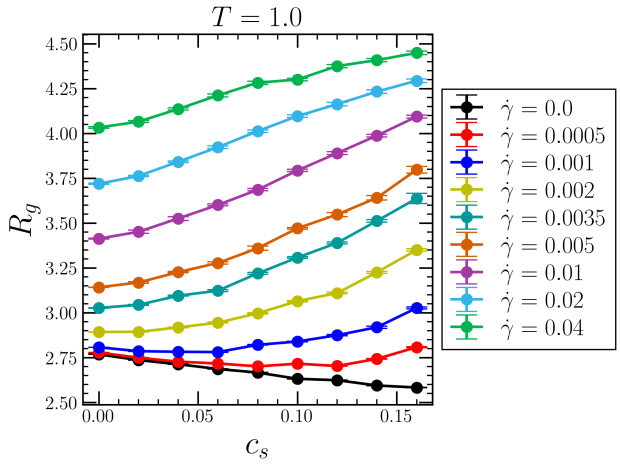

Figure 4.2: Polymer radius of gyration, R_g, as a function of salt concentration, c_s, for various shear rates, $\dot{\gamma}$, at $T = 1.0$. Over the concentration range shown, the zero-shear data correspond to the regime where salt addition contracts the chain. This equilibrium trend weakens with increasing shear rate and is eventually reversed, such that at sufficiently strong shear R_g increases with c_s.

function to the stretched-exponential Kohlrausch–Williams–Watts form,

$$C_{ee}(t) = \exp\left[-\left(\frac{t}{\tau_{\mathrm{KWW}}}\right)^{\beta}\right]. \tag{4.13}$$

We then define the relaxation time as the area under the fitted curve,

$$\tau_R = \frac{\tau_{\mathrm{KWW}}}{\beta}\Gamma\left(\frac{1}{\beta}\right), \tag{4.14}$$

where Γ denotes the Gamma function.

As shown in Fig. 4.3b, the extracted τ_R increases with salt concentration. These results also clarify the shear-induced reversal in Fig. 4.2. Because τ_R increases with c_s, a fixed shear rate corresponds to a progressively larger Weissenberg number at higher salt concentration. The stronger flow-induced extension observed at larger c_s is therefore not inconsistent with the equilibrium contraction of the chain. Rather, salt plays a dual role. It compacts the chain at equilibrium over the low- to intermediate-concentration regime, but it also slows the relaxation strongly enough that under shear the chain becomes more susceptible to flow-induced stretching.

Figure 4.4a shows the radius of gyration, R_g, as a function of shear rate, $\dot{\gamma}$, for the different salt concentrations. For all concentrations, R_g increases monotonically with increasing shear rate, indicating progressive chain deformation under flow. At fixed $\dot{\gamma}$, the salt-doped systems exhibit larger R_g than the neat polymer, and the

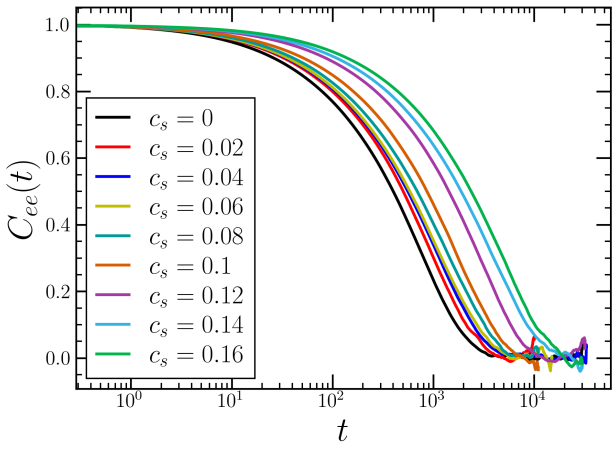

(a)

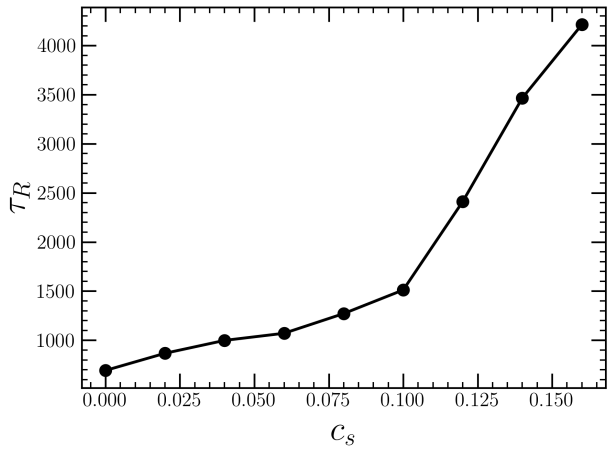

(b)

Figure 4.3: (a) Normalized end-to-end autocorrelation function, $C_{ee}(t)$, for various salt concentrations, c_s. (b) Relaxation time, τ_R, obtained from stretched-exponential fits of $C_{ee}(t)$ to the Kohlrausch–Williams–Watts form. The systematic shift of the decay to longer times with increasing c_s indicates that salt addition slows the polymer relaxation monotonically.

increase becomes more pronounced as c_s increases. Thus, when plotted against $\dot{\gamma}$, the chains at higher salt concentration appear to respond more strongly to the imposed flow.

The same data are shown in Figure 4.4b as a function of the Weissenberg number, Wi. When plotted in this form, the data for all salt concentrations collapse reasonably well onto a single master curve. This collapse shows that the shear-induced increase in R_g is controlled primarily by the ratio of the imposed deformation rate to the intrinsic chain relaxation time. At low Wi, R_g increases rapidly with increasing Wi, while at larger Wi the increase becomes weaker, suggesting a gradual approach

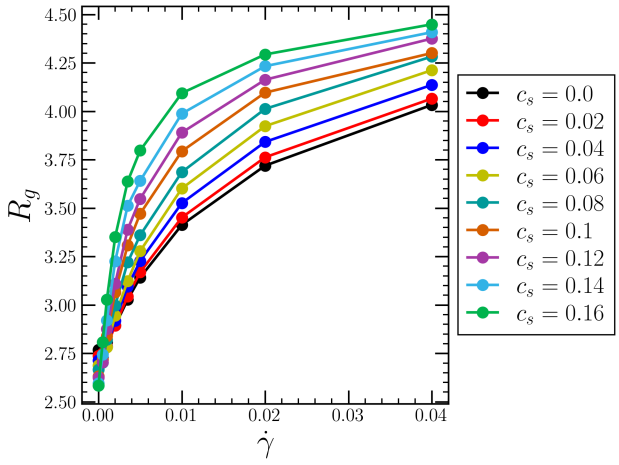

(a)

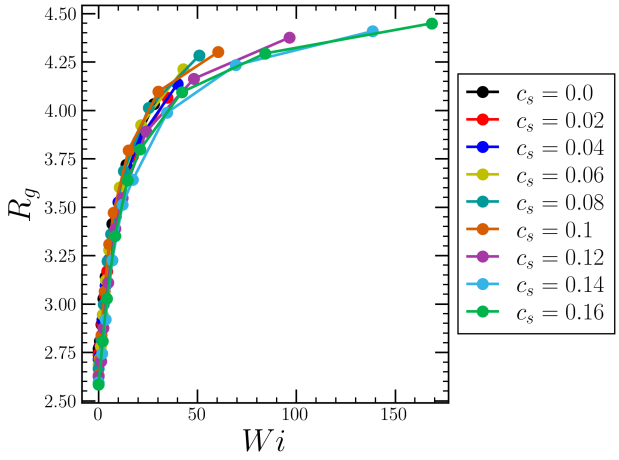

(b)

Figure 4.4: (a) Radius of gyration, R_{g}, as a function of shear rate, $\dot{\gamma}$, for various salt concentrations, c_{s}. (b) The same data plotted as a function of Weissenberg number, Wi. While R_{g} increases monotonically with $\dot{\gamma}$ for all c_{s}, plotting the data against Wi leads to an approximate collapse onto a single master curve. This result indicates that the shear-induced chain stretching is governed primarily by the competition between the imposed flow rate and the intrinsic chain relaxation time.

toward a highly deformed state.

The collapse with Wi suggests that the main effect of salt is to renormalize the relaxation time of the chains rather than to alter the underlying deformation mechanism. In other words, at fixed $\dot{\gamma}$, chains at higher salt concentration appear more extended because salt slows down their relaxation and therefore shifts them to larger effective Wi. Once the shear rate is rescaled by the appropriate relaxation time, the response becomes nearly universal. This result indicates that the shear-induced change in chain size is governed mainly by the competition between flow and chain relaxation, while the role of salt enters primarily through its effect on the relaxation dynamics.

Having established that salt addition slows the polymer relaxation, we next examine its consequence for the nonlinear rheology. In Fig. 4.5, we plot the steady-state shear viscosity, η, as a function of the imposed shear rate, $\dot{\gamma}$, for various salt concentrations, c_s, at $T = 1.0$. For all concentrations, we observe the characteristic behavior of polymer melts under shear. At low shear rates, the viscosity is nearly constant, defining the Newtonian plateau. At higher shear rates, the viscosity decreases with increasing $\dot{\gamma}$, indicating shear thinning.

The most notable effect of salt is that the entire viscosity curve shifts upward with increasing c_s. Thus, at a given shear rate, the salt-doped systems are more viscous than the neat polymer melt. This trend is consistent with the monotonic increase in the polymer relaxation time discussed above. The addition of salt strengthens the ion–polymer coupling, slows the segmental dynamics, and therefore increases the resistance to flow. At the same time, the shear-thinning regime remains present at all concentrations, showing that the material response crosses over from linear to nonlinear rheology once the imposed deformation rate becomes comparable to the intrinsic relaxation rate of the chains.

Because the calculation of the stress tensor at very low shear rates is subject to significant statistical fluctuations in nonequilibrium molecular dynamics simulations, the zero-shear viscosity cannot always be determined directly from the lowest-$\dot{\gamma}$ data points. To estimate the zero-shear viscosity, η_0, we fit the simulation data to the Carreau model [26, 27],

$$\eta(\dot{\gamma}) = \eta_0 \left[1 + (\lambda\dot{\gamma})^2\right]^{-p}, \tag{4.15}$$

where λ is a characteristic time scale and p is a fitting exponent. As shown by the dashed lines in Fig. 4.5, the Carreau model provides a good description of the data

over the full range of shear rates examined. The fitted values of η_0 therefore provide a convenient measure of how salt concentration alters the linear-response viscosity.

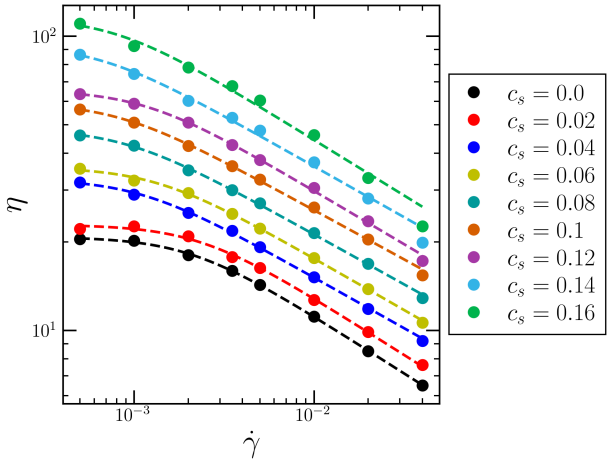

Figure 4.5: Steady-state shear viscosity, η, as a function of shear rate, $\dot{\gamma}$, for various salt concentrations, c_s, at $T = 1.0$. At low shear rates, the viscosity approaches a Newtonian plateau, while at higher shear rates the systems exhibit shear thinning. Dashed lines are fits to the Carreau model [26, 27].

In Fig. 4.6(a), we plot the zero-shear viscosity, η_0, obtained from the Carreau fits, as a function of c_s. η_0 increases strongly and approximately exponentially with salt concentration. This behavior is consistent with the results of Mongcopa and co-workers [28, 29], who found a similar salt dependence for the monomeric friction coefficient. The increase in η_0 therefore reflects the progressive slowdown of polymer relaxation caused by stronger ion–polymer coupling.

Since the zero-shear viscosity is related to the relaxation time and plateau modulus through $\eta_0 \sim G\tau_R$, we use the measured η_0 together with τ_R to estimate an effective shear modulus. In Fig. 4.6(b), we plot the resulting modulus G normalized by its zero-salt value, G_0. We find that G/G_0 increases monotonically with c_s and reaches more than a fivefold increase over the concentration range studied here. Thus, salt addition enhances not only the viscosity, but also the elastic stiffness of the material. We note that our highest salt concentrations are well above the concentration at which the conductivity is maximized. Thus, for the systems studied here, the salt concentration at which the conductivity is largest does not coincide with the concentration at which the mechanical response is strongest. Instead, the mechanical robustness increases monotonically with c_s. This trend may arise from the increasing number of ion-mediated physical crosslinks, which reinforce the polymer matrix as salt is added.

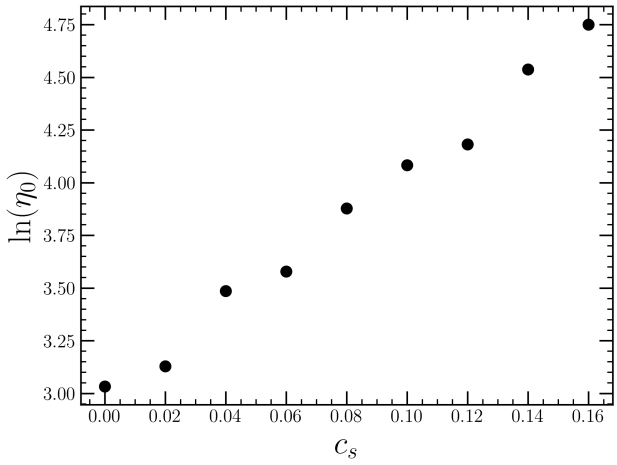

(a)

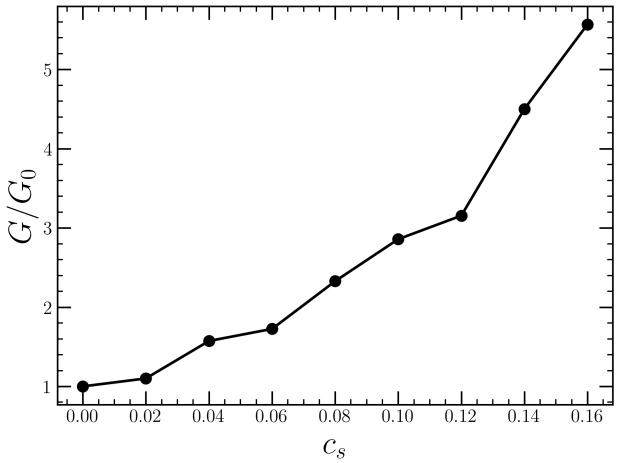

(b)

Figure 4.6: (a) Zero-shear viscosity, η_0, as a function of salt concentration, c_s, obtained from the Carreau fits. (b) Shear modulus, G, normalized by its zero-salt value, G_0, as a function of c_s, estimated from $\eta_0 \sim G\tau_R$.

Linear Viscoelastic Response

We now turn to the linear viscoelasticity. In Fig. 4.7a, we plot the stress relaxation modulus, $G(t)$, for various salt concentrations. For the neat polymer melt, the decay is in good agreement with the simple Rouse picture. With increasing salt concentration, however, clear deviations develop. The relaxation becomes progressively slower, and $G(t)$ develops a "shoulder" that evolves into a plateau at the highest salt concentrations. Similar trends have been found for associative polymer melts [30, 31].

To examine these deviations more closely, in Fig. 4.7b we plot $G(t)t^{1/2}$. For a Rouse melt, this quantity should be approximately constant over the intermediate-

time regime. This is indeed the case for $c_s = 0$. By contrast, the salt-doped systems show a clear upward deviation, which becomes stronger with increasing c_s. The apparent scaling is therefore much stronger than the Rouse prediction, and the discrepancy grows systematically with salt concentration. Thus, salt addition drives the system away from simple Rouse behavior. A sticky-Rouse description is a natural first route, since such models can produce shoulders and plateau-like features in $G(t)$ when slow sticky modes are added to the underlying chain relaxation [30]. At the same time, our data suggest that this picture is incomplete, because the short-time modulus also increases with c_s, and the Sticky-Rouse cannot capture such behavior. A heterogeneous Rouse description may therefore be more appropriate, since it allows for a distribution of local mobilities and corresponding deviations from simple Rouse relaxation [32]. A detailed analysis along these lines will be pursued in future work.

We next examine the storage and loss moduli, $G'(\omega)$ and $G''(\omega)$, obtained from the stress relaxation modulus through

$$G'(\omega) = \omega \int_0^\infty G(t) \sin(\omega t)\, dt \tag{4.16}$$

and

$$G''(\omega) = \omega \int_0^\infty G(t) \cos(\omega t)\, dt. \tag{4.17}$$

$G'(\omega)$ measures the elastic part of the response, while $G''(\omega)$ measures the viscous part.

The results for $c_s = 0$, 0.08, 0.16, and 0.24 are shown in Figs. 4.8 and 4.9. For the neat polymer melt and at low salt concentration, we find $G'' > G'$ over the full frequency range shown, indicating predominantly viscous-like behavior [33]. With increasing salt concentration, however, $G'(\omega)$ rises relative to $G''(\omega)$, and the material becomes progressively more solid-like. At $c_s = 0.16$, the two moduli nearly overlap over an intermediate frequency range. At $c_s = 0.24$, we find a clear crossover from a viscous-dominated response at low frequency to an elastic-dominated response at intermediate frequency, followed by a second crossover at higher frequency. These trends are consistent with the slower stress relaxation discussed above and show that salt addition shifts the viscoelastic response toward a more elastic and glassy state.

Next, we examine whether the Cox–Merz rule holds for this system. This empirical rule states that the complex viscosity at frequency ω is equal to the steady-state

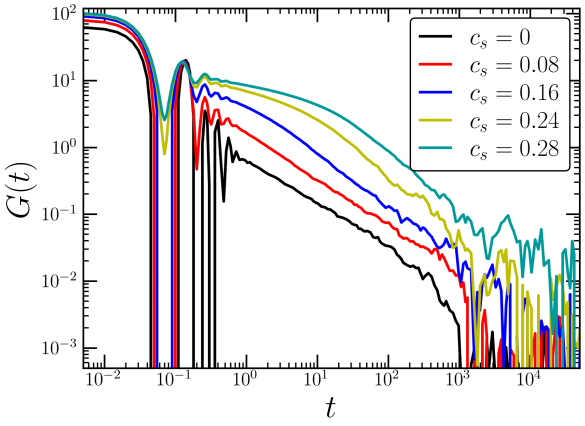

(a)

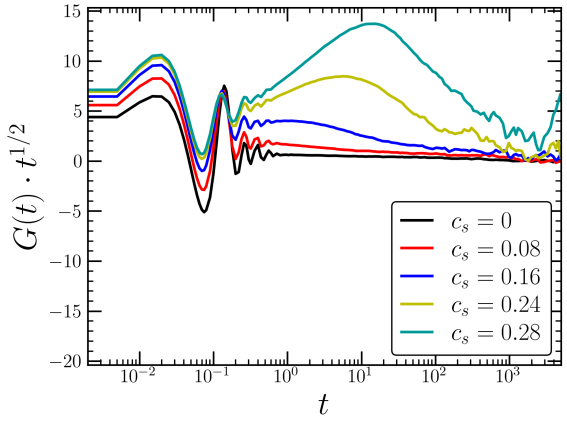

(b)

Figure 4.7: (a) Stress relaxation modulus, $G(t)$, for various salt concentrations, c_s. (b) Same data plotted as $G(t)t^{1/2}$ to highlight deviations from the Rouse scaling.

shear viscosity at the same value of shear rate, i.e., $\eta^*(\omega) = \eta(\dot{\gamma})$ for $\omega = \dot{\gamma}$. The complex viscosity is calculated from the storage and loss moduli as

$$\eta^*(\omega) = \frac{\sqrt{G'(\omega)^2 + G''(\omega)^2}}{\omega}. \tag{4.18}$$

In Fig. 4.10, we compare $\eta^*(\omega)$ with the steady-state viscosity $\eta(\dot{\gamma})$ for several salt concentrations. We find good agreement over the concentration range shown. Thus, the Cox–Merz rule appears to be applicable for our system, at least for the salt concentrations examined here.

To quantify the lengthscale-dependent friction, we next perform a Rouse-mode

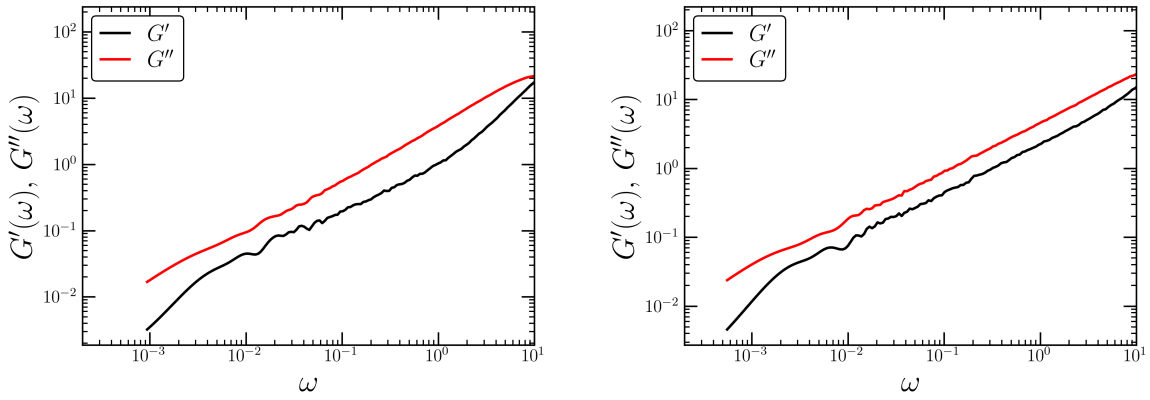

(a) (b)

Figure 4.8: (a)–(b) Storage modulus, $G'(\omega)$, and loss modulus, $G''(\omega)$, for $c_s = 0$ and 0.08, respectively.

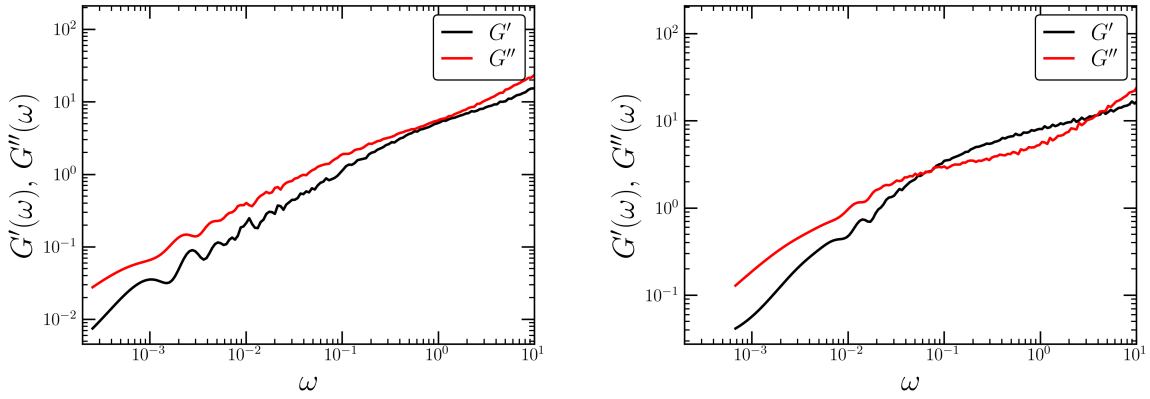

(a) (b)

Figure 4.9: (a)–(b) Storage modulus, $G'(\omega)$, and loss modulus, $G''(\omega)$, for $c_s = 0.16$ and 0.24, respectively.

analysis. The pth Rouse mode is defined as

$$\mathbf{X}_p = \left(\frac{2}{N}\right)^{1/2} \sum_{i=1}^{N} \mathbf{r}_i \cos\left[\frac{p\pi}{N}\left(i - \frac{1}{2}\right)\right], \tag{4.19}$$

and its autocorrelation is fitted to

$$\langle \mathbf{X}_p(t) \cdot \mathbf{X}_p(0) \rangle = \langle X_p^2 \rangle \exp\left[-\left(\frac{t}{\tau_p}\right)^{\beta_p}\right]. \tag{4.20}$$

From the fit, we define the effective relaxation time

$$\tau_p = \frac{\tau_{kww}}{\beta_p} \Gamma\left(\frac{1}{\beta_p}\right). \tag{4.21}$$

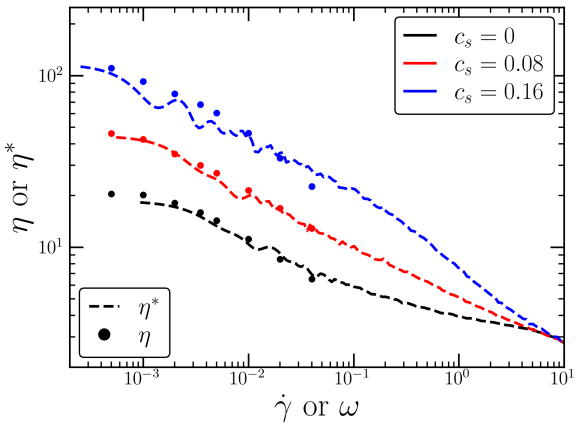

Figure 4.10: Comparison of the complex viscosity, $\eta^*(\omega)$, and the steady-state shear viscosity, $\eta(\dot{\gamma})$, for various salt concentrations, c_s. The agreement supports the applicability of the Cox–Merz rule for the concentration range shown.

In the Rouse model, the mode relaxation time is given by

$$\tau_p = \frac{\zeta b^2}{12 k_B T} \sin^{-2}\left(\frac{p\pi}{2N}\right), \tag{4.22}$$

where ζ is the monomeric friction coefficient and b is the statistical segment length. For large N and small p/N, this reduces to the familiar scaling $\tau_p \sim p^{-2}$.

In Fig. 4.11, we plot τ_p as a function of $1/p$. The neat polymer is reasonably close to the Rouse prediction, but clear deviations develop with increasing salt concentration. The relaxation times shift upward for all modes, and the departure from the Rouse scaling becomes progressively stronger. Thus, salt slows the dynamics over a broad range of *subchain* length scales and introduces a clear non-Rouse character.

A complementary measure of the lengthscale-dependent viscous response is the wavevector-dependent viscosity, $\eta(k)$. It is obtained from NVT simulations with a DPD thermostat and calculated from the transverse velocity autocorrelation function:

$$C_{uu}^{\perp}(\mathbf{k}, t) = \frac{1}{V} \langle \delta\tilde{\mathbf{u}}_{\perp}(\mathbf{k}, t) \cdot \delta\tilde{\mathbf{u}}_{\perp}(-\mathbf{k}, 0) \rangle , \tag{4.23}$$

with

$$\delta\tilde{\mathbf{u}}_{\perp}(\mathbf{k}, t) = \frac{1}{\rho_m} \sum_{i=1}^{N} m_i \left[\mathbf{v}_i(t) - (\mathbf{v}_i(t) \cdot \hat{\mathbf{k}})\hat{\mathbf{k}}\right] e^{-i\mathbf{k}\cdot\mathbf{r}_i(t)}, \tag{4.24}$$

through the zero-frequency relation

$$\eta(k) = \frac{\rho_m}{k^2} \frac{C_{uu}^{\perp}(k, 0)}{\tilde{C}_{uu}^{\perp}(k, 0)}. \tag{4.25}$$

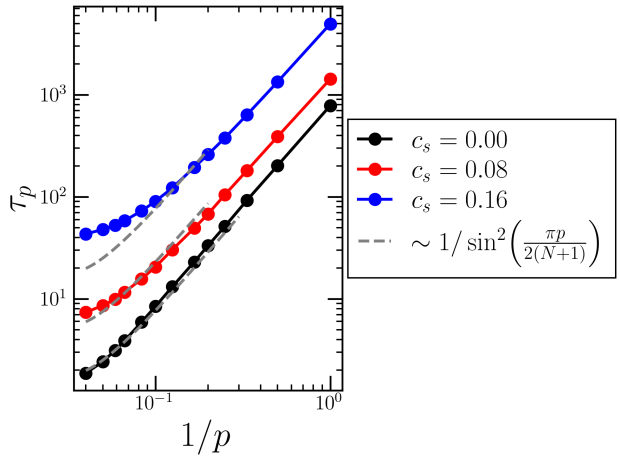

Figure 4.11: Effective Rouse-mode relaxation time, τ_p, as a function of $1/p$ for various salt concentrations, c_s. The dashed line indicates the Rouse scaling, $\tau_p \sim \sin^{-2}\left(\frac{p\pi}{2N}\right)$.

Here, $\tilde{C}^{\perp}_{uu}(k,0) = \int_0^\infty C^{\perp}_{uu}(k,t)\,dt$ denotes the zero-frequency Fourier–Laplace transform.

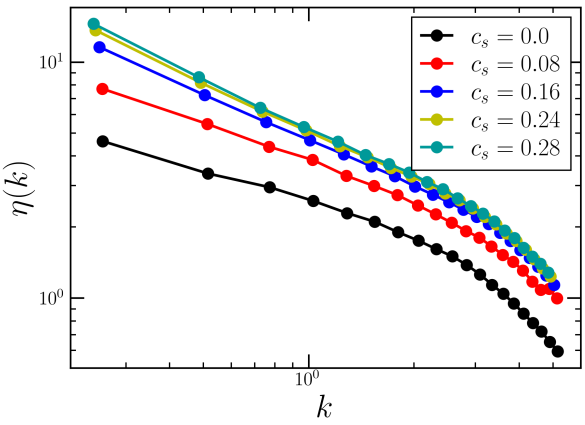

Figure 4.12: Wave-vector-dependent viscosity, $\eta(k)$, as a function of wavevector, k, for various salt concentrations, c_s.

The results are shown in Fig. 4.12. For all salt concentrations, $\eta(k)$ decreases with increasing k, indicating that the effective viscosity is smaller on shorter length scales. At the same time, increasing salt shifts $\eta(k)$ upward over the full k range. The separation between the curves is largest at small k and becomes weaker at larger k. Relating the mode-dependent chain relaxation to the lengthscale–dependent viscous response remains an important direction for future work.

4.4 Conclusions

In this work, we used coarse–grained molecular dynamics simulations to examine how salt concentration controls the equilibrium chain conformation and the linear and nonlinear viscoelastic response of a PEO/LiTFSI. In agreement with previous works, we showed that the polymer radius of gyration depends non-monotonically on salt concentration, decreasing at low salt concentration and increasing again at higher salt concentration, consistent with a change in the Li^+ solvation environment. Under shear, however, this equilibrium salt effect is reversed, as salt–doping also slows the chain relaxation and thereby shifts the system to larger effective Weissenberg numbers at fixed imposed shear rate. The steady-state shear viscosity exhibits the expected Newtonian plateau and shear-thinning regime, while the zero-shear viscosity increases strongly with salt concentration. Using the zero-shear viscosity together with the chain relaxation time, we found that the effective modulus also increases substantially over the concentration range studied here. In the linear viscoelastic regime, the stress relaxation modulus develops a shoulder and then a plateau-like regime with increasing salt concentration, indicating clear deviations from the simple Rouse model. The Rouse-mode analysis shows that salt increases friction over a broad range of length scales, with the strongest enhancement at small lengthscales/timescales. On the other hand, the wavevector-dependent viscosity exhibits stronger deviations at lower k. Taken together, these results show that salt addition does not simply slow the dynamics, but qualitatively reshapes the conformation, relaxation, and mechanical response of polymer electrolytes.

Several important directions emerge from this work. A first question is how the imposed shear rate affects the Li^+ coordination and local solvation environment, and whether the shear-induced reversal in chain conformation is due to a corresponding change in ion solvation. Related to this is whether the solvation environment becomes similar at fixed Weissenberg number, even for systems with different salt concentrations. A second direction is to determine how salt doping affects the polymer tumbling timescale under shear, and how this timescale relates to the R_g distribution. It will also be important to establish a more quantitative connection between the mode-dependent chain relaxation and the lengthscale-dependent viscous response. Addressing these questions should provide a more complete picture of how ion coordination, flow, and chain dynamics combine to determine the rheology of polymer electrolytes.

References

[1] Fenton, D. E.; Parker, J. M.; Wright, P. V. *Polymer* **1973**, *14*, 589, DOI: 10.1016/0032-3861(73)90146-8.

[2] Armand, M. B. *Annual Review of Materials Research* **1986**, *16*, 245–261, DOI: 10.1146/annurev.ms.16.080186.001333.

[3] Miller, T. F. I.; Wang, Z.-G.; Coates, G. W.; Balsara, N. P. *Accounts of Chemical Research* **2017**, *50*, 590–593, DOI: 10.1021/acs.accounts.6b00568.

[4] Hallinan, D. T.; Balsara, N. P. *Annual Review of Materials Research* **2013**, *43*, 503–525, DOI: 10.1146/annurev-matsci-071312-121705.

[5] Lascaud, S.; Perrier, M.; Vallee, A.; Besner, S.; Prud'homme, J.; Armand, M. *Macromolecules* **1994**, *27*, 7469–7477, DOI: 10.1021/ma00103a034.

[6] Nikolakakou, G.; Pantazidis, C.; Sakellariou, G.; Glynos, E. *Macromolecules* **2022**, *55*, 6131–6139, DOI: 10.1021/acs.macromol.2c00620.

[7] Loo, W. S.; Mongcopa, K. I.; Gribble, D. A.; Faraone, A. A.; Balsara, N. P. *Macromolecules* **2019**, *52*, 8724–8732, DOI: 10.1021/acs.macromol.9b01509.

[8] Fang, C.; Loo, W. S.; Wang, R. *Macromolecules* **2021**, *54*, 2873–2881, DOI: 10.1021/acs.macromol.0c01850.

[9] Monroe, C.; Newman, J. *Journal of The Electrochemical Society* **2005**, *152*, A396, DOI: 10.1149/1.1850854.

[10] Gudla, H.; Edström, K.; Zhang, C. *ACS Materials Au* **2024**, acsmaterialsau.3c00098, DOI: 10.1021/acsmaterialsau.3c00098.

[11] Frenck, L.; Veeraraghavan, V. D.; Maslyn, J. A.; Müller, A.; Ho, A. S.; Loo, W. S.; Minor, A. M.; Balsara, N. P. *Solid State Ionics* **2020**, *358*, 115517, DOI: 10.1016/j.ssi.2020.115517.

[12] Shen, K.-H.; Hall, L. M. *Macromolecules* **2020**, *53*, 3655–3668, DOI: 10.1021/acs.macromol.0c00216.

[13] Shen, K.-H.; Hall, L. M. *Macromolecules* **2020**, *53*, 10086–10096, DOI: 10.1021/acs.macromol.0c02161.

[14] Tsamopoulos, A. J.; Wang, Z.-G. *ACS Macro Letters* **(2024)**, 322–327, DOI: 10.1021/acsmacrolett.3c00757.

[15] Weeks, J. D.; Chandler, D.; Andersen, H. C. *The Journal of Chemical Physics* **1971**, *54*, 5237–5247, DOI: 10.1063/1.1674820.

[16] Morita, H.; Tanaka, K.; Kajiyama, T.; Nishi, T.; Doi, M. *Macromolecules* **2006**, *39*, 6233–6237, DOI: 10.1021/ma052632h.

[17] Kremer, K.; Grest, G. S. *The Journal of Chemical Physics* **1990**, *92*, 5057–5086, DOI: 10.1063/1.458541.

[18] Brown, J. R.; Seo, Y.; Sides, S. W.; Hall, L. M. *Macromolecules* **2017**, *50*, 5619–5626, DOI: 10.1021/acs.macromol.7b00522.

[19] Brown, W. M.; Wang, P.; Plimpton, S. J.; Tharrington, A. N. *Computer Physics Communications* **2011**, *182*, 898–911, DOI: 10.1016/j.cpc.2010.12.021.

[20] Plimpton, S. *Journal of Computational Physics* **1995**, *117*, 1–19, DOI: 10.1006/jcph.1995.1039.

[21] Baig, C.; Edwards, B. J.; Keffer, D. J.; Cochran, H. D. *The Journal of Chemical Physics* **2005**, *122*, 114103, DOI: 10.1063/1.1819869.

[22] Edwards, B. J.; Baig, C.; Keffer, D. J. *The Journal of Chemical Physics* **2005**, *123*, 114106, DOI: 10.1063/1.2035079.

[23] Nosé, S. *The Journal of Chemical Physics* **1984**, *81*, 511–519, DOI: 10.1063/1.447334.

[24] Lees, A. W.; Edwards, S. F. *Journal of Physics C: Solid State Physics* **1972**, *5*, 1921, DOI: 10.1088/0022-3719/5/15/006.

[25] Todd, B. D.; Daivis, P. J., *Nonequilibrium Molecular Dynamics: Theory, Algorithms and Applications*, 1st ed.; Cambridge University Press: 2017, DOI: 10.1017/9781139017848.

[26] Borodin, O.; Smith, G. D.; Kim, H. *The Journal of Physical Chemistry B* **2009**, *113*, 4771–4774, DOI: 10.1021/jp810016e.

[27] Kelkar, M. S.; Maginn, E. J. *The Journal of Physical Chemistry B* **2007**, *111*, 4867–4876, DOI: 10.1021/jp0686893 Publisher: American Chemical Society.

[28] Mongcopa, K. I. S.; Gribble, D. A.; Loo, W. S.; Tyagi, M.; Mullin, S. A.; Balsara, N. P. *Macromolecules* **2020**, *53*, 2406–2411, DOI: 10.1021/acs.macromol.0c00091.

[29] Mongcopa, K. I. S.; Tyagi, M.; Mailoa, J. P.; Samsonidze, G.; Kozinsky, B.; Mullin, S. A.; Gribble, D. A.; Watanabe, H.; Balsara, N. P. *ACS Macro Letters* **2018**, *7*, 504–508, DOI: 10.1021/acsmacrolett.8b00159.

[30] Ricarte, R. G.; Shanbhag, S. *Macromolecules* **2021**, *54*, 3304–3320, DOI: 10.1021/acs.macromol.0c02530.

[31] Xia, J.; Kalow, J. A.; Olvera De La Cruz, M. *Macromolecules* **2023**, *56*, 8080–8093, DOI: 10.1021/acs.macromol.3c01366.

[32] Hung, J.-H.; Mangalara, J. H.; Simmons, D. S. *Macromolecules* **2018**, *51*, 2887–2898, DOI: 10.1021/acs.macromol.8b00135.

[33] Adeyemi, O.; Zhu, S.; Xi, L. *Physics of Fluids* **2022**, *34*, 053107, DOI: 10.1063/5.0090540.

Chapter 5

MICRORHEOLOGICAL DUMBBELL PROBES IN SIMPLE AND COMPLEX FLUIDS

Nanoparticles and colloidal probes are widely used to infer the rheology of complex fluids and the transport properties of crowded biological environments. In these systems, the classical Stokes–Einstein–Sutherland relation, which connects diffusion to a single macroscopic viscosity, often exhibits systematic deviations. Such deviations arise because the probe experiences friction that depends on the ratio of its size to other characteristic length scales of the medium. This limitation has motivated theoretical descriptions of probe motion in terms of a wave-vector-dependent viscosity, $\eta(k)$, which characterizes the viscous response of the medium across different length scales. In this work, we investigate the diffusion of an anisotropic probe in both simple and polymeric fluids, using dissipative particle dynamics (DPD) simulations. The anisotropic probe is modeled as a rigid dumbbell with fixed bead separation, immersed in polymer solutions whose correlation length and macroscopic viscosity are set by the concentration and chain length. Using fluctuating hydrodynamics, we extract $\eta(k)$ from the transverse momentum autocorrelation function. We determine the total, parallel, and perpendicular diffusion coefficients of the dumbbell, D_d, $D_\parallel$, and $D_\perp$ from our simulations, and compare them with the theoretical predictions from a recently developed hydrodynamic theory for diffusion of anisotropic probes, which expresses the dumbbell mobility in terms of $\eta(k)$. We find that our simulation results are in good agreement with the theoretical mobilities, demonstrating that $\eta(k)$, rather than the macroscopic viscosity, captures the relevant length-scale dependence of the surrounding medium. Based on these results, we suggest a new approach to experimentally measure $\eta(k)$ using optical tweezers microrheology.

This chapter includes content from our previously published article:

[1] Tsamopoulos, A. J.; Makuch, K.; Wang, Z.-G. Microrheological Dumbbell Probes in Complex Fluids, *in preparation*, (2026).

5.1 Introduction

Understanding the transport of nanoparticle probes in complex fluids is of fundamental interest in soft condensed matter physics and in applications ranging from materials processing to cellular biology. Such complex media include the cytoplasm of living cells and crowded protein or DNA solutions, as well as polymer melts, polymer solutions, and cellulose–fiber suspensions [1]. Their structural heterogeneity, together with multiple intrinsic length and time scales, leads to rich and complex particle dynamics that in general cannot be described in terms of macroscopic rheology.

In simple liquids, the Stokes–Einstein–Sutherland (SES) equation relates the diffusivity of a spherical nanoparticle to the macroscopic shear viscosity of the solvent. In viscoelastic complex fluids, however, this relation often no longer holds; the effective diffusivity can deviate by orders of magnitude from SES predictions and becomes strongly dependent on the probe size and the microstructural organization of the surrounding medium [2–4]. Such deviations have been observed across neutral polymer and polyelectrolyte solutions, as well as unentangled and entangled polymer melts, where the presence of multiple intrinsic length and time scales fundamentally alters how momentum is transported to and from an embedded nanoparticle [3, 5, 6]. A central framework for predicting the linear viscoelastic response of complex fluids across timescales is the generalized Stokes–Einstein–Sutherland equation (GSES) introduced by Mason and Weitz, which infers the storage and loss moduli from the Laplace-transformed mean-squared displacement of a tracer particle [7]. While widely used, the GSES is not universally applicable; when the probe radius approaches structural length scales of the polymer network—such as the correlation length, radius of gyration, or entanglement tube diameter—it no longer senses a homogeneous continuum, and the inferred rheology becomes probe-size-dependent [4, 8, 9]. Experiments in entangled polymer solutions have shown that deviations from the GSE emerge sharply as the probe size becomes comparable to the tube diameter [8]. Studies of unentangled solutions and polyelectrolytes show analogous crossovers governed by the ratio of probe size to correlation length [4, 5]. Complementary scaling theories[4] and microscopic generalized-Langevin analyses[3] demonstrate how probe mobility transitions between regimes dominated by local blob-scale dynamics, entanglement constraints, and the terminal viscoelastic relaxation of the bulk.

Taken together, these findings show that agreement with the SES prediction is not

universal but emerges only when a clear separation of length scales is present. Probes far smaller than the mesh size experience only weak coupling to the macroscopic viscosity and may diffuse with an effective friction largely insensitive to polymer molecular weight [3, 4]. Conversely, sufficiently large probes—exceeding the correlation length, radius of gyration, or tube diameter—experience a continuum-scale hydrodynamic response of the medium and recover SES-like behavior governed by the bulk viscosity [3, 4]. In between these extremes, the friction is inherently scale-dependent, reflecting the hierarchical relaxation dynamics of the medium rather than a single macroscopic viscosity.

Makuch *et al.* [2] formulated a microscopic theory in which the viscous response of the medium is represented by a wave-vector-dependent viscosity, $\eta(k)$, capturing the influence of multiple characteristic length scales on the friction experienced by a probe. Using a generalized Smoluchowski description for Brownian dynamics, they derived a modified Stokes law that connects the hydrodynamic radius-dependent friction $\zeta_{\mathrm{tr}}(a)$ to the function $\eta(k)$. Combining this with the Einstein relation, $D_{tr} = k_{\mathrm{B}}T/\zeta_{tr}$, where $k_{\mathrm{B}}T$ is the thermal energy, provides a generalization of the SES that accounts for the relevant lengthscales of a complex fluid. Importantly, this generalized Stokes law is invertible, thus allowing to determine $\eta(k)$ from experimentally measured diffusivities of probes spanning multiple radii. By applying their framework to micellar solutions, polymer solutions, and intracellular environments, they demonstrated that a single function $\eta(k)$ quantitatively accounts for the pronounced departures from SES behavior and explains size-dependent diffusion.

While spherical probes are often used in microrheology, anisotropic particles are widespread in soft and biological matter [1]. Their Brownian motion samples distinct hydrodynamic environments along and perpendicular to their long axis, producing direction-dependent diffusion that is highly sensitive to local structure and mechanical constraints. Understanding this anisotropic transport is essential for interpreting the dynamics of actin filaments and cellulose fibers, and for guiding the design of synthetic rod-like viral carriers for drug delivery [10]. Continuum theories of rod-like diffusion, including the framework of Sokołowski *et al.* [11], treat the surrounding medium through an implicit, wave-vector-dependent viscosity $\eta(k)$. Such descriptions require $\eta(k)$ as an input, yet this quantity is rarely known a priori in polymer systems and is difficult to infer from experiments. Consequently, these analytical approaches cannot predict how chain dynamics regulate parallel and perpendicular mobilities in realistic environments.

To overcome these limitations, we employ dissipative particle dynamics (DPD) simulations of rigid dumbbells with tunable bead separation, immersed in simple liquids and in polymer solutions. DPD simulations enable us to determine the total, parallel, and perpendicular diffusion coefficients of the probe, D_d, $D_\parallel$, and $D_\perp$, while simultaneously extracting $\eta(k)$ from the transverse velocity autocorrelation function using fluctuating hydrodynamics. By comparing the simulated mobilities with the hydrodynamic theory of Makuch *et al.*, which expresses dumbbell motion solely in terms of $\eta(k)$, we demonstrate quantitative agreement between theory and simulations in polymeric environments. These results show that $\eta(k)$, rather than the macroscopic shear viscosity, captures the relevant length-scale dependence governing anisotropic drag. Lastly, we suggest that microrheology with optical tweezers could provide an experimental route to directly determine $\eta(k)$, without having to add any probes with varied hydrodynamic radius. Taken together, our findings suggest a unified description of anisotropic probe diffusion and hydrodynamic response in complex fluids, connecting molecular simulations with continuum theory.

5.2 Theory

We describe the anisotropic mobility of an oriented dumbbell in a complex fluid in terms of the wave-vector-dependent viscosity, $\eta(k)$ [2, 11]. This framework provides a direct connection between probe transport and the dissipation of transverse momentum across length scales, encoded in $\eta(k)$. Following Makuch *et al.*, we formulate the mobility problem using linear response theory and an effective hydrodynamic Green function that explicitly involves $\eta(k)$ [2]. In an incompressible, homogeneous, and isotropic fluid, the average velocity response at position $\mathbf{r}$ to a small point force $\mathbf{f}$ applied at position $\mathbf{r}_0$ can be written as:

$$\langle \mathbf{v}(\mathbf{r}) \rangle = \mathbf{G}_{\text{eff}}(\mathbf{R})\, \mathbf{f}, \qquad \mathbf{R} \equiv \mathbf{r} - \mathbf{r}_0, \tag{5.1}$$

where $\mathbf{G}_{\text{eff}}$ is the effective Green function. Within linear response, the corresponding Fourier-space Green function has the general form[2, 11]:

$$\hat{\mathbf{G}}_{\text{eff}}(\mathbf{k}) = \frac{1}{k^2 \eta(k)} \left(\mathbf{I} - \hat{\mathbf{k}}\hat{\mathbf{k}} \right), \tag{5.2}$$

which shows that the nonlocal viscous response is governed by $\eta(k)$. Guided by previous work, one can show that in the case of a dumbbell, the inverse Fourier transform of the Green function can be expressed in terms of two scalar functions:

$$\mathbf{G}_{\text{eff}}(\mathbf{R}) = \phi(R)\, \mathbf{I} + \psi(R) \left(\mathbf{I} - 3\hat{\mathbf{R}}\hat{\mathbf{R}} \right), \tag{5.3}$$

where $R = |\mathbf{R}|$ and $\hat{\mathbf{R}} = \mathbf{R}/R$. The scalar functions $\phi(R)$ and $\psi(R)$ are given by[2, 11]

$$\phi(R) = \frac{1}{3\pi^2} \int_0^\infty dk \, \frac{j_0(kR)}{\eta(k)}, \tag{5.4}$$

$$\psi(R) = -\frac{1}{6\pi^2} \int_0^\infty dk \, \frac{j_2(kR)}{\eta(k)}, \tag{5.5}$$

with $j_0(x)$ and $j_2(x)$ the spherical bessel functions defined as: $j_0(x) = \frac{\sin x}{x}$ and $j_2(x) = \left(\frac{3}{x^3} - \frac{1}{x}\right) \sin x - \frac{3}{x^2} \cos x$.

We model the probe as an oriented dumbbell composed of two identical spherical beads of hydrodynamic radius a, separated by $\mathbf{l}_d$ and constrained to maintain a fixed orientation. For a small total external force $\mathbf{F}_{\text{tot}}$ applied to the dumbbell, the center-of-mass velocity response takes the linear form

$$\mathbf{V} = \mathbf{M}(\mathbf{l}_d) \, \mathbf{F}_{\text{tot}}, \tag{5.6}$$

where $\mathbf{M}(\mathbf{l}_d)$ is the dumbbell mobility matrix. Since the surrounding medium is isotropic, $\mathbf{M}(\mathbf{l}_d)$ can be decomposed into components parallel and perpendicular to the dumbbell axis,

$$\mathbf{M}(\mathbf{l}_d) = \mu_{\parallel}(l_d) \, \hat{\mathbf{l}}_d \hat{\mathbf{l}}_d + \mu_{\perp}(l_d) \left(\mathbf{I} - \hat{\mathbf{l}}_d \hat{\mathbf{l}}_d \right). \tag{5.7}$$

We adopt the effective Green-function approximation introduced in Ref. [11]. In this approximation, the dominant hydrodynamic coupling between the two beads is captured by $\mathbf{G}_{\text{eff}}(\mathbf{l}_d)$, and the dumbbell mobility is written as

$$\mathbf{M}(\mathbf{l}_d) \approx \frac{1}{2} \mu_{\text{single}}(a) \, \mathbf{I} + \frac{1}{2} \mathbf{G}_{\text{eff}}(\mathbf{l}_d), \tag{5.8}$$

where $\mu_{\text{single}}(a)$ is the self-mobility of a single bead of hydrodynamic radius a in the same complex fluid. In our simulations the dumbbell beads are identical to the solvent particles. Therefore, the single-bead mobility follows directly from the solvent self-diffusivity via the Einstein relation, $\mu_{\text{single}}(a) = D_{\text{s}}/k_{\text{B}}T$, where D_{s} is the solvent self-diffusivity.

Substituting Eq. (5.3) into Eq. (5.8) and identifying coefficients in Eq. (5.7) yields explicit expressions for the parallel and perpendicular mobilities,

$$\mu_{\parallel}(l_d) = \frac{1}{2} \Big[\mu_{\text{single}}(a) + \phi(l_d) - 2\psi(l_d) \Big], \tag{5.9}$$

$$\mu_{\perp}(l_d) = \frac{1}{2} \Big[\mu_{\text{single}}(a) + \phi(l_d) + \psi(l_d) \Big]. \tag{5.10}$$

The anisotropy is controlled by $\psi(l_d)$ through

$$\mu_{\parallel}(l_d) - \mu_{\perp}(l_d) = -\frac{3}{2}\psi(l_d). \tag{5.11}$$

Finally, the diffusion coefficients follow from the Einstein relation,

$$D_{\parallel}(l_d) = k_{\mathrm{B}}T\,\mu_{\parallel}(l_d), \tag{5.12}$$

$$D_{\perp}(l_d) = k_{\mathrm{B}}T\,\mu_{\perp}(l_d). \tag{5.13}$$

5.3 Lengthscale Dependent Viscous Response

Non-local viscous response

At macroscopic length scales, Newton's law of viscosity provides a *local* constitutive relation between shear stress and strain rate. However, when the strain-rate field varies over molecular distances, the stress may not result from the strain rate at the same point [12]. This motivates a *non-local* constitutive law in which the shear stress is written as a spatial convolution of a viscosity kernel with the strain rate; in Fourier space this becomes a product involving the wavevector-dependent viscosity $\eta(k,\omega)$, which approaches the Newtonian viscosity as $k,\omega \to 0$ but becomes k-dependent at finite k [12, 13]. In Molecular Dynamics simulations, $\eta(k,\omega)$ can be determined from the transverse velocity autocorrelation function, $C_{uu}^{\perp}(\mathbf{k},t)$ [14]. To calculate, $C_{uu}^{\perp}(\mathbf{k},t)$, we consider the fluctuations of the streaming velocity field in Fourier space $\delta\tilde{\mathbf{u}}(\mathbf{k},t)$, evaluated from:

$$\delta\tilde{\mathbf{u}}(\mathbf{k},t) = \frac{1}{\rho_m}\sum_{i=1}^{N} m_i\,\mathbf{v}_i(t)\,e^{-i\mathbf{k}\cdot\mathbf{r}_i(t)}, \tag{5.14}$$

Here, ρ_m is the mass density, N is the total number of particles, m_i and $\mathbf{v}_i(t)$ are the mass and velocity of particle i, $\mathbf{r}_i(t)$ is its position, and $\mathbf{k}$ is the reciprocal-space wavevector. We note the mean streaming velocity vanishes in equilibrium. For a given wavevector $\mathbf{k}$, the transverse component $\delta\tilde{\mathbf{u}}_{\perp}$ is any Cartesian component orthogonal to $\mathbf{k}$ is given by:

$$\delta\tilde{\mathbf{u}}_{\perp}(\mathbf{k},t) = \frac{1}{\rho_m}\sum_{i} m\left[\mathbf{v}_i(t) - \left(\mathbf{v}_i(t)\cdot\hat{\mathbf{k}}\right)\hat{\mathbf{k}}\right]e^{-i\mathbf{k}\cdot\mathbf{r}_i(t)}, \tag{5.15}$$

where $\hat{\mathbf{k}} = \mathbf{k}/|\mathbf{k}|$ is the unit vector in the direction of $\mathbf{k}$. Then, the transverse velocity autocorrelation function is given by:

$$C_{uu}^{\perp}(\mathbf{k},t) = \frac{1}{V}\left\langle \delta\tilde{\mathbf{u}}_{\perp}(\mathbf{k},t)\cdot\delta\tilde{\mathbf{u}}_{\perp}(-\mathbf{k},0)\right\rangle, \tag{5.16}$$

and its Fourier–Laplace transform,

$$\widehat{C}^{\perp}_{uu}(\mathbf{k},\omega) = \int_0^\infty C^{\perp}_{uu}(\mathbf{k},t)\, e^{i\omega t}\, dt. \tag{5.17}$$

Then, the frequency and wavevector dependent shear viscosity is obtained by [15]:

$$\eta(k,\omega) = \frac{\rho_m}{k^2} \frac{C^{\perp}_{uu}(\mathbf{k},0) + i\omega\, \widehat{C}^{\perp}_{uu}(\mathbf{k},\omega)}{\widehat{C}^{\perp}_{uu}(\mathbf{k},\omega)}, \qquad (k \equiv |\mathbf{k}|) \tag{5.18}$$

In this work we focus on the zero-frequency viscosity at finite wavevector,

$$\eta(k) = \frac{\rho_m}{k^2} \frac{C^{\perp}_{uu}(\mathbf{k},0)}{\widehat{C}^{\perp}_{uu}(\mathbf{k},0)}. \tag{5.19}$$

Wavevectors are discrete under periodic boundary conditions,

$$k = \frac{2\pi n}{L}, \qquad n = 1, 2, \ldots, \tag{5.20}$$

where L is the length of the simulation box. In our work, we compute $C^{\perp}_{uu}(\mathbf{k},t)$ using the `Dynasor` package [16, 17].

Macroscopic viscosity η^0: Green–Kubo equation and optimal integration cutoff
The zero-wavevector viscosity η^0 is obtained from the Green–Kubo relation expressed in terms of the shear relaxation modulus $G(t)$,

$$\eta^0 = \int_0^\infty G(t)\, dt, \tag{5.21}$$

with $G(t)$ given by:

$$\begin{aligned} G(t) = \frac{V}{5k_\mathrm{B}T}\Big[&\langle\sigma_{xy}(t)\sigma_{xy}(0)\rangle + \langle\sigma_{yz}(t)\sigma_{yz}(0)\rangle \\ &+ \langle\sigma_{zx}(t)\sigma_{zx}(0)\rangle\Big] + \frac{V}{30k_\mathrm{B}T}\Big[\langle N_{xy}(t)N_{xy}(0)\rangle \\ &+ \langle N_{yz}(t)N_{yz}(0)\rangle + \langle N_{zx}(t)N_{zx}(0)\rangle\Big]. \end{aligned} \tag{5.22}$$

where $N_{\alpha\beta} \equiv \sigma_{\alpha\alpha} - \sigma_{\beta\beta}$. We use Eq. (5.22) in combination with the multitau correlator algorithm which substantially reduces statistical error [18].

A practical difficulty in Eq. (5.21) is that $G(t)$ typically exhibits a long-time tail with increasing statistical noise. To determine the integration cutoff without fitting $G(t)$ to an assumed analytic form [19] or imposing an arbitrary truncation time, we adopt

the statistical cutoff criterion of Liu *et al.* [20] We define the running Green–Kubo integral

$$\eta(t) \equiv \int_0^t G(\tau)\, d\tau. \tag{5.23}$$

At finite t, $\eta(t)$ suffers from two competing errors: (1) a *truncation bias* due to the missing long-time tail, $\int_t^\infty G(\tau)\, d\tau$, and (2) a *statistical error* due to noise in the measurement of $G(t)$. Assuming the noise in $G(t)$ has zero mean and is short-time correlated, one can minimize the mean-squared error of $\eta(t)$ with respect to t and obtain the following condition:

$$G(t^*)\big[\eta - \eta(t^*)\big] = \overline{\Delta G^2(t^*)}, \tag{5.24}$$

where $\overline{\Delta G^2(t)}$ denotes the variance of $G(t)$.

Because η is not known *a priori*, Eq. (5.24) is solved self-consistently. In practice, we compute:

$$E_1(t) = G(t)\big[\eta(t^*) - \eta(t)\big], \qquad E_2(t) = \overline{\Delta G^2(t)}. \tag{5.25}$$

To determine t^*, we start from a large initial guess for the cutoff t_0^* and evaluate $E_1(t)$ using $\eta(t_0^*)$. The updated cutoff t_1^* is then defined as the time at which $E_1(t) = E_2(t)$. Using t_1^*, we recompute $E_1(t)$ and $\eta(t_1^*)$, and obtain a new intersection time t_2^*. We repeat this procedure until t_n^* converges; the final viscosity is reported as $\eta^0 = \eta(t^*)$.

5.4 Simulation Method

All simulations are performed using the LAMMPS molecular dynamics package [21, 22], with GPU acceleration [23, 24]. We employ dissipative particle dynamics (DPD) [25] simulations, which use a Galilean-invariant, momentum-conserving thermostat and therefore capture hydrodynamic interactions [14, 26, 27]. All bead types have identical mass m and interact within a cutoff distance r_c, which define the natural units of mass and length, respectively. The energy scale is set to, $k_\mathrm{B}T$, which defines the characteristic time scale $\tau = \sqrt{mr_c^2/k_\mathrm{B}T}$.

In DPD simulations, a bead i interacts with neighboring beads j within $r_{ij} < r_c$ via the sum of conservative, dissipative, and random pair forces,

$$\mathbf{f}_i = \sum_{j \neq i} \left(\mathbf{F}_{ij}^\mathrm{C} + \mathbf{F}_{ij}^\mathrm{D} + \mathbf{F}_{ij}^\mathrm{R} \right), \tag{5.26}$$

where $\mathbf{r}_{ij} = \mathbf{r}_i - \mathbf{r}_j$, and $r_{ij} = |\mathbf{r}_{ij}|$. The conservative repulsive force is

$$\mathbf{F}_{ij}^\mathrm{C} = a_{ij} \left(1 - \frac{r_{ij}}{r_c} \right) \mathbf{e}_{ij}, \tag{5.27}$$

with $\mathbf{e}_{ij} = \mathbf{r}_{ij}/r_{ij}$ and $a_{ij} = 25\, k_{\mathrm{B}}T/r_c$ for all bead pairs. The dissipative and random forces take the standard form

$$\mathbf{F}_{ij}^{\mathrm{D}} = -\gamma\, w^{\mathrm{D}}(r_{ij})\, \left(\mathbf{v}_{ij} \cdot \mathbf{e}_{ij}\right) \mathbf{e}_{ij}, \tag{5.28}$$

$$\mathbf{F}_{ij}^{\mathrm{R}} = \sigma\, w^{\mathrm{R}}(r_{ij})\, \xi_{ij}\, \mathbf{e}_{ij}, \tag{5.29}$$

where $\mathbf{v}_{ij} = \mathbf{v}_i - \mathbf{v}_j$, ξ_{ij} is a symmetric Gaussian random variable with zero mean and unit variance, and the weight functions are

$$w^{\mathrm{R}}(r) = \left(1 - \frac{r}{r_c}\right), \qquad w^{\mathrm{D}}(r) = \left[w^{\mathrm{R}}(r)\right]^2. \tag{5.30}$$

Following the standard DPD convention, the friction coefficient is set to $\gamma = 4.5$, and the fluctuation–dissipation relation $\sigma^2 = 2\gamma k_{\mathrm{B}}T$ fixes $\sigma = 3$ in our reduced units.

To account for the polymer chain connectivity, bonded polymeric beads are connected by harmonic bonds,

$$U_{\mathrm{bond}}(r) = \frac{1}{2} K_{\mathrm{bond}}\, (r - r_0)^2, \tag{5.31}$$

with $K_{\mathrm{bond}} = 128\, k_{\mathrm{B}}T/r_c^2$ and $r_0 = 0.7\, r_c$.

The total number density is fixed at the standard DPD value $\rho = 3\, r_c^{-3}$. All simulation boxes are cubic with periodic boundary conditions. In all cases, the total number of beads is fixed at $N_{\mathrm{tot}} = 81,000$, corresponding to $V = 27,000\, r_c^3$ and a box length $L = 30\, r_c$. Polymer solutions are prepared at polymer volume fractions $\phi_P = 0, 0.3, 0.5$, where $\phi_P = 0$ corresponds to a pure DPD solvent. At fixed ϕ_P, the number of chains is adjusted to maintain ϕ_P as N varies. We consider $N = 10 - 200$.

We perform two types of simulations. First, polymer solutions without dumbbells are used to compute the wave-vector-dependent viscosity $\eta(k)$. Second, dumbbells dispersed in polymer solutions are used to compute the dumbbell diffusion coefficients. Each dumbbell simulation is paired with a corresponding polymer-solution-only simulation at the same (ϕ_P, N), obtained by replacing dumbbell beads with solvent beads while keeping N_{tot} and ρ fixed.

The dumbbell probes consist of two identical beads held at a fixed bead separation $l_d = 1, 2, 4, 6, 8$ (in units of r_c). Each simulation contains 100 dumbbells (200 beads), corresponding to a number density $n_d \approx 0.007$. Rigid-body dynamics are integrated using `fix rigid/nve` in LAMMPS [28], with rotational motion

suppressed. All dumbbells are initialized to be aligned with the x-axis and remain at fixed orientation throughout the simulation. We confirm that keeping the orientation fixed does not introduce any artifacts by conducting simulations where the dumbbell can freely rotate (see Appendix).

Initial configurations are generated by randomly placing solvent beads and polymer chains in the simulation box (with chain conformations constructed via a random-walk procedure). Dynamics are integrated with a time step of $\Delta t = 0.02\,\tau$. Each system is equilibrated for 5×10^6 steps, followed by a production run of 5×10^7 to 10^8 steps. At least four independent replicas are used to estimate uncertainties.

5.5 Results and Discussion

Anisotropic Probe Dynamics

We begin by investigating how polymer concentration and chain length affect the friction on a probe embedded in a polymer solution. This friction inherently depends on multiple length scales of the system, therefore, we first determine the zero-frequency wave-vector-dependent viscosity, $\eta(k)$, which characterizes the scale dependence of momentum dissipation and resulting friction. For $k > 0$, we obtain $\eta(k)$ from the transverse velocity autocorrelation function, $C^{\perp}_{uu}$ (eq. (5.19)), while for $k = 0$, we compute $\eta(0) \equiv \eta^0$ from the Green–Kubo relation (eq. (5.21)). In Fig. 5.1(a), we show $\eta(k)$ for the solvent ($\phi_P = 0$). The Newtonian shear viscosity of the solvent is $\eta^0 \approx 0.8\, k_B T\tau / r_c^3$. Self-diffusivity of the solvent molecule obtained from the mean square displacement is equal to $D_s = 0.301 r_c^2/\tau$, which gives the hydrodynamic radius of the solvent molecule equal to $a_s = k_B T/6\pi\eta_0 D_s \approx 0.22 r_c$.

In Fig. 5.1(a), we also show $\eta(k)$ for polymer solutions at fixed chain length $N = 50$ and polymer volume fractions $\phi_P = 0.3$ and $\phi_P = 0.50$. For comparison, we also show $\eta(k)$ for a simple liquid, which consists solely of non-bonded monomeric beads. For the simple liquid, $\eta(k)$ depends only weakly on k [14], indicating that nonlocal corrections to the viscous response are negligible over the wavevector range probed and that the stress is described by a local, Newtonian constitutive relation [12, 13].

In contrast, polymer solutions exhibit a pronounced enhancement of $\eta(k)$ at small k [29]. As k increases, $\eta(k)$ decreases and approaches the solvent value, consistent with the recovery of a local, solvent-like response on sufficiently small length scales. The magnitude of the low-k enhancement increases with polymer volume fraction. A natural interpretation is in terms of the polymer correlation length ξ, which

decreases with ϕ_P as $\xi \simeq b\,\phi_P^{-0.76}$ in a good solvent [4]. It is convenient to associate each wave vector with a real-space probe length scale $d \simeq 2\pi/k$. When $d \ll \xi$ (equivalently $k\xi \gg 1$), the probe samples the fluid within a single correlation volume and the viscous response is predominantly solvent-like. Conversely, when $d \gtrsim \xi$ (i.e., $k\xi \lesssim 1$), the probe motion spans many correlation volumes and polymer segments must relax to accommodate momentum dissipation, leading to an increased effective viscous response.

In this regime, Cai *et al.* [4] found that the effective friction (or $\eta(k)$ in our work) of a probe of size d scales as $\eta_{\text{eff}} \sim \eta_s(d/\xi)^2$, where η_s is the solvent viscosity. This implies that polymer contributions become increasingly important as k decreases below $O(1/\xi)$, producing the observed rise of $\eta(k)$ as k approaches 0. Moreover, because ξ decreases with increasing ϕ_P, the crossover shifts to larger k and the low-k enhancement strengthens with polymer concentration, consistent with Fig. 5.1(a). Overall, the data reveal a clear separation between polymer-controlled momentum dissipation at small k (large d) and a solvent-like viscous response at large k (small d) [30].

Having established the effect of polymer concentration, we next examine the role of chain length, N, at fixed polymer volume fraction. Figure 5.1(b) shows $\eta(k)$ at $\phi_P = 0.33$ for several N. At small k, $\eta(k)$ increases systematically with increasing N, consistent with the Rouse model. Longer chains contribute more strongly to large-scale momentum dissipation. As k increases, this chain-length dependence weakens continuously and vanishes once the probed length scale becomes smaller than the correlation length, $d \simeq 2\pi/k \lesssim \xi$ (or $k \gtrsim \xi^{-1}$), beyond which all curves collapse. This behavior is expected in the semidilute regime, where ξ is controlled by ϕ_P and is independent of N; consequently, the crossover to the local, solvent-like response occurs at a common wave vector for all sufficiently long chains [14, 30]. A small deviation from this collapse is visible for $N = 10$, which we attribute to the fact that this chain length does not reach the overlap concentration at $\phi_P = 0.3$ and therefore does not lie in the semidilute regime (see Appendix). By contrast, $N = 20$ is close to the overlap condition at this concentration, with $\phi_P/\phi_P^* \approx 1$, and already exhibits the semidilute-like crossover. Overall, the results show that chain connectivity enhances $\eta(k)$ only on the largest length scales (small k), while the short-wavelength response recovers a local, solvent-like dissipation that is largely insensitive to N [14, 30].

Next, we quantify the dumbbell translational diffusivity and its dependence on the

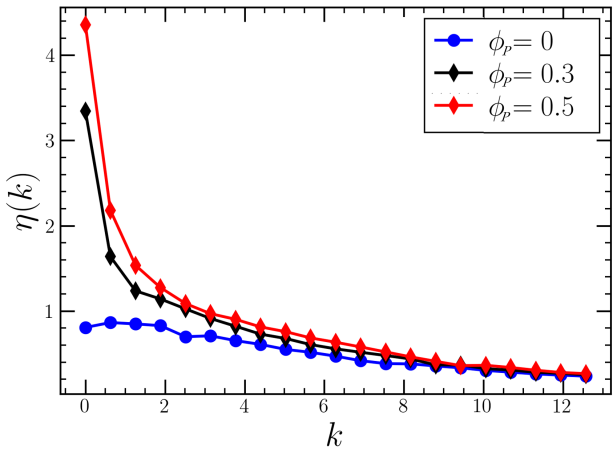

(a)

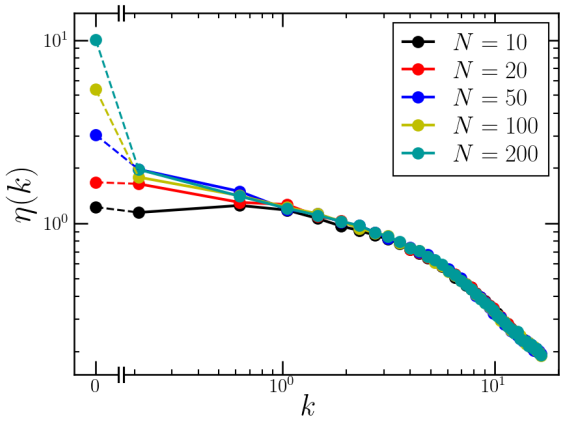

(b)

Figure 5.1: Wave-vector-dependent viscosity $\eta(k)$. (a) Fixed chain length $N = 50$, varying polymer volume fraction, ϕ_P. (b) Fixed polymer volume fraction, $\phi_P = 0.3$, varying chain length, N.

separation distance between the two beads of a dumbbell, l_d. The diffusivity is determined by:

$$D_d = \lim_{t\to\infty} \frac{\left\langle \Delta \boldsymbol{R}_d(t)^2 \right\rangle}{6t}, \tag{5.32}$$

where $\left\langle \Delta \boldsymbol{R}_d(t)^2 \right\rangle$ is the mean-square displacement (MSD) of the dumbbell center-of-mass over time t.

To characterize anisotropic motion, we further decompose the diffusivity into components parallel and perpendicular to the dumbbell axis, $\hat{\boldsymbol{l}}_d$. These are given by:

$$D_{\parallel} = \lim_{t\to\infty} \frac{\left\langle \Delta \boldsymbol{R}_{\parallel}(t)^2 \right\rangle}{2t}, \tag{5.33}$$

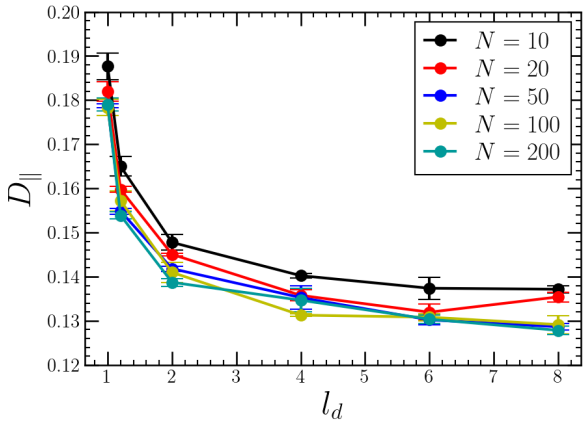

(a)

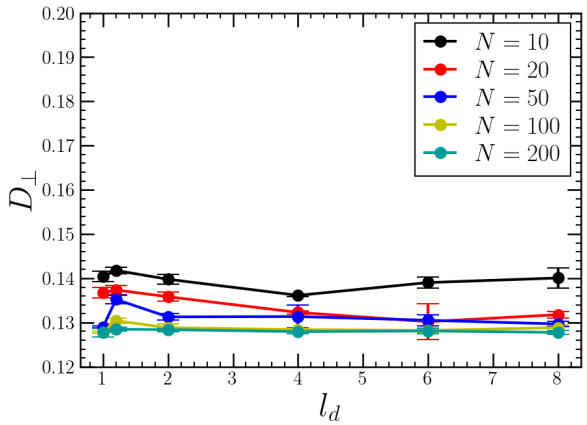

(b)

Figure 5.2: Diffusion coefficients as a function of dumbbell length l_d. (a) Parallel diffusion coefficient $D_\parallel$. (b) Perpendicular diffusion coefficient $D_\perp$. Results are shown at fixed polymer volume fraction $\phi_P = 0.3$ for several chain lengths N.

$$D_\perp = \lim_{t\to\infty} \frac{\left\langle \Delta \boldsymbol{R}_\perp(t)^2 \right\rangle}{4t}, \tag{5.34}$$

with $\Delta R_\parallel(t) \equiv \Delta \boldsymbol{R}_d(t) \cdot \hat{\boldsymbol{l}}_d$ and $\Delta \boldsymbol{R}_\perp(t) \equiv \Delta \boldsymbol{R}_d(t) - \Delta R_\parallel(t)\, \hat{\boldsymbol{l}}_d$.

In Fig. 5.2, we plot the diffusivity components as a function of l_d for polymer solutions at fixed volume fraction $\phi_P = 0.3$ and several chain lengths N. Figure 5.2(a) shows that the parallel diffusivity $D_\parallel$ decreases markedly as l_d increases and then approaches a plateau for larger separations. Over most of the l_d range, the N-dependence of $D_\parallel$ is modest, with the curves for different N largely collapsing within uncertainty at the largest l_d values. This weak N-dependence is attributed to the correlation length being independent of N. In Fig. 5.2(b), the perpendicular

diffusivity $D_\perp$ is essentially independent of l_d and, as in the parallel case, shows only a weak dependence on N. Comparing Figs. 5.2(a) and 5.2(b), we find $D_\parallel > D_\perp$ for $l_d < 8$, with the anisotropy diminishing as l_d increases, primarily due to the decrease in $D_\parallel$. At $l_d = 8$, the diffusion becomes essentially isotropic.

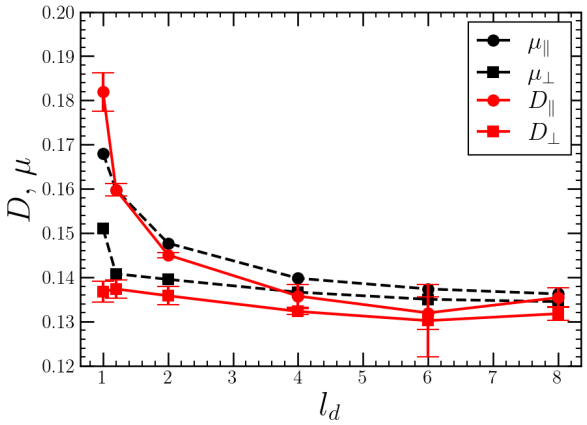

(a)

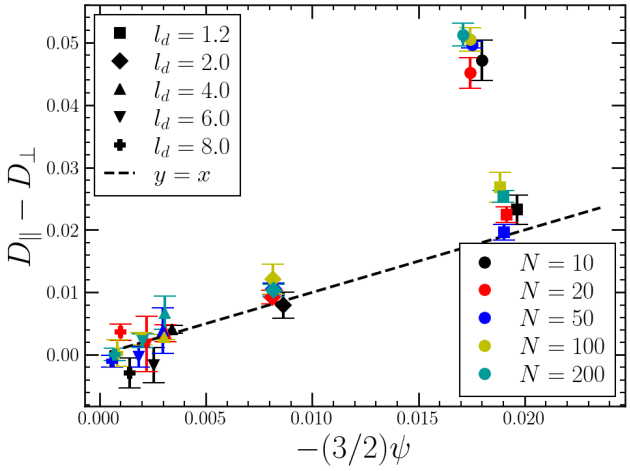

(b)

Figure 5.3: Comparison of dumbbell anisotropic diffusivity from simulation with predictions based on $\eta(k)$. (a) Parallel and perpendicular mobilities, $\mu_\parallel$ and $\mu_\perp$, together with the directly measured long-time diffusion coefficients, $D_\parallel$ and $D_\perp$, as functions of bead separation, l_d, for $N = 50$ and $\phi_P = 0.3$. (b) Difference of the long-time diffusion coefficients, $D_\parallel - D_\perp$, plotted against $-(3/2)\,\psi(l_d)$ for several bead separations l_d and chain lengths N.

To rationalize the behavior of the diffusivity, we apply the theoretical framework outlined in Sec. 5.2, which connects the anisotropic dumbbell mobility to the wave-vector-dependent viscosity $\eta(k)$. We therefore examine whether this viscosity function alone can predict the anisotropic dumbbell dynamics. Specifically, using

$\eta(k)$ extracted from simulations of polymer solutions without addition of dumbbells, we compute the scalar coefficients of the effective Green function—the isotropic coefficient $\phi(l_d)$ and the anisotropic coefficient $\psi(l_d)$—from Eqs. (5.4)–(5.5). These two functions encode the isotropic and anisotropic components of hydrodynamic coupling at bead separation l_d, and thereby determine the parallel and perpendicular mobilities through Eqs. (5.9) and (5.10).

Figure 5.3(a) compares the directly measured diffusion coefficients, $D_\parallel$ and $D_\perp$, with the corresponding theoretical mobility predictions obtained from $\eta(k)$, for $N = 50$ and $\phi_P = 0.3$. We note that we have chosen $k_\mathrm{B}T = 1$, thus diffusivities and mobilities are essentially the same. Across the range of bead separations considered, the theory reproduces the weak l_d-dependence of $D_\perp$ as well as the more pronounced decrease of $D_\parallel$ with increasing l_d. Extending this comparison beyond a single chain length, we next examine whether the same agreement holds across all chain lengths, N, and bead separations, l_d. Figure 5.3(b) focuses on the diffusion anisotropy, $D_\parallel - D_\perp$, and compares it to the anisotropic contribution of the effective Green function, $\psi(l_d)$, which is directly related to the mobility difference through Eq. (5.11). In our reduced units with $k_\mathrm{B}T = 1$, Eqs. (5.11) and (5.12)-(5.13) imply that $D_\parallel - D_\perp = -(3/2)\,\psi$. Remarkably, data spanning multiple chain lengths N and bead separations l_d collapse onto the $y = x$ line, indicating that the diffusion anisotropy consistently decreases with increasing l_d. At small l_d, there is a hydrodynamic coupling between the dumbbell beads; the motion of one bead creates a velocity gradient in the surrounding fluid, which makes the other sphere act like a forced dipole (stresslet). At large l_d, this hydrodynamic coupling weakens. We can also understand this from the definition of ψ, which quantifies the diffusion anisotropy; first, for a simple liquid, assuming that $\eta(k)$ is a weak function of k, then

$$\psi(l_d) = -\frac{1}{6\pi^2}\int_0^\infty \frac{j_2(kl_d)}{\eta_0}\,dk \tag{5.35}$$

Therefore,

$$\psi(l_d) = -\frac{1}{24\pi\eta_0\, l_d}. \tag{5.36}$$

which has consistent scaling with previous work for simple liquids [31]. Overall, these results suggest that the anisotropic Green-function coefficient $\psi(l_d)$ extracted from $\eta(k)$ quantitatively accounts for the observed diffusion anisotropy.

We find a small deviation between DPD simulations and theoretical predictions for $l_d = 1$. Figure 5.3(a) shows that for the shortest dumbbell, $l_d = 1$, the anisotropy between the parallel and perpendicular diffusivities predicted by the theory does

not quantitatively match the DPD simulations. Specifically, the theoretical values (black symbols) at $l_d = 1$ lie clearly between the simulation data (red symbols), indicating that the theory underestimates the asymmetry. For such a small bead separation, deviations are expected for at least two reasons: (i) higher-order hydrodynamic interactions beyond the leading far-field (Oseen-type) description, and (ii) a breakdown of a homogeneous-solvent hydrodynamic picture caused by depletion of solvent particles between the beads, i.e., by the inhomogeneous solvent structure around the dumbbell.

Insight into the first mechanism can be gained by recalling the Rotne–Prager correction to the Oseen tensor. In a simple Newtonian fluid governed by the Stokes equations, inclusion of Rotne–Prager terms (as the next hydrodynamic order in a^2/l_d^2) reduces the predicted anisotropy as the dumbbell length decreases. If the same qualitative trend persists in a complex fluid, then higher-order hydrodynamic interactions alone would further decrease the anisotropy and therefore cannot explain the larger asymmetry observed in the simulations at $l_d = 1$.

To rationalize the second mechanism, note that $l_d = 1$ corresponds to $l_d = r_c$, i.e., the beads are separated by approximately the cutoff distance and are thus at the edge of their mutual interaction range. In this regime, our DPD simulations indicate that solvent particles are effectively depleted from the region between the two beads. This motivates considering an even closer limit, $l_d \to 0$ (or formally $l_d = 0$), where the dumbbell becomes an effective "bead-on-bead" object, i.e., a composite particle that behaves similarly to a single bead. In DPD, such a composite object would in principle differ from a solvent bead because it presents a stronger repulsion to the surrounding solvent and therefore may have a somewhat larger hydrodynamic radius. Neglecting this complication and assuming the same hydrodynamic radius as for a single bead, the Einstein relation $D = k_B T\,\mu$ implies that a bead-on-bead object has approximately twice the mobility (and thus twice the diffusivity) compared to a dumbbell at large separation $l_d \to \infty$. Applying this estimate to Fig. 5.2(a) where the large-separation diffusivity is $D_\parallel(l_d = 8) \approx 0.13\, r_c^2/\tau$, we expect

$$D_\parallel(l_d = 0) \simeq 2D_\parallel(l_d = 8) \approx 0.26\, r_c^2/\tau, \tag{5.37}$$

which is consistent with the observed increase of the parallel diffusivity for short dumbbells in Fig. 5.2(a) and 5.3(a).

Figure 5.4(a) presents the total dumbbell diffusivity $D = (D_\parallel + 2D_\perp)/3$ at $\phi_P = 0.3$ as a function of bead separation l_d for several chain lengths N. For all N, D initially

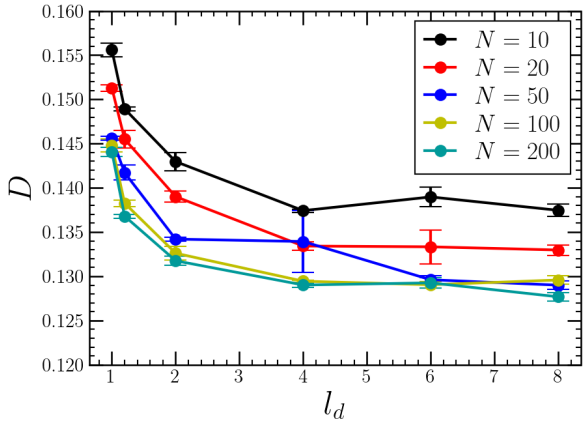

(a)

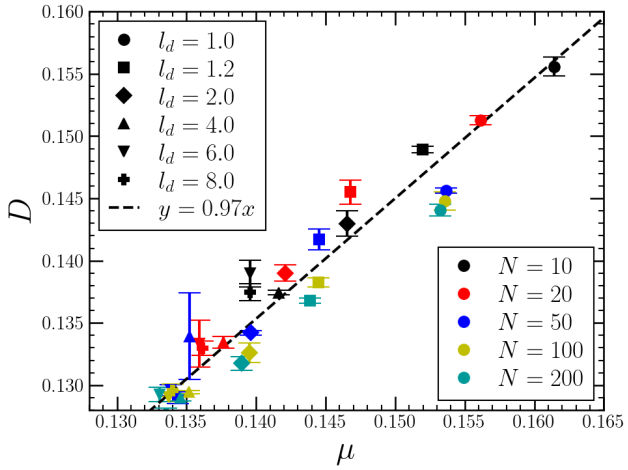

(b)

Figure 5.4: Comparison of the total dumbbell diffusivity $D = (D_{\parallel} + 2D_{\perp})/3$ with theoretical prediction. (a) D as a function of bead separation, l_d, for polymer solutions at volume fraction $\phi_P = 0.3$ and several chain lengths, N. (b) D plotted against the theoretical mobility prediction μ, computed from $\eta(k)$.

decreases with increasing l_d and then approaches a plateau at larger separations. At fixed l_d, increasing N also leads to a modest reduction of D, consistent with progressively slower transport in polymer solutions with longer chain lengths.

Figure 5.4(b) compares D to the theoretical prediction obtained from the mobility $\mu = (\mu_{\parallel} + 2\mu_{\perp})/3$ computed using $\eta(k)$ extracted from dumbbell-free simulations. Data for multiple chain lengths and bead separations fall close to a unit-slope relation, indicating that the framework captures both the magnitude and the systematic variations of D across N and l_d. The near-collapse of points associated with different l_d further supports that the same $\eta(k)$-based description consistently accounts for the isotropic diffusivity over the range of separations considered.

Extracting $\eta(k)$ from dumbbell microrheology

The wave-vector-dependent viscosity $\eta(k)$ is a central material function: it governs transverse momentum transport across length scales and, through the effective Green function, determines the mobility of immersed probes [2, 11]. Once $\eta(k)$ is known, the same framework can be used, in principle, to predict the dynamics of a broad class of colloidal particles in complex fluids, where a single macroscopic viscosity cannot describe the viscous response and the classic SES equation fails [3].

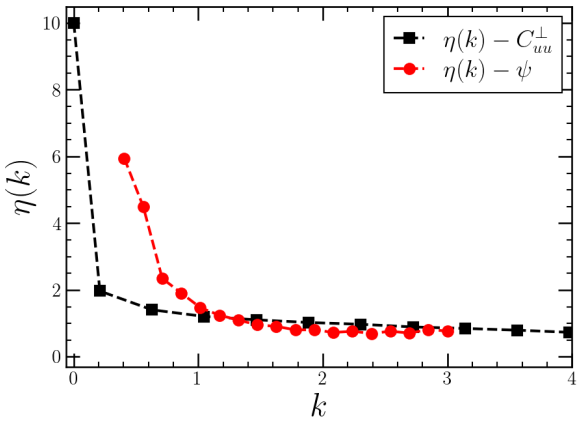

Figure 5.5: Comparison of the wave-vector-dependent viscosity, $\eta(k)$, for $N = 200$ and $\phi_P = 0.3$, obtained from the transverse velocity autocorrelation function ($C_{uu}^{\perp}$) and from Eq. (5.41), using $\psi = -(2/3)(D_{\parallel} - D_{\perp})$.

Motivated by this, we propose an experimental route to determine $\eta(k)$ using microrheology with dumbbell probes. In a dual optical tweezers setup, two beads are held at a fixed separation l_d while small forces are applied to measure the mobility response, yielding $\mu_{\parallel}(l_d)$ and $\mu_{\perp}(l_d)$. The mobility anisotropy directly determines

the anisotropic kernel of the effective Green function,

$$\mu_{\parallel}(l_d) - \mu_{\perp}(l_d) = -\frac{3}{2}\,\psi(l_d), \tag{5.38}$$

and therefore provides $\psi(l_d)$ as an experimentally accessible quantity. Varying l_d within the same setup then replaces the need to repeat measurements for multiple probe radii.

To connect $\psi(l_d)$ to $\eta(k)$, we start from its definition,

$$\psi(l_d) = -\frac{1}{6\pi^2}\int_0^\infty dk\,\frac{j_2(kl_d)}{\eta(k)}. \tag{5.39}$$

Multiplying both sides by $l_d^2 j_2(kl_d)$ and integrating over l_d gives an integral equation that can be inverted using the spherical–Bessel orthogonality identity,

$$\int_0^\infty dl_d\, l_d^2\, j_2(kl_d)\, j_2(k'l_d) = \frac{\pi}{2k^2}\,\delta(k-k'). \tag{5.40}$$

This yields the following relation:

$$\eta(k) = -\frac{1}{12\pi k^2}\left[\int_0^\infty dl_d\, l_d^2\, j_2(kl_d)\,\psi(l_d)\right]^{-1}. \tag{5.41}$$

Equations (5.38)–(5.41) thus provide a direct route from a dumbbell mobility measurement at varying separations l_d to the full viscosity function $\eta(k)$. We apply this procedure in our simulation by computing $\psi(l_d)$ from the measured diffusivity anisotropy and reconstructing $\eta(k)$ via Eq. (5.41). Figure 5.5 compares the resulting $\eta(k)$ extracted from the transverse momentum autocorrelation function $C_{uu}^{\perp}(k,t)$ and from $\psi(l_d)$ (Eq. (5.41)). We find good agreement between the η_ψ and η, indicating that the anisotropic Green-function kernel provides a practical route to access $\eta(k)$. However this agreement is limited by the chosen separation distances utilized in our work, and more importantly by the deviation at $l_d = 1$, which does not allow us to probe higher k values.

5.6 Conclusions

We used dissipative particle dynamics simulations to study the translational dynamics of rigid dumbbell probes in a simple DPD solvent and in polymer solutions, where probe friction depends on the interplay between probe anisotropy and the intrinsic length scales of the medium. To quantify this scale dependence, we extracted the zero-frequency wave-vector-dependent viscosity $\eta(k)$ from the transverse velocity autocorrelation function and used it as the sole input to a recently

developed hydrodynamic theory for anisotropic probes. The resulting predictions reproduce both the magnitude and the systematic trends of the dumbbell diffusion coefficients over bead separations and polymer chain lengths, including the distinct behaviors of $D_{\parallel}$ and $D_{\perp}$ and the collapse of the diffusion anisotropy $D_{\parallel} - D_{\perp}$ onto the theoretical relation set by the anisotropic kernel $\psi(l_d)$. Together, these results demonstrate that $\eta(k)$—rather than a single macroscopic viscosity—captures the relevant length-scale dependence governing anisotropic drag in polymeric liquids.

Motivated by these findings, we proposed a dumbbell microrheology protocol to experimentally access $\eta(k)$ using dual optical tweezers. By measuring the mobility anisotropy as a function of bead separation, one can directly obtain $\psi(l_d)$ and invert the corresponding spherical-Bessel integral relation to reconstruct $\eta(k)$, thereby replacing the need for multiple probe sizes with a single tunable dumbbell geometry [2]. Applying this inversion within our simulations provides good agreement between $\eta(k)$ obtained independently from transverse velocity fluctuations and $\eta(k)$ from the diffusion anisotropy (l_d), thereby supporting the feasibility of the approach. More broadly, our work provides a unified connection between anisotropic probe transport and generalized hydrodynamic response in complex fluids, bridging molecular simulations, continuum theory, and experimentally accessible microrheological observables.

5.7 Appendix

Stress relaxation and accurate estimation of η^0

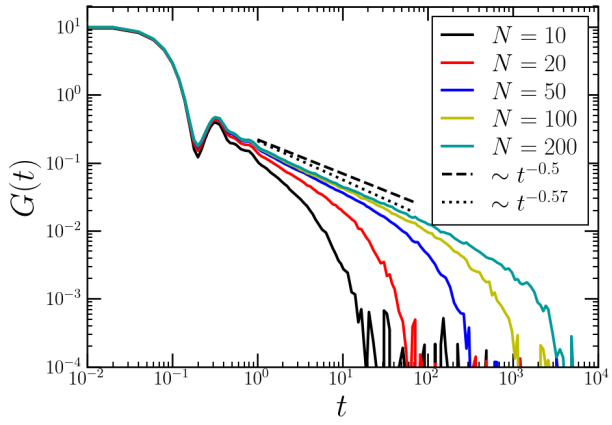

Figure 5.6: Shear stress relaxation modulus $G(t)$, for various chain lengths, N, and $\phi = 0.3$. The power law decay at intermediate times resembles more the Zimm prediction ($t^{-0.57}$) than the Rouse prediction ($t^{-0.5}$).

The accurate numerical evaluation of the Green–Kubo integral is limited by a signal-to-noise tradeoff in $G(t)$: early-time data exhibit a high signal with small variance, whereas late-time data exhibit diminished signal and substantially increased noise. Consequently, truncating the integral too early biases the viscosity, while extending it too long inflates the variance and can destabilize the estimate. Common remedies, such as empirical tail fitting or an imposed cutoff time, reduce noise but introduce model dependence. In our work, we adopt the algorithm of Liu et al. [20], which determines the cutoff time that best balances late-time noise against early-time truncation bias.

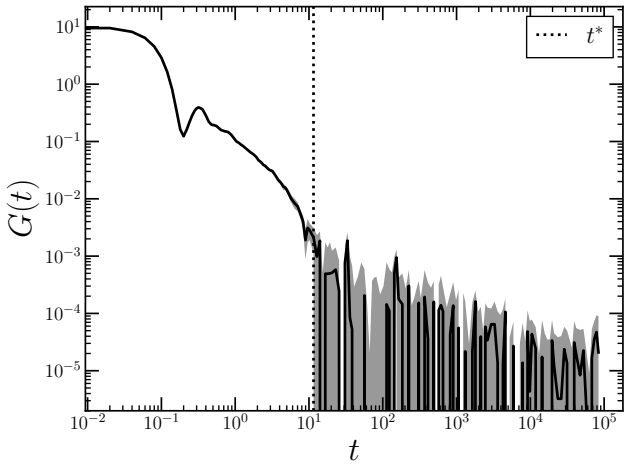

Figure 5.7: $G(t)$ for $N = 10$ and $\phi = 0.3$, together with its standard deviation determined from 10 independent runs. Early times are characterized by high signal and low noise, while later times by low signal and high noise. $t*$ denotes the cutoff time, where the systematic truncation error of the Green–Kubo integral (tail contribution) becomes equal to the statistical noise in the stress relaxation modulus ($E1 = E2$). This corresponds to the minimum total mean-square error in the viscosity estimate.

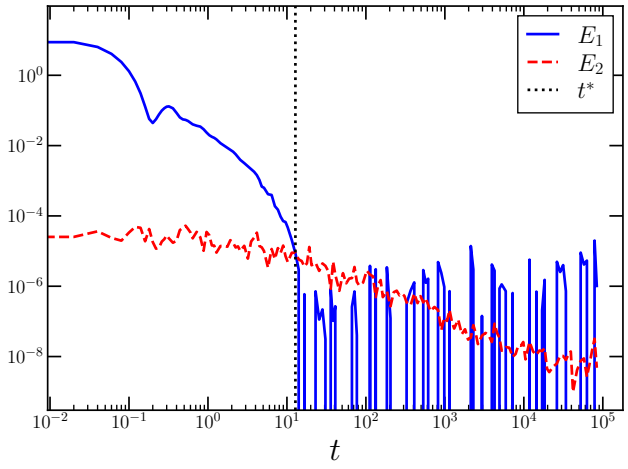

Figure 5.8: E_1 and E_2 determined by 10 independent runs. Their intersection denotes the cutoff time for the Green–Kubo integral. To get better statistics, we repeat this procedure 5 times (50 independent runs in total).

Transverse velocity autocorrelation functions

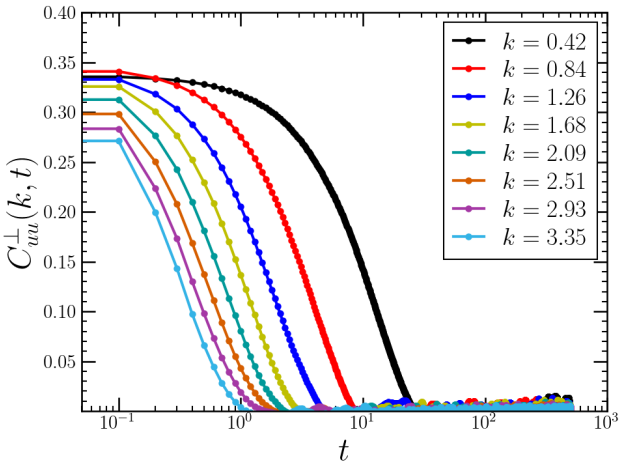

Figure 5.9: Transverse velocity correlation functions, $C^{\perp}_{uu}(k,t)$, for $N = 50$ at $\phi_P = 0.3$.

Dumbbell Diffusion with free and fixed rotation

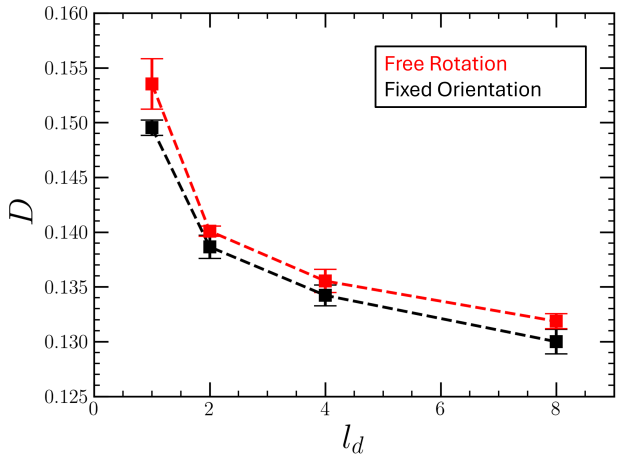

Figure 5.10: Comparison of dumbbell diffusion for fixed orientation and freely rotating dumbbells. We find good agreement between the two methods for all l_d.

Polymer Volume Fraction and Overlap concentration

The polymer volume fraction is defined as

$$\phi_P = \frac{V_{\text{poly}}}{V_{\text{tot}}} \tag{5.42}$$

The overlap concentration occurs when

$$V_{\text{tot}} \approx n\frac{4}{3}\pi R_g^3 = V_{\text{per}} \tag{5.43}$$

Thus

$$\phi_P{}^* = \frac{V_{\text{poly}}}{V_{\text{per}}} = \frac{v_0 nN}{n\frac{4}{3}\pi R_g^3} \tag{5.44}$$

For good solvent conditions

$$R_g = \frac{1}{\sqrt{6}}\, b_0\, N^{3/5} \tag{5.45}$$

Substituting into the expression for $\phi_P{}^*$,

$$\phi_P{}^* = 3.5\, N^{-4/5} \tag{5.46}$$

In Figure 5.11a, we show the dependence of the overlap concentration $\phi_P{}^*$ on chain length N, which follows the expected scaling $\phi_P{}^* \sim N^{-4/5}$. For comparison, several fixed volume fractions ϕ_P are also plotted. We quantify the *effective* concentration

regime in Figure 5.11b, where we present the normalized ratio $\phi_P/\phi_P{}^*$, which increases with N.

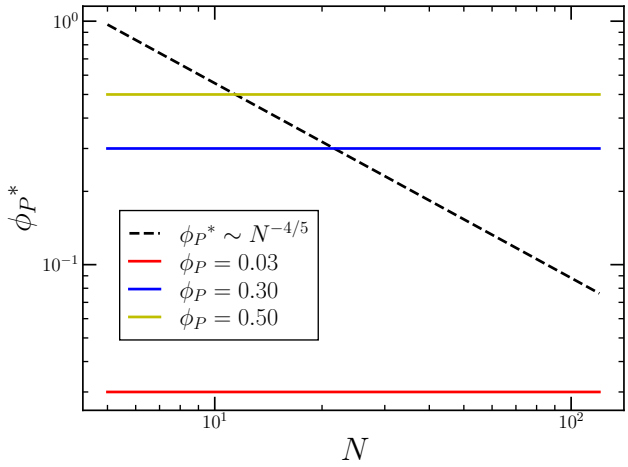

(a)

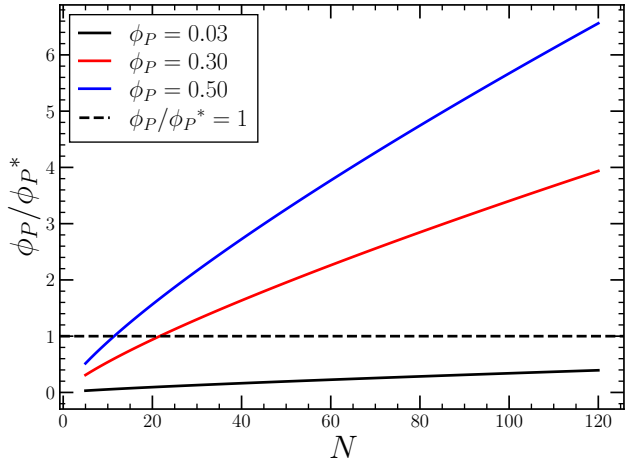

(b)

Figure 5.11: (a) Volume fraction and overlap concentration as a function of chain length and (b) volume fraction normalized by the overlap concentration as a function of chain length.

References

[1] Habibi, Y.; Lucia, L. A.; Rojas, O. J. *Chemical Reviews* **2010**, *110*, 3479–3500, DOI: 10.1021/cr900339w.

[2] Makuch, K.; Hołyst, R.; Kalwarczyk, T.; Garstecki, P.; Brady, J. F. *Soft Matter* **2020**, *16*, 114–124, DOI: 10.1039/C9SM01119F.

[3] Yamamoto, U.; Schweizer, K. S. *Macromolecules* **2015**, *48*, 152–163, DOI: 10.1021/ma501150q.

[4] Cai, L.-H.; Panyukov, S.; Rubinstein, M. *Macromolecules* **2011**, *44*, 7853–7863, DOI: 10.1021/ma201583q.

[5] Poling-Skutvik, R.; Krishnamoorti, R.; Conrad, J. C. *ACS Macro Letters* **2015**, *4*, 1169–1173, DOI: 10.1021/acsmacrolett.5b00616.

[6] Kohli, I.; Mukhopadhyay, A. *Macromolecules* **2012**, *45*, 6143–6149, DOI: 10.1021/ma301237r.

[7] Mason, T. G.; Weitz, D. A. *Physical Review Letters* **1995**, *74*, 1250–1253, DOI: 10.1103/PhysRevLett.74.1250.

[8] Chapman, C. D.; Lee, K.; Henze, D.; Smith, D. E.; Robertson-Anderson, R. M. *Macromolecules* **2014**, *47*, 1181–1186, DOI: 10.1021/ma401615m.

[9] Everts, J. C.; Hołyst, R.; Makuch, K. *Physics of Fluids* **2025**, *37*, 027170, DOI: 10.1063/5.0253886.

[10] Gittes, F.; Mickey, B.; Nettleton, J.; Howard, J. *Journal of Cell Biology* **1993**, *120*, 923–934, DOI: 10.1083/jcb.120.4.923.

[11] Sokołowski, W.; Jamil, H.; Makuch, K. *Soft Matter* **2026**, DOI: 10.1039/d6sm00101g.

[12] Todd, B. D.; Hansen, J. S.; Daivis, P. J. *Physical Review Letters* **2008**, *100*, 195901, DOI: 10.1103/PhysRevLett.100.195901.

[13] Hansen, J. S., *Nanoscale Hydrodynamics of Simple Systems*; Cambridge University Press: Cambridge, 2022, DOI: 10.1017/9781009158749.

[14] Hansen, J. S.; Greenfield, M. L.; Dyre, J. C. *The Journal of Chemical Physics* **2018**, *148*, 034503, DOI: 10.1063/1.4986569.

[15] Evans, D. J.; Morriss, G., *Statistical Mechanics of Nonequilibrium Liquids*, 2nd ed.; Cambridge University Press: Cambridge, 2008, DOI: 10.1017/CBO9780511535307.

[16] Fransson, E.; Slabanja, M.; Erhart, P.; Wahnström, G. *Advanced Theory and Simulations* **2021**, *4*, 2000240, DOI: 10.1002/adts.202000240.

[17] Berger, E.; Fransson, E.; Eriksson, F.; Lindgren, E.; Wahnström, G.; Rod, T. H.; Erhart, P. *Computer Physics Communications* **2025**, *316*, 109759, DOI: 10.1016/j.cpc.2025.109759.

[18] Ramírez, J.; Sukumaran, S. K.; Vorselaars, B.; Likhtman, A. E. *The Journal of Chemical Physics* **2010**, *133*, 154103, DOI: 10.1063/1.3491098.

[19] Adeyemi, O.; Zhu, S.; Xi, L. *Physics of Fluids* **2022**, *34*, 053107, DOI: 10.1063/5.0090540.

[20] Liu, X.; Guo, X.; Liao, Q. *Polymer* **2024**, *290*, 126519, DOI: 10.1016/j.polymer.2023.126519.

[21] Plimpton, S. *Journal of Computational Physics* **1995**, *117*, 1–19, DOI: 10.1006/jcph.1995.1039.

[22] Thompson, A. P.; Aktulga, H. M.; Berger, R.; Bolintineanu, D. S.; Brown, W. M.; Crozier, P. S.; in 't Veld, P. J.; Kohlmeyer, A.; Moore, S. G.; Nguyen, T. D.; Shan, R.; Stevens, M. J.; Tranchida, J.; Trott, C.; Plimpton, S. J. *Computer Physics Communications* **2022**, *271*, 108171, DOI: 10.1016/j.cpc.2021.108171.

[23] Nguyen, T. D.; Plimpton, S. J. *Computational Materials Science* **2015**, *100*, 173–180, DOI: 10.1016/j.commatsci.2014.10.068.

[24] Brown, W. M.; Wang, P.; Plimpton, S. J.; Tharrington, A. N. *Computer Physics Communications* **2011**, *182*, 898–911, DOI: 10.1016/j.cpc.2010.12.021.

[25] Groot, R. D.; Warren, P. B. *The Journal of Chemical Physics* **1997**, *107*, 4423–4435, DOI: 10.1063/1.474784.

[26] Español, P.; Warren, P. *Europhysics Letters (EPL)* **1995**, *30*, 191–196, DOI: 10.1209/0295-5075/30/4/001.

[27] Español, P.; Warren, P. B. *The Journal of Chemical Physics* **2017**, *146*, DOI: 10.1063/1.4979514.

[28] Gissinger, J. R.; Nikiforov, I.; Afshar, Y.; Waters, B.; Choi, M.-k.; Karls, D. S.; Stukowski, A.; Im, W.; Heinz, H.; Kohlmeyer, A.; Tadmor, E. B. *The Journal of Physical Chemistry B* **2024**, *128*, 3282–3297, DOI: 10.1021/acs.jpcb.3c08419 Publisher: American Chemical Society.

[29] Grosberg, A. Y.; Joanny, J.-F.; Srinin, W.; Rabin, Y. *The Journal of Physical Chemistry B* **2016**, *120*, 6383–6390, DOI: 10.1021/acs.jpcb.6b03339.

[30] Puscasu, R. M.; Todd, B. D.; Daivis, P. J.; Hansen, J. S. *Physical Review E* **2010**, *82*, 011801, DOI: 10.1103/PhysRevE.82.011801.

[31] Batchelor, G. K. *Journal of Fluid Mechanics* **1976**, *74*, 1–29, DOI: 10.1017/S0022112076001663.